Design of an anemometer to characterize the flow in the rotor rim ducts of a hydroelectric generator

Kevin Venne

Department of Mechanical Engineering

McGill University
Montréal, Québec, Canada
August 2017

A thesis submitted to McGill University in partial fulfillment of the requirements for the degree of Master of Engineering

ACKNOWLEGEMENTS

ABSTRACT

Due to its complex geometry, the airflow within hydroelectric generators is difficult to characterize. Although Computational Fluid Dynamics (CFD) can be a reliable engineering tool, its application to the field of hydroelectric generators is quite recent and has certain limitations, which are in part due to geometrical and flow complexities, including the coexistence of moving (rotor) and stationary (stator) components. For this reason, experimental measurements are required to validate CFD simulations of such complex flows. To this end, a 1:4 scale model of a hydroelectric generator was constructed at the *Institut de recherche d'Hydro-Québec* (Hydro Québec's Research Institute - IREQ) and measurements using Particle Image Velocimetry (PIV) were performed to characterize the flow therein. However, this technique cannot be used in machines and thus, new flow sensors must be developed to measure the flow in the confined and harsh regions in these machines. The main region of interest is the flow within the rotor rim ducts, since it is directly responsible for cooling the poles (one of the most critical components). This rather complex task required the design of an anemometer that had to be accurate, durable, cost-effective, easy to install, and able to withstand the extreme conditions found in hydroelectric generators (temperatures of 45°C, centrifugal forces of 300 g, etc.). In this thesis, a thermal mass flow meter and a method for validating its performance, using hot-wire anemometry and a static model of a rotor rim, was developed. The sensor is equipped with two uniquely designed features: i) a heating element made of an array of Nichrome wires and ii) Resistance Temperature Detectors (RTDs) made of Balco wires. This design is capable of: i) measuring the mass flow rate in the rotor rim ducts with an accuracy of approximately 10%, ii) fitting inside small rectangular ducts (12.2 mm by 51 mm), iii) resisting forces up to 300 g, and iv) making measurements that are not altered by the magnetic fluxes found in the rotor poles.

ABRÉGÉ

La complexité géométrique des alternateurs rend la caractérisation de l'écoulement d'air dans ces machines très difficile à réaliser. En dépit de la fiabilité des outils de modélisation tels que la *Computational Fluid Dynamics* (CFD), leur utilisation dans le domaine des alternateurs est très récente et implique certaines limitations, qui sont dues en partie à la complexité de la géométrie et de l'écoulement, et à la coexistence de composantes rotative (rotor) et fixe (stator). En conséquence, des mesures expérimentales sont requises pour la validation de simulations numériques et pour ce faire, une maquette tournante d'alternateur (échelle 1:4) a été construite à l'Institut de recherche d'Hydro-Québec (IREQ). De plus, des mesures par *Particle Image Velocimetry* (PIV) ont été réalisées afin de caractériser l'écoulement au niveau du rotor et du stator. Cependant, cette technique ne peut pas être utilisée dans des alternateurs réels et il est donc nécessaire de développer de nouveaux capteurs pour mesurer l'écoulement dans des régions confinées de ces machines. Une région d'intérêt particulier se situe au niveau de la jante du rotor, car l'écoulement sortant des canaux a un impact majeur sur le refroidissement des pôles (une des composantes critiques). Cette tâche très complexe nécessite la conception d'un anémomètre fiable, durable, abordable, simple à installer et en mesure de résister aux conditions extrêmes normalement rencontrées dans les alternateurs (températures de 45ᵒC, forces centrifuges de 300 *g*, etc.). Dans cette thèse, un débitmètre massique de type thermique et une méthode permettant de valider sa performance, en utilisant un anémomètre à fil chaud et une maquette statique d'une jante de rotor, ont été développés. Ce capteur est équipé de deux design uniques : i) un élément chauffant fabriqué avec des fils de Nichrome et ii) des *Resistance Temperature Detectors* (RTDs) fabriqués avec des fils de Balco. Ce design peut : i) mesurer le débit massique dans les canaux de la jante du rotor avec une précision approximative de 10%, ii) être inséré dans de petits canaux rectangulaires (12.2 mm par 51 mm), iii) résister à des forces centrifuges de 300 *g*, et iv) prendre des mesures qui ne sont pas altérées par les flux magnétiques qui se retrouvent dans les pôles du rotor.

TABLE OF CONTENTS

LIST OF FIGURES

LIST OF TABLES

LIST OF SYMBOLS

Latin

- A = area
- A_A = area at location A
- A_B = area at location B
- A_c = cross-sectional area
- A_s = surface area
- a, b, c = polynomial constants
- B = magnetic flux density
- Bi = Biot number
- C = constant
- C_1, C_2 = correlation coefficients
- C_α = temp. coeff. of resistance
- C_D = coefficient of drag
- c = specific heat
- c_p = c at constant pressure
- D = diameter
- D_A = diameter at location A
- D_B = diameter at location B
- D_f = drag force
- d = distance between transducers
- E = voltage/electrical potential
- F = force
- F_{max} = maximum force
- Fo = Fourier number
- f = frequency
- f_r = reflected sound frequency
- f_t = transmitted sound frequency
- g = acceleration due to gravity
- h = convective heat transfer coefficient

- $\bar{h}$ = average h
- H = frontal width
- I = current
- k = thermal conductivity
- L_α = coefficient of resistivity
- l = length
- N = number/quantity
- N_L = number of rows of wires
- Nu = Nusselt number
- N_{pls} = number of pulses
- $n.m$ = exponential constants
- $\dot{m}$ = mass flow rate
- $\dot{m}_{hot-wire}$ = mass flow rate obtain via hot-wire
- $\dot{m}_{sensor}$ = mass flow rate obtain via thermal mall flow meter
- P = pressure
- P_A = pressure at location A
- P_B = pressure at location B
- Pr = Prandtl number
- Pr_s = surface Prandtl number
- Q = flow rate
- R = electrical resistance
- R_{RTD} = RTD resistance
- R_0 = R at 0°C
- R_{100}= R at 100°C
- Re = Reynolds number
- r_P = prototype radius
- r_M = scale model radius
- S_T = transverse pitch

- S_L = longitudinal pitch
- St = Strouhal number
- T_i^k = discrtized temperature at the ith spatial node at time k
- T_0^k = discrtized temperature at the left wall (0) at time k
- $T_{i_{max}}^k$ = discrtized temperature at the right wall (i_{max}) at time k
- T_0 = temperature at 0°C
- T_b = bulk temperature
- T_o = outlet temperature
- T_i = inlet temperature
- T_{RTD} = RTD temperature
- T_S = wire surface temperature
- T_S = temp. rise due to source
- T_∞ = free stream temperature
- t = time
- U = velocity
- U_A = velocity at location A
- U_B = velocity at location B
- w = of wire (subscript)
- x, y, z = length scales/distances
- $\%Er$ = percentage error

Greek

- α = thermal diffusivity
- β = diameter ratio
- γ = specific weight
- Δ = differential
- δ = air gap
- θ = angle
- μ = dynamics viscosity
- ν = kinematic viscosity
- ρ = density
- σ_y = yield stress
- τ_W = wall shear stress
- χ = electrical resistivity
- χ_0 = χ at 0°C
- χ_{20} = χ at 20°C
- ω_p = prototype roational speed
- ω_M = model rotational speed

Script

- $\mathcal{A}, \mathcal{B}$ = calibration constant
- $\mathcal{A}_L$ = Leinhard's 1st hot-wire calibration correction coefficient
- $\mathcal{B}_L$ = Leinhard's 2nd hot-wire calibration correction coefficient
- $\mathcal{b}$ = intercept
- $\mathcal{C}$ = speed of sound
- $\mathcal{D}$ = dissipation constant
- $\mathcal{m}$ = slope
- $\mathcal{N}$ = dimensionless parameter based on wire geometry
- $\mathcal{P}_{inj}$ = power injected into flow
- $\mathcal{Q}$ = sensitivity index
- $\mathcal{R}$ = result
- $\mathcal{S}$ = source term
- $\mathcal{U}$ = uncertainty
- $\mathcal{U}_0$ = zeroth-order uncertainty

Chapter 1
Introduction

1.1 Hydroelectricity in Québec

According to the Canadian Hydropower Association (CHA), Canada has a potential of 160,000 MW in hydroelectricity. In 2016, the CHA announced that Canada's current installed capacity was 76,000 MW, which represents 48% of the nation's potential. Hydroelectricity accounts for 63% of Canada's electrical consumption, making hydropower a cornerstone of the nation's economy. The province of Québec has the largest potential with 42,400 MW, accounting for 27% of the nation's overall hydroelectric potential. The CHA has estimated Québec's current installed capacity to be 38,400 MW (i.e., 91% of its potential). Therefore, Québec is the province in Canada with the largest potential, and the largest installed hydropower capacity. This can be attributed to the province's 500,000 lakes and 4,500 rivers covering 12% of its surface area and a power company (Hydro-Québec) committed to using renewable energy resources for power generation. The numbers presented above clearly demonstrate the importance of hydropower in Québec and its potential for future economic development.

To meet the province's energy demands, Hydro-Québec was founded in 1944, and quickly thereafter the company began the construction of hydropower plants Beauharnois, Carillon, Bersimis-1 and Bersimis-2. By 2016, the company harnessed 75 rivers to build 63 hydroelectric power plants, 27 large reservoirs, 668 dams, and 98 control structures. Today, 99% of Hydro Québec's power generation is from renewable resources, with a large majority coming from hydropower.

The key component in a hydropower plant is the turbine-generator group. The turbine extracts the kinetic energy of flowing water, and the generator, which is connected to the turbine by a shaft, transforms this energy into electrical energy, as illustrated in Fig. 1-1. In hydropower plants, the turbine-generator group is called the generating unit.
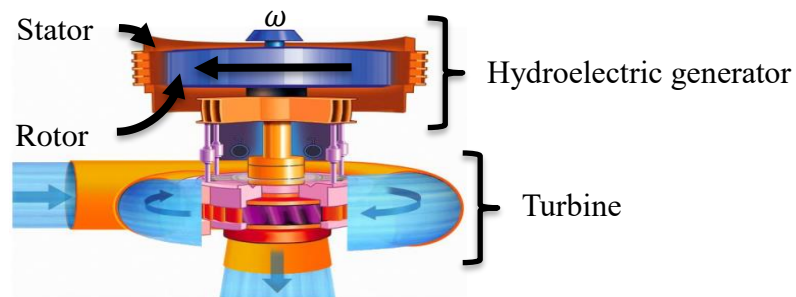
Figure 1-1 Generating unit [1]

Generating units typically have high operating efficiencies of around 98%, but a portion of the converted energy is lost as heat. However, this loss can still cause a significant temperature rise of the machine. This rise creates hot spots in the machine resulting in the degradation of insulation, that can lead to mechanical or electrical failures. Thus, the operating temperature of the machinery needs to be well controlled to increase its longevity. Hydroelectric generators cool themselves by drawing in air (like a pump) and pushing it through the rotor and stator components (shown in Fig. 1-2). The air passes through the rotor through small rectangular openings called rotor rim ducts. The flow passing through these ducts cools the poles on the outer rim of the rotor and the stator. Thus, the rotor acts as a fan, and an optimal equilibrium is required between the airflow rate needed to efficiently cool the equipment and the associated windage losses. Windage losses is a term typically used in electric machines that refers to the increased resistance put on the rotating shaft by the pressure forces the air must overcome to pass through the machine. Between 20% and 30% of the total energy lost in a hydroelectric generator is attributed to windage losses. Therefore, cooling is an important factor to consider when aiming to improve both the efficiency and the longevity of a generating unit.

1. Spider Arm	4. Pole	7. Radiator
2. Rotor Rim	5. Stator	8. Pit Opening
3. Fan Blades	6. Frame	
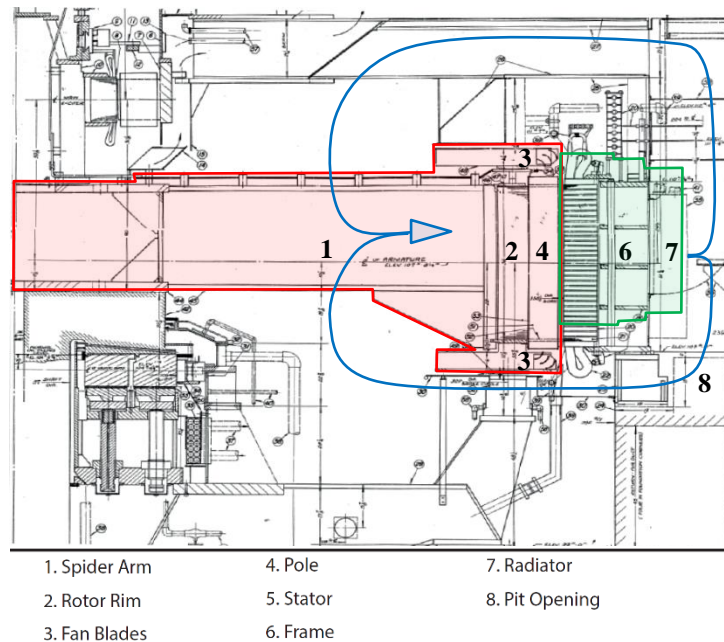
Figure 1-2: Schematic of the airflow (blue) through the rotating (red) and stationary (green) components of a hydroelectric generator

1.2   The DIAAA project

In 2002, the *Institut de recherche d'Hydro-Québec* (Hydro Québec's Research Institute - IREQ) launched a project called AUPALE: *Augmentation de la Puissance des Alternateurs Existants* (Increasing the Power Generation of Existing Hydroelectric Generators) in an effort to increase the power output of existing generating units without compromising their lifespan. As illustrated in Fig. 1-3, the project primarily focused on generator multiphysics modeling, which required the joint efforts of many teams to carry out electromagnetic, thermal, mechanical and fluid dynamical simulations. The main reason for starting this project was that the majority of Québec's generating units were built in the 70s-80s and, at that time, engineers were not able to model in detail the complex phenomena occurring in the diverse components due to limitations in the available computational tools. Consequently, generating units were designed with large factors of safety. The underlying foundation of the AUPALE project is that a combination of new numerical and experimental techniques could increase the understanding of these devices, allowing Hydro-Québec to increase the power production of their fleet without having to build new generating units. A broader description of the project and related results can be found in Hudon *et al.* [2].
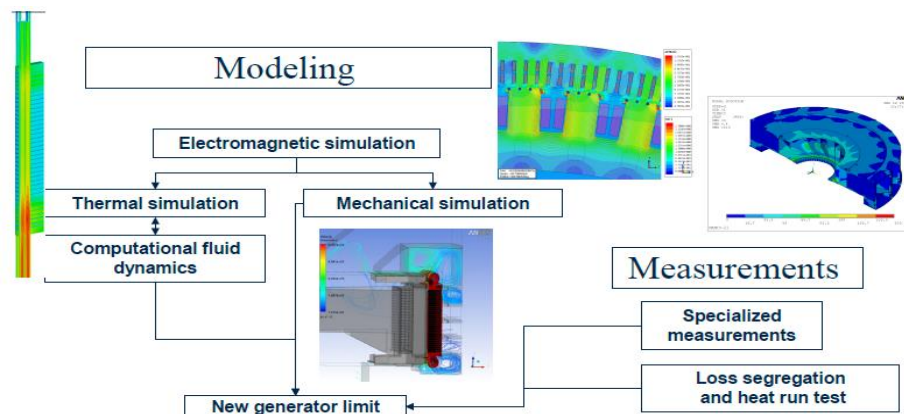
Figure 1-3: The AUPALE project [2]

In 2015, the research project changed its name to DIAAA: *Diagnostic Avancé des Alternateurs* (Advanced Diagnostics of Hydroelectric Generators) due to a shift in the company's perspective that preferred increasing a generating unit's lifespan rather than its power production capacity. However, the multiphysics modeling approach remained the

same. One of the first goals of DIAAA was to resolve a specific long-term maintenance issue on an existing hydroelectric generator, which is the overheating of the rotor poles, as illustrated in Fig. 1-4.

Figure 1-4: Burnt rotor pole

Fig. 1-4 shows a burnt rotor pole with insulation oozing out of it. One of the suspected reasons for the failure is insufficient airflow from the rotor rim ducts — more specifically a non-uniform velocity profile exiting the rotor.

As previously mentioned, one of the key aspects of the research project was modeling the airflow in hydroelectric generators since understanding the flow dynamics and heat transfer mechanisms in its components is critical to its efficient operation. Numerical tools such as Computational Fluid Dynamics (CFD) are increasingly used to characterize the thermofluid behavior of large electrical machines. However, the geometric and flow complexities require the validation of simulation results since numerical models have not yet achieved a sufficient degree of maturity to be used alone. Consequently, experimental measurements on hydroelectric generators are needed, but, they are costly, time-consuming, and rare given that access to real machines is often limited. The use of a laboratory scale model is thus a potential solution for the acquisition of data needed to validate numerical models, without the limitations associated with *in situ* measurements. For this reason, the IREQ built a simplified scale model generator that lacks the active electromagnetic elements of a prototype, but it includes all main ventilation components. This scale model was also partially built with transparent materials to allow optical access in anticipation of non-intrusive flow measurements, such as particle image velocimetry (PIV).

Using the scale model, much work has been undertaken as part of the AUPALE/DIAAA project. Firstly, a CFD analysis of the entire airflow circuit in the scale model was undertaken by Toussaint as part of his Master's thesis [3]. His work investigated the effect of various numerical parameters on the predicted flow, as well as the best practices for modeling such type of flows. Secondly, in an effort to validate Toussaint's work, an experimental campaign, using PIV, was subsequently performed by Bach [2]. This study showed good agreement between the computed and measured flow velocities in different components of the hydroelectric generator scale model. Although, the PIV measurements performed on the scale model provided a preliminary validation of the numerical model, more experimental data from actual prototypes is required to achieve a higher level of confidence in the CFD modeling. Moreover, PIV cannot be used for measurements in a real generator due to the harsh environment and the absence of optical accesses. For this reason, accurate and robust airflow sensors need to be designed for applications within hydroelectric generators.

Early work on sensor development on hydroelectric generators began on the stator. To characterize the flow exiting the stator ducts, an airflow device based on a differential pressure measurement was designed by Torriano [4], using several of these devices the author was able to measure the axial-flow distribution exiting the stator cooling ducts. This device has been successfully installed on many hydroelectric generators at Hydro-Québec and has provided useful information. Given this sensor's success, focus has shifted to the flow in the rotor. Torriano's device however, cannot be installed on the rotor rim due to geometrical and mechanical constraints. A first attempt in designing such a device was done as part of Saleban's Master's thesis [5], which resulted in a micro-motor equipped with an impeller. Its principle of operation was that the airflow makes the impeller turn, and by measuring the electric signal generated by the motor, the air velocity can be determined (using calibration data). Although the sensor worked correctly in a static setup, it exhibited some serious limitations when tested on the rotating scale model, mainly because the small moving parts were not able to operate when exposed to the high centrifugal forces seen in the rotor.

The limitations associated with the micro-motor sensor, motivated the search for a more robust and reliable device, which has become the main scope of the research project herein.

1.3 Objectives of the present work

Prior work both numerical (by Toussaint [3]) and experimental (by Torriano [4] and Saleban [5]) have emphasized the need for the development of new measurement techniques that can be used in such restricted and complex flows that occur in the rotor of hydroelectric generators. Thus, the focus of the present research project is to design a sensor that can be easily integrated into the hydroelectric generator rotor rim ducts. Moreover, the measuring device must be durable, cost-effective, easy to install and able to withstand the harsh conditions (temperature, vibrations, etc.) found in real hydroelectric generators.

Given the above, the principal objectives of the present research are to design an anemometer that:

 i. provides an accurate measurement of the airflow in the rotor rim duct,

 ii. is small enough to fit inside a typical rotor rim duct (12.2 mm by 51 mm),

 iii. is sufficiently robust to withstand the high centrifugal forces (~300 g) and the relatively high temperatures (around 45°C) found in the rotor,

 iv. and its performance should not be altered by the magnetic fluxes generated by the rotor poles.

1.4 Research approach and thesis structure

The underlining approach used in the development of the anemometer that ultimately met the research objectives was split into three phases. The first is the preliminary phase, the second is the validation phase, and the last phase is the proof of concept.

The preliminary phase was divided into three parts that are discussed in three different chapters of this thesis: a literature review (Chapter 2), a review of the IREQ's experimental approach to hydroelectric generators (Chapter 3), and a review of the existing measurement techniques (Chapter 4). These steps were taken to fully understand the project and to collect ideas for the subsequent phases. Prior to the commencement of the next phase

the concepts collected in the preliminary phase were filtered (Section 3 of Chapter 4). A list of design specifications was made, and, for each criterion, a rating varying from 0 (poor) to 5 (excellent) was given to each technique. The first iteration of concept filtering allowed for the selection of two measurement techniques. Although only one sensor type is needed in principle, developing two would allow for an alternate option should complications arise for a given design in the preliminary validation phase.

The validation phase was split into two parts: the analytical validation (Chapter 5) and the experimental validation (Chapter 6). The analytical validation was undertaken to answer the questions posed in the concept filtering regarding the potential performance of the chosen techniques. Thus, using analytical and numerical methods, the performance of each technique was calculated by varying the geometrical or mechanical parameters such as wire diameters and material types. This step would determine the technique's feasibility of obtaining the research objectives. The experimental validation involved the design of the experimental apparatus and prototypes of the chosen measuring technique. This step would refine the sensor's design until a solution was found.

The final phase of the project was the proof of concept phase (Chapter 7). This phase consisted of the sensor's validation in a simplified version of the rotor rim that consisted of a wood stack with rectangular openings that replicate the rim ducts and an air blower connected to the wood stacks providing the airflow. This non-rotating model is referred to as the static model hereafter. The main objective of the static model is to quickly test the sensors under different flow conditions and to easily troubleshoot potential problems with a design. Once satisfactory results are obtained on the static model, one can draw main conclusions and propose a plan for future implementation of the sensor to meet the broader objectives of the DIAAA project (Chapter 8), which includes measurements on the rotating scale model. Such measurements will allow the IREQ to further evaluate the sensor's performance under more realistic operating conditions, test its data acquisition system, and pass safety requirements needed to make measurements on a real hydroelectric generator.

Chapter 2
Literature Review

The first part of the preliminary phase was the literature review, which is divided into three sections: i) advancements in the field of hydroelectric generators, ii) experimental studies on the static components, and iii) experimental studies on the rotating components.

2.1   Advancements in the field of hydroelectric generators

Understanding the ventilation circuit of hydroelectric generators is essential to increasing their longevity since an inefficient ventilation results in premature aging or even failure. Hydroelectric generators are cooled by the convection of a fluid (usually air) through the main components of the system. However, this cooling comes at a cost as ventilation losses, sometimes referred to as windage losses, can account for 30% or more of the global losses of the machine [4]. In the past, the ventilation and thermal aspects of electrical machines were sometimes neglected by the designers and often overshadowed by the electromagnetic analysis [6]. The reason for the neglect of this aspect is that electrical machines are generally designed by electrical engineers that have a background in electromagnetics, whereas heat transfer is a background commonly associated with mechanical engineers [6]. Yet, it is well known that there is a strong coupling between the electromagnetic and thermal aspects of electrical machines [6,4]. This is because the magnetic losses are dependent upon temperature and *vice versa*. Typically, only global ventilation losses are obtained as inputs to the thermal model, as explained in Chaaban *et al*. [7]. However, such tests do not provide the distribution of losses in different components of the generator. With the increasing demands of more compact, more efficient, and less expensive electric machines, designers must consider this multiphysics phenomenon.

To meet the increasing energy demands, companies like Hydro-Québec are forced to increase the power output of their generating units by focusing on the thermal-electromagnetic coupling of these machines. Chaaban *et al*. discuss the challenges of pushing the limits of hydroelectric generators to meet these requirements [7]. In hydro-power production the most expensive component is the hydroelectric generator. These generators were built decades ago and due to large factors of safety, they are generally operated well below nominal capacity. Chaaban *et al*. gives two ways that Hydro-Québec

can increase their power production: either by replacing old turbines with more efficient/durable ones, or operating existing units at the maximum possible load sacrificing hydraulic efficiency [7]. In either case, the core and winding temperatures in the stator will increase, potentially exceeding the temperature limit imposed by the class of insulation. Companies such as Hydro-Québec have found it more cost effective to follow the second route. Therefore, researchers must now find an optimal equilibrium between the temperature of the machine and the ventilation losses. To achieve this, the pressure drop in ventilation circuit must be minimized to reduce the ventilation losses and the flow path must be altered to appropriately distribute convective cooling to the components that are most susceptible to overheating. Currently, there are three methods of achieving this goal: analytical methods, numerical methods or experimental measurements.

Analytical methods of electrical machines based on the Lumped-Parameter Thermal-Network (LPTN) are the most used technique in industry as they are the simplest and least computationally demanding method [8-10]. The LPTN method involves modeling the machine as a series of thermal circuits with imposed (conductive, convective, etc.) heat losses that model the thermal behavior. The accuracy of the model is highly dependent upon the calibration of the loss and heat transfer coefficients for the entire thermal circuit. The calibration of the model is generally obtained using analytical formulas (e.g. textbook values) or experimental measurements from real machines or scale models. Limitations of this modeling approach are: i) it cannot give detailed information on the ventilation and heat transfer coefficients, and ii) it is limited to the geometric configuration upon which the calibration was based. For example, electrical machines such as hydroelectric generators have different ventilation configurations (radial, axial, hybrid, with or without auxiliary ventilation, etc.), and the LPTN method would require one to calibrate their model for each of these configurations.

The limitations of the LPTN method have motivated the development of more advanced computational methods that can perform complex simulations of electrical machines. One numerical approach used for the analysis of electrical machines is the Finite Element Analysis (FEA) method. FEA accurately models the conductive heat transfer at solid boundaries, but uses the same techniques as the LPTN to model the convective

9

boundary conditions. The only advantage FEA has over LPTN is that it can model solid component conduction more accurately in complex geometries.

A numerical method that overcomes the weaknesses of the LPTN and FEA approaches is CFD. The latter solves the equations of conservation of mass, energy, and momentum of a fluid, and thus does not require the use of empirical formulas. Meshing tools also allow for a finer discretization of hydroelectric generators as compared to the LPTN method. This allows for a more detailed description of the air flow in the cooling circuit. Many studies [11-17] have been published in recent years on the use of CFD in the components of electrical machines and the results have proven beneficial in the field of hydroelectric generators.

Due to these increasing benefits, the IREQ launched a project in 2002 to create a numerical model to achieve its goal of increasing the power production of hydroelectric generators without compromising their longevity. The model had to consider electromagnetic, thermal, mechanical and fluid dynamical factors. Hudon *et al.* described the relationships between the physical phenomena (i.e. the analysis of the coupling between these factors) and the challenges associated with model validation [4]. Like any numerical model, CFD simulations require experimental validation via measurements on real machines or scale models. However, experimental results in hydroelectric generators are rare due to limited shutdowns needed to perform these tests. For this reason, many experimental studies on hydroelectric generators have used scale models, which provide a better control over the geometric parameters, so that one may study their effect on the convective cooling [18-24]. However, *in situ* measurements remain a necessary tool to quantify several physical quantities (e.g. airflow distributions) and to supply boundary conditions to the numerical models. Consequently, it is important to develop techniques to measure the airflow in the rotating and stationary parts of a hydroelectric generator.

2.1.1   Experimental studies on the stationary components

The most challenging modeling aspect in hydroelectric generators is the ventilation process as only field measurements are available to serve as inputs to the thermal model [4]. To resolve this limitation, and as part of the AUPALE project, the IREQ began the development of a sensor that could measure the airflow distribution at the exit of the stator

10

cooling ducts. This goal was achieved in 2008 by the development of a Venturi-type flow meter called the converging cone (shown in Fig. 2-1).
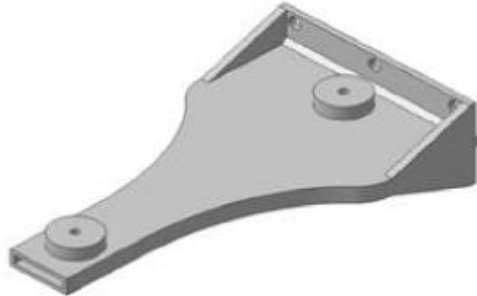
Figure 2-1: Converging cone for flow measurements in the stator ducts [4]

The cone covers 15 cm of the duct width in the circumferential direction and is attached to the duct by magnets. To obtain the average airflow rate exiting the stator duct, one places the cones at the duct outlet and the airflow rate is then measured by the pressure differential using calibration curves obtained on an experimental rig. The axial flow distribution exiting the stator is obtained by placing several cones along the height of the stator on an operating hydroelectric generator.

Other approaches have also been taken in measuring the flow through the fixed components of hydroelectric generators. For example, experiments have been carried out to determine the flow rates at the exit of the coolers [25] and in the stator [13,15]. At first, only measurements in air coolers were undertaken (Filipian *et al*. [25]) due to their simplicity, but more complex measurements are now obtainable, such as PIV measurements in scale models, such as those presented by Hartomo *et al*. [19] and Bach *et al*. [24]. As shown by the literature, work on hydroelectric generators began on the water coolers [25], then moved to more complex regions such as the stator [13, 15] and rotor components [24].

2.1.2   Experimental studies on the rotating components

Due to the past success of direct measurements in the stator an attempt to obtain direct measurements of the airflow in rotors was undertaken in 2013. This project was proposed by IREQ in collaboration with *l'École Polytechnique Fédérale de Lausanne* (EPFL) for Saleban's Master's thesis [5]. The goal was to develop an anemometer to measure the flow rate in the rotor rim ducts.

To achieve this objective, Saleban had to choose from the numerous methods capable of measuring a fluid flow velocity. After reviewing many methods, Saleban opted for a mini turbine flow meter, as shown in Fig. 2-2.
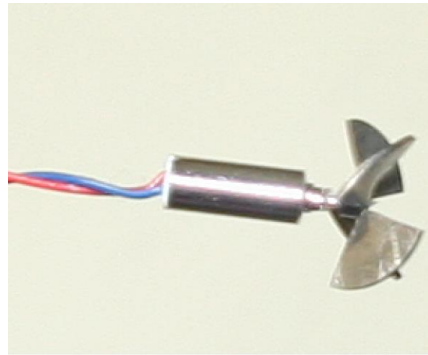
Figure 2-2: Miniature turbine flow meter equipped with a mini DC motor [5]

This type of device converts rotational motion induced by the flowing fluid into a velocity by measuring the voltage generated by the DC motor. The turbine's impeller had a diameter of 10 mm with blades bent at 45°. The DC motor was 3.2 mm in diameter, 8.1 mm in length, and rated at a torque of 0.01 mN·m. The motor shaft had a diameter of 0.6 mm and a length of 3.3 mm.

This method ultimately did not meet expectations due to the underestimated effect of the centrifugal force in the scale model on the bearings of the mini DC motor in fact, it was found that the applied centrifugal force of 0.65 N on the impeller caused it to push too hard against the DC motor bearing and this made it impossible for the incoming flow to make the impeller rotate.

Although this project did not achieve all the objectives, the challenges involved in developing an anemometer for the rotor rim ducts were better understood and to our knowledge, there have been no other attempts to directly measure the airflow in the rotor

of a hydroelectric generator. Furthermore, ventilation measurements on real hydroelectric generators are, in most cases, only partial, and therefore cannot be used to create the required ventilation maps nor calibrate numerical models (especially in the case of the rotor). In addition to these difficulties, there is a general lack of understanding of the flow dynamics in the complex geometries of large hydroelectric generators. It is for this reason that, in 2009, the IREQ decided to design and build a scale model of a hydroelectric generator to expand our understanding from limited field measurements and that, in 2015, a new project was launched to develop a flow sensor that would overcome the obstacles encountered during the first stage of development.

Chapter 3
IREQ's Scale Model of a Hydroelectric Generator

The second part of the preliminary phase describing the review of the IREQ's experimental approach on hydroelectric generators is split into four sections: i) airflow in hydroelectric generators, ii) scale model development, iii) scale model description, and iv) the scale model CFD analysis. The first section begins with a general discussion of the airflow pattern in hydroelectric generators while detailing some of the components the flow passes through and concludes by explaining the need for a scale model to better understand the flow physics. Then the second section reviews the general scaling analysis that was carried out to create the scale model. The third section describes the components of the scale model, focusing on the rotor. To conclude, a summary of the CFD analysis on the scale model is given to better understand the fluid dynamics therein.

3.1   Airflow in hydroelectric generators

The flow pattern within a hydroelectric generator is depicted in Fig 3-1. As the rotor (1-5) spins, the rotor spider arms (1) act like a pump drawing in the flow through the rotor rim (2) and the fan blades (3). The flow can pass through the rotor, as there are small ducts called rotor rim ducts that allow the flow to cool the poles (5) on the outer rim. The portion of the flow that passes through the fan blades is primarily directed toward the end windings but, a portion of it, is also deflected in the air gap. Once the flow passes the rotor, it goes through the stator (6), and exits through the water-cooled radiators (7). Finally, the air returns to the rotor through the ceiling (9) and pit openings (8).

1. Spider Arms	4. Rotor Rim Ducts	7. Radiator Exit
2. Rotor Rim	5. Poles	8. Pit Openings
3. Fan Blades	6. Stator	9. Ceiling Opening
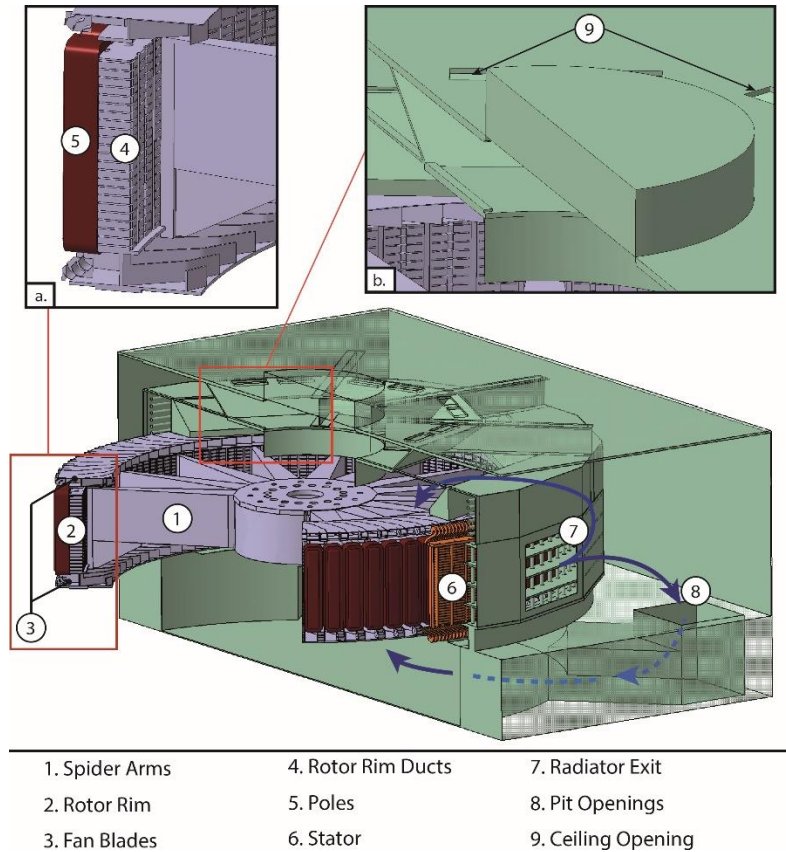
Figure 3-1: Airflow schematic through the rotating (1-5) and stationary (6-9) parts of a hydroelectric generator

The geometry is not only complex, but it involves both stationary and rotating parts making the flow difficult to model numerically. Thus, experimental measurements are necessary to increase our understanding of the airflow in hydroelectric generators and to improve the cooling efficiency of this machinery. However, measurements on operational hydroelectric generators are rare as shutdown costs are too important and one cannot install anemometers while the system is under operation. For these reasons, notable efforts have been made at the IREQ to build a scale model of a hydroelectric generator.

3.2   Scale model development

In fluid dynamics, it is often appropriate to substitute real-life mechanisms with laboratory models as in most cases, the former is too large/expensive to analyze and a smaller/inexpensive model is often more practical. This is possible by similitude analysis, a process of scaling real-life mechanisms into models to facilitate testing. The results on

the model can then be scaled up to obtain the data for the actual system. This is the basic principle for the development of a scale model hydroelectric generator at IREQ in 2009.

The design and manufacturing of the scale model was carried out by the robotics division at the IREQ [26]. Taking the project from design to realization took two years. The scale model is a simplified and scaled version of an existing hydroelectric generator in Hydro-Québec's generating fleet, as shown in Fig 3-2.
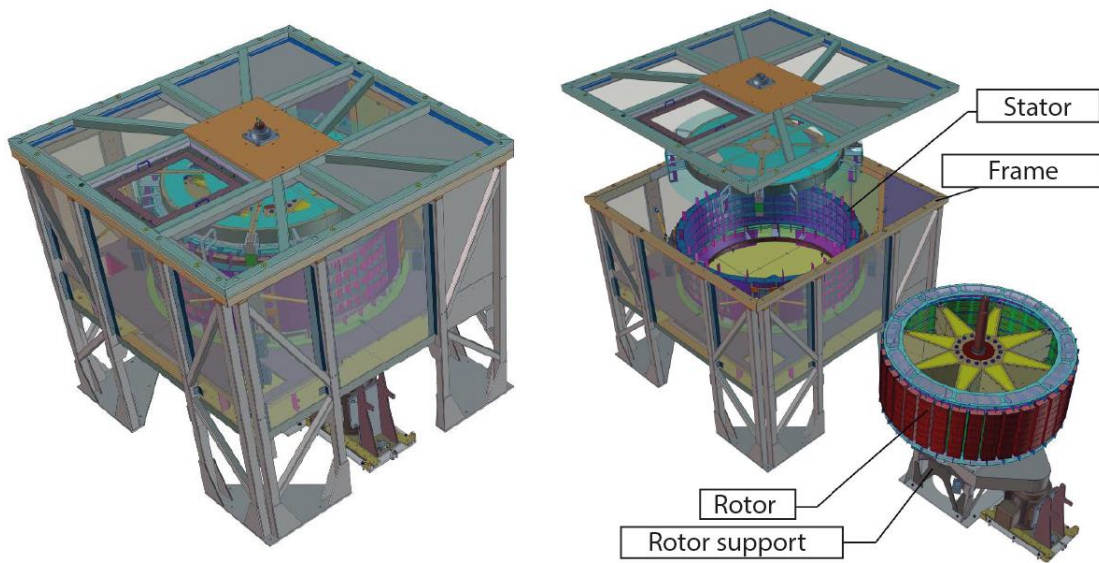
Figure 3-2: Isometric and exploded view of the scale model [3]

The model is scaled down by a factor of 4 in the radial direction and by a factor of 2 in the axial direction when compared to the prototype. Smaller scaling is applied in the axial direction to facilitate access to the interior of the machine for maintenance and instrumentation purposes. Several dimensions were not scaled, such as, the cooling ducts in the rotor rim and stator, and the air gap between the rotor and stator. This was done for two reasons: i) to conserve the similitude of the airflow, and ii) to facilitate the transfer of developed technology or anemometers to full-scale generators. Table 3-1 describes the list of dimensions that were adopted for the scale model.

Table 3-1: Comparison of dimensions between the prototype and scale model

Component	Prototype (P) [mm]	Scale Model (M) [mm]
Rotor diameter	9081	2270
Rotor height	1604	802
Rotor rim duct height	12.2	12.2
Rotor rim duct width	50.8	47.7
Air gap (δ)	12.7	12.7
Stator duct height	6.0	6.0
Stator duct width	48.7	42.5

Dimensionless similarity is maintained by adjusting the rotational speed to compensate for the reduction in size in the radial direction. The relevant dimensionless parameter is the Reynolds number (based on the air gap) and is defined as:

$$Re_\delta = \left[\frac{\rho(\omega_P r_P)\delta}{\mu}\right]_{prototype} = \left[\frac{\rho(\omega_M r_M)\delta}{\mu}\right]_{Scale\ Model} , \qquad (3.1)$$

where ω, is the rotational speed of the rotor, r is the radius of the rotor, and δ is the air gap distance. Assuming the properties of air (μ, ρ), which are functions of temperature, are approximately the same in the laboratory as they are in the prototype, Eq. 3.1 simplifies to the following expression:

$$\left[\frac{\omega_M}{\omega_P}\right] = \left[\frac{r_P}{r_M}\right] = 4. \qquad (3.2)$$

Therefore, to maintain the same tangential velocity at the rotor tip, the speed of the scale model must be 379 rpm as the prototype rotates at about 94.7 rpm. Given this information, one can assume that the airflow within the stator ducts is of the same order of magnitude as the airflow in the prototype, as the dimension of the ducts are almost identical and thus, the local Re_δ is conserved at these locations.

3.3   Scale model description

The main purpose of studying the airflow in the scale model is to obtain the required ventilation map needed for the calibration of numerical models. To achieve this goal, several geometric simplifications were made. For example, the electromagnetic components were omitted to reduce the manufacturing complexity and to aid in the

meshing process of the computational domain. Therefore, some components act as passive elements, for example, the rotor poles are made of sheet metal and formed to the shape of a real pole. Such simplifications do not impact the airflow or the convective cooling, but greatly simplify the manufacturing process and the numerical modeling. Furthermore, the heat exchanger was also omitted, and since no active electromagnetic components are present, this decouples the temperature rise in the scale model, such that it is only due to windage losses. A third geometric simplification is that many of the metallic components, such as the stator, were replaced by Plexiglas ones to allow for optical access required for PIV measurements.

Although all components must be studied to fully understand the flow dynamics and convective heat transfer in hydroelectric generators, this project mainly focuses on the rotor.

3.3.1 Scale model rotor

The scale model has an open rotor that is powered by a 75 kW (≈100 hp) electric motor capable of obtaining a maximum rotational speed of 500 rpm. As shown in Fig. 3-3, the motor will spin the rotor (1-6) causing the spider arms (4) to draw in air from the top and bottom into the fan blades (1) and the region between the spider arms. Due to its rotation, the spider arms push the air radially outwards through the rotor rim ducts (3), allowing the air to pass between the pole casings or into the interpole region (6) to cool the poles (5).

1. Fan Blades   4. Spider Arms
2. Rotor Rim   5. Poles
3. Rotor Rim Ducts   6. Interpole
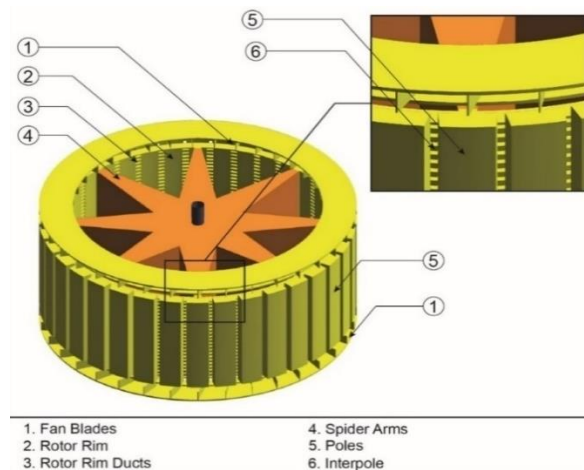
Figure 3-3: Components of the scale model's rotor [3]

To complement Fig. 3-3, the number of components on the rotor and their characteristics are shown in Table 3-2.

Table 3-2: Quantity and positioning of the rotor components [3]

Component	Number	Circumferential Periodicity
Spider Arms	8	45°
Fan Blades	72	10°
Rotor Rim Ducts	36 ($circumferential\ columns$) by 23 ($axial\ rows$)	10°
Poles	36	10°

Fig. 3-3 and Table 3-2 show that there are 23 rotor rim ducts between two adjacent poles. Most of the cool air needed to cool the poles comes from these ducts and thus it is critical to quantify the airflow rate in this region. To this end, Hydro-Québec's initial CFD analysis of the flow in the scale model is of substantial benefit in the understanding of the flow physics within the rotor.

3.4 Scale model CFD analysis

As part of DIAAA and an effort to better understand the heat transfer mechanism at the pole, CFD simulations were carried out at the IREQ on the scale model. Of interest in the CFD results are both the quantitative and qualitative features of the flow in the rotor. The CFD results of the scale model were undertaken by Toussaint [3].
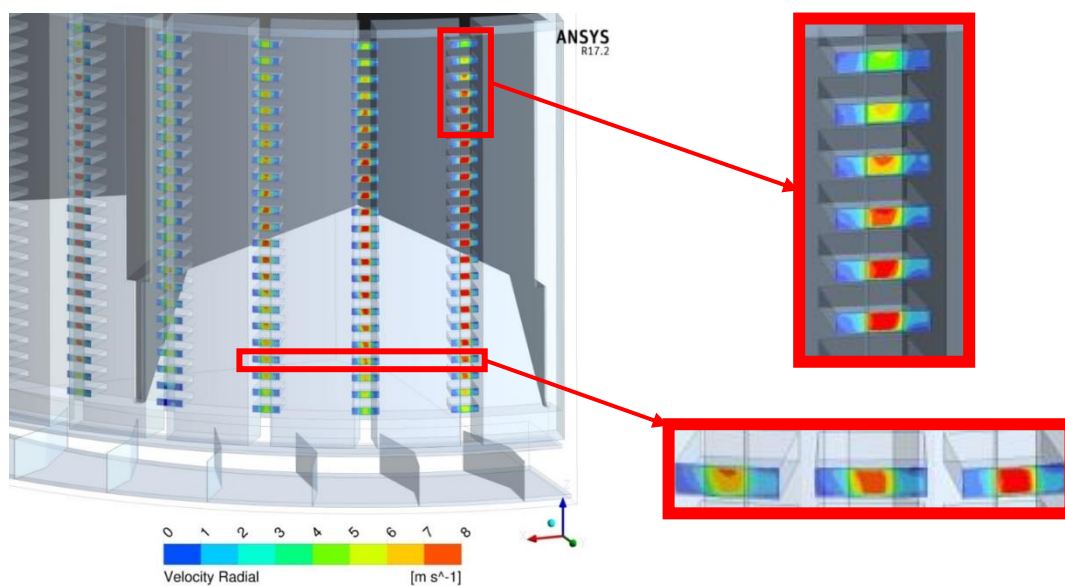
Figure 3-4: Numerically generated radial velocity profile of the rotor rim duct outlets

19

In Fig 3-4, one can observe that the radial velocity profile is non-uniform both axially and circumferentially, which may explain the uneven temperature distribution measured in some hydroelectric generator poles [20]. From these results, one can obtain the average, minimum, and maximum radial velocities exiting the rotor rim ducts:

$$\bar{U} = 3.26 \ m/s$$

$$-4.08 \ m/s \leq U \leq 12.25 \ m/s$$

as well as the corresponding average, minimum, and maximum mass flow rates:

$$\bar{\dot{m}} = \ 2.23 \ g/s$$

$$-0.27 \ g/s \leq \dot{m} \leq \ 3.50 \ g/s$$

Thus, some ducts have very low flow rates of air passing through them.

To understand why some ducts, exhibit low or even negative flow velocities, one can consider the flow in the r-θ plane to visualize the velocity profile in the spider arm region and in the rotor rim ducts, as shown in Fig. 3-5.
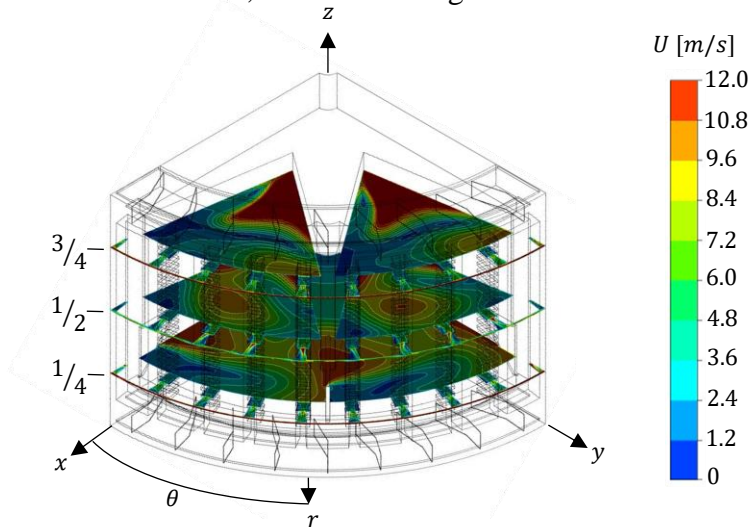
Figure 3-5: Velocity contours in planar r-θ sections at ¼, ½, and ¾ heights along the pole

As shown in Fig. 3-5, the three sections are taken in the ¼, ½, and ¾ planes along the height of the pole. Each section is centered with respect to the rotor rim ducts to observe the flow variations therein. The contours showed a variation in the velocity profile within the ducts, as well as, low velocity regions indicating recirculating flow in some ducts. These results

were better understood by considering the flow incidence angle (θ) along the sections, as shown in Fig. 3-6.
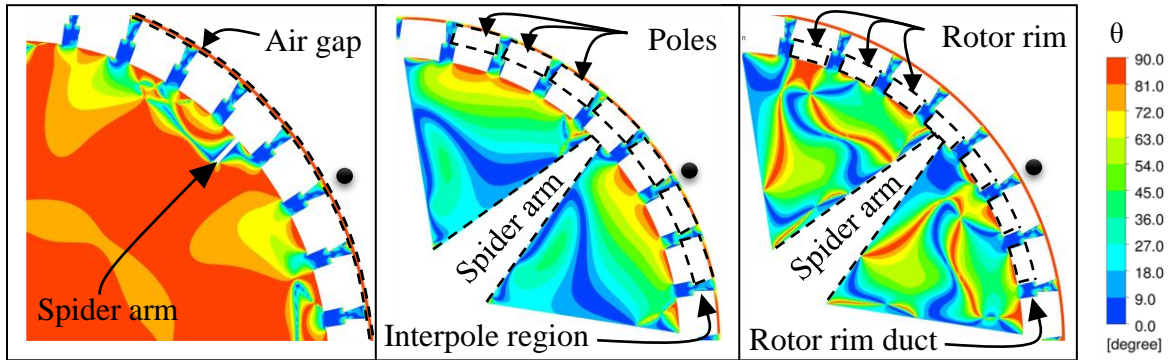
Figure 3-6: Incidence angle contours in planar sections at ¼, ½, and ¾ heights along the pole

The contours shaded in red indicate purely tangential flow, whereas contours shaded in blue indicate purely radial flow. To reduce clutter in the figures, the air gap, poles, interpole region, rotor rim, and rotor rim ducts where only shown in one of the three sections. Also shown in Fig. 3-6 is the non-uniformity of the spider arms in the axial direction. At the ¼ plane, the spider arm has a smaller width and therefore has a smaller influence on the flow, which is mainly tangential in the region between the spider arms. However, as one moves to ½ and ¾ planes, the width of the spider arm increases and therefore has a greater influence on the flow, creating large recirculation zones between the spider arms. To more closely observe how this influences the flow in the rotor rim ducts, the flow in the third duct from the bottom (indicated by the black dot) for each axial position was considered, as illustrated in Fig. 3-7.
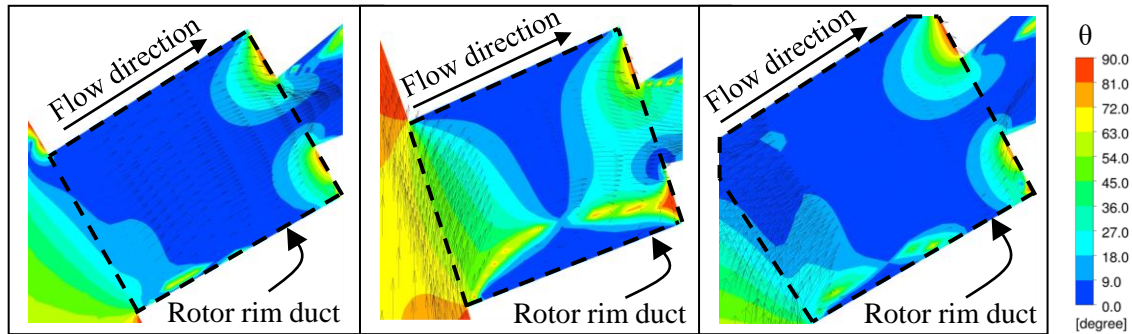
Figure 3-7: Incidence angle contours in the third rotor rim duct (from Fig. 3-6) at ¼, ½, and ¾ heights along the pole

21

From Fig. 3-7, one observes that the flow in the chosen rotor rim duct at the ¼ plane is almost purely radial, whereas the flow within the duct at the ½ plane shows a recirculation zone that is the length of the duct, and the flow in the duct a the ¾ plane shows a small recirculation zone. Fig. 3-7 also indicates that the flow impinges upon the corners of the duct and enters at about 45°. Thus, large entrance incidence angles of 45° can result in large recirculation zones that affect the net airflow in the rotor rim ducts. Another factor that affects the airflow is the spider arm configuration, where the top and bottom portions of the rotor are open allowing the air to escape, and thus, less air passes through the rotor rim ducts at these locations. This phenomenon explains the lower flow velocities in the ducts located in the upper and lower half of the rotor, which result in the observed non-uniformity in the axial direction. The non-uniformity in the circumferential direction is due to the presence of a pressure and suction zone on the leading and trailing side of the spider arms respectively. The circumferential variation predicted by the CFD was experimentally verified by Bach [24], who made PIV measurements in the interpole region as shown in Fig. 3-8.
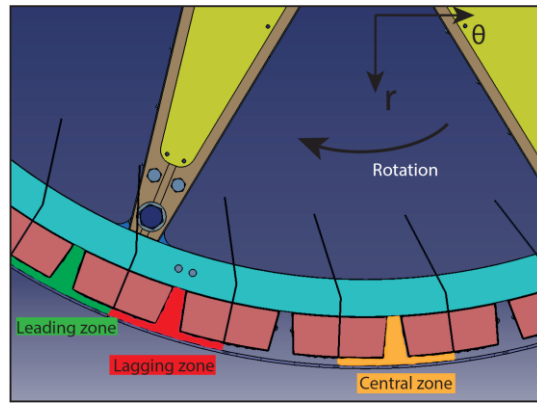
Figure 3-8: Three circumferential regions created by the spider arms [2]

The results by Bach indicate that the central zone experiences the highest flow exiting the rotor, followed by the leading and then the lagging zones.

The results from the CFD simulations and PIV measurements show that the anemometer must be able to operate at different flow conditions. Furthermore, the average measurement obtained by the anemometer must be insensitive to variations in flow velocity/velocity profile and inlet incidence angle.

Chapter 4
Overview of Measurement Techniques

The final part of the project's preliminary phase is the review of existing flow measurement techniques. All considered techniques were grouped into three categories: those that convert temperature to velocity, pressure to velocity, and all other methods. Ten different techniques distributed among those categories were considered. After a sufficient review, the techniques were filtered to proceed to the preliminary validation phase. To select the techniques with the best potential, a design specification list was made and, for each criterion, a rating varying from 0 (poor) to 5 (excellent) was assigned to each technique. The first iteration of technique filtering allowed for the selection of two measurement techniques. Although only one sensor type is needed in principle, developing two designs allowed for an alternative if complications were to arise for a given design in any of the subsequent phases.

4.1   Review of current techniques

As previously mentioned, two principal categories of sensors will be investigated: i) those that convert pressure to velocity, and ii) those that convert temperature to velocity. The first approach includes sensors such as the Pitot-static tube and the Venturi meter. The second method is comprised of hot-wire anemometry, hot-film anemometry, and thermal mass flow meters. Alternatives to thermal and pressure methods are classified herein as miscellaneous methods, and include: ultrasonic anemometry, vortex flow meters, turbine flow meters, drag flow meters, and electromagnetic flow meters. These methods have advantages and limitations when considering the characterization of the flow within the rotor rim ducts and once they are all considered, a new measuring device can be developed such that all the research objectives are met.

4.1.1   Pressure methods

This section considers the most common types of sensors that fundamentally convert a pressure measurement to velocity. The two most common types are Pitot-static tubes and Venturi meters, which rely on the same mathematical principle, but their application is very different.

4.1.1.1 Pitot-static tubes

Pitot-static tubes rely on the fundamental principle of Bernoulli`s equation (Bernoulli, 1738):

$$P + \frac{\rho U^2}{2} + \gamma z = Constant, \qquad (4.1)$$

where z is the elevation and γ is the specific weight ($\gamma = \rho g$). The above equation is only valid if the following four assumptions can be made:

  i.   Inviscid flow
 ii.   Steady flow
iii.   Incompressible flow
 iv.   Applied along a streamline

The first term in Eq. 4.1 is called the static pressure; the actual thermodynamic pressure of the fluid as it flows. The second term is called the dynamic pressure; the difference between the static pressure and the stagnation pressure. The dynamic pressure is a representation of the kinetic energy of the fluid particle. The third term is the elevation pressure; this term accounts for the particle weight as the elevation changes.

A Pitot-static tube is made using two concentric tubes attached to two pressure gages so that one can experimentally determine the pressure differential (ΔP) between the two locations. The center tube measures the stagnation pressure at its open tip, and the outer tube is made with several small holes at an appropriate distance from the tip so that they measure the static pressure. Neglecting the effect of elevation and solving for the velocity, one obtains from Bernoulli's equation:

$$V = \sqrt{2(\Delta P)/\rho}. \qquad (4.2)$$

The accuracy of the pressure measurements is highly dependent on the sensitivity of the transducers used. For high precision, fast response times and a digital output, diaphragm-type transducers are the preferred choice. However, high-range transducers give poor accuracy in flows with low velocities. These and other errors can occur if care is not taken when making velocity measurements with Pitot-static tubes. See the Handbook of Experimental Fluid Mechanics [27] for more details on this topic.

4.1.1.2 Venturi meters

Venturi meters infer a fluid's speed using Bernoulli's equation, and measure the flowrate through ducts by: i) placing a restriction in the pipe, and ii) measuring the pressure drop across the restriction.
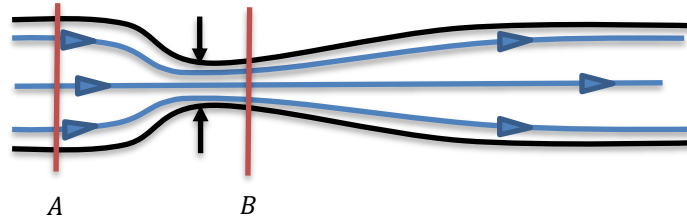
Figure 4-1: Venturi meter

As shown in Fig. 4-1, a differential pressure measurement is made between sections A and B. The low-velocity, high-pressure upstream location and the high-velocity, low-pressure downstream location, respectively. For a horizontal, steady, inviscid, and incompressible flow between section A and B, Bernoulli's equation simplifies to:

$$P_A + \frac{1}{2}\rho U_A^2 = P_B + \frac{1}{2}\rho U_B^2. \tag{4.3}$$

Using the continuity equation for constant density flow:

$$Q = A_A U_A = A_B U_B, \tag{4.4}$$

where Q is the volume flowrate and the velocity profiles at section A and B are uniform. Rewriting Bernoulli's equation by combining Eqs. 4.3 and 4.4 results in:

$$Q_{ideal} = A_B \sqrt{\frac{2(P_A - P_B)}{\rho(1 - (A_B/A_A)^2)}} = A_B \sqrt{\frac{2(\Delta P)}{\rho(1 - (\beta)^4)}}, \tag{4.5}$$

where β is the diameter ratio:

$$\beta = D_B/D_A. \tag{4.6}$$

Therefore, for a given flow geometry the flow rate (Q) is related to the square root of the pressure difference:

$$Q \sim \sqrt{\Delta P}. \tag{4.7}$$

In reality, the actual flow rate will be smaller than the theoretical result because of the differences between viscous flows and the assumptions underlying Bernoulli's equation. However, a properly designed Venturi meter will keep head losses to a minimum by providing both a smooth contraction, which eliminates separation ahead of the throat, and a very gradual expansion downstream of the throat, which eliminates separation in the decelerating portion of the meter. In well-designed Venturi meter, the head loss is due to friction rather than flow separation. A more detailed explanation about this method is given in the text by Munson [28].

4.1.2 Thermal methods

This section considers the most common types of sensors that convert a temperature measurement to velocity. The three most common types are: hot-wire anemometers, hot-film anemometers, and thermal mass flow meters. All three rely on the conservation of energy of a flowing fluid over a heating element. Hot-wires and hot-films are closely related, but their fabrication process alters how they are used, and what they measure. The third method is slightly different and is often used in an industrial context, such as the automotive industry to measure the air intake to the cylinders of a combustion engine.

4.1.2.1 Hot-wire anemometry

Hot-wires were one of the first turbulence measurement tools, in addition to being well understood and of low-cost. The physical principle of hot-wires is that the velocity of a flowing fluid over a small electrically heated sensor can be measured by sensing the changes in convective heat transfer over the sensor. This can be shown by looking at the energy balance over a hot-wire (neglecting radiation):

$$\rho_w c_w A_w \frac{\partial T_w}{\partial t} = \frac{I^2 \chi_w}{A_w} - \pi D_w h (T_w - T_\infty) - k_w A_w \frac{\partial^2 T_w}{\partial x^2}, \tag{4.8}$$

which is a function of the specific heat (c), temperature (T), area (A), time (t), current (I), electrical resistivity (χ), diameter (D), convective heat transfer coefficient (h), thermal conductivity (k), axial position (x), and the subscript w stands for wire. For every

instant in time, the convective heat transfer is balanced by the conduction losses, and the electrical energy injected into the wire. A well designed hot-wire avoids conduction losses to the prongs by having: i) a wire with a high aspect ratio and ii) a wire with low thermal conductivity. Thus, the governing steady state equation for hot-wires is:

$$\frac{I^2 \chi_w}{A_w} = \pi D h (T_w - T_\infty).$$

(4.9)

The heat transfer over the wire can be related to the flow velocity by a relationship of the form of:

$$Nu = \mathcal{A} + \mathcal{B} Re^n.$$

(4.10)

From his classical experimental and theoretical work in hot-wires, King (1914) proposed that the convective heat transfer is expressed as:

$$Nu = \mathcal{A} + \mathcal{B}\sqrt{Re},$$

(4.11)

where $\mathcal{A}$ and $\mathcal{B}$ are empirical calibration constants for each fluid. Therefore, for a given sensor and fluid, there are three unknowns, the wire temperature (T_w), the flow velocity (U), and the current (I). To find the parameter of interest (U), one typically keeps the wire temperature constant, this is referred to as Constant Temperature Anemometry (CTA). It is sometimes beneficial to cast Eq. 4.10 in terms of the anemometer outputs as:

$$E^2 = \mathcal{A} + \mathcal{B} U^n,$$

(4.12)

where E is the anemometer output voltage. Eq. 4.12 is only valid if the fluid properties and the wire resistance remain constant. A more detailed explanation of all the intricacies of hot-wire anemometry is given in the text by Bruun [29].

4.1.2.2 Hot-film anemometry

Hot-films are very similar to hot-wires but, they differ in the way they are manufactured and in what they measure. Hot-films are manufactured by depositing a thin platinum film (about 0.1μm thick) on a quartz substrate and coating it with a layer of quartz alumina, which electrically insulates the film and offers mechanical and chemical protection. It is because of this protection that hot-films can be used in water or flows with contaminants. Hot-films come in different shapes: cylindrical, conical, and flush-mounted.

Hot-films are typically used for near-wall and skin-friction measurements. These types of measurements are of interest in heat transfer predictions and turbulence modeling. In turbulent boundary layers with no pressure gradients, the law of the wall applies, thus in the inner region, the mean velocity and the three components of the fluctuating velocity are governed by the viscous length scale. Under steady state conditions, a hot-film under a thermal boundary layer operating in CTA mode will give a similar expression as Eq. 4.12 as described in Bruun [29]:

$$E^2 = \mathcal{A} + \mathcal{B}\tau_W^{1/n}, \quad (4.13)$$

where n (greater than 3) increases with the hot-film-to-fluid thermal conductivity.

4.1.2.3 Thermal mass flow meters

Thermal mass flow meters rely on the principle of conservation of energy of a flowing fluid over a heating source to infer the mass flow rate of the fluid. These devices are typically used to measure the mass flow rate of gases. There are two main types of thermal mass flow meters: heated-tube flow meters (shown in Fig. 4-2) and the immersion-probe flow meters.
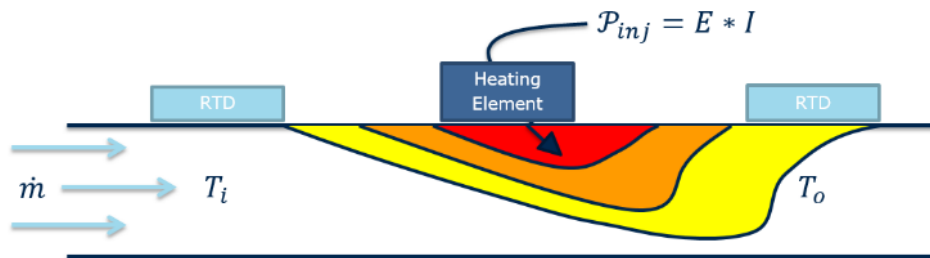
Figure 4-2: Sketch of a thermal mass flow meter

As shown in Fig. 4-2, a temperature measurement (T_i) is taken at an upstream location. Then farther downstream a heating source injects energy into the flow. This is typically done through resistance heating, where a voltage is imposed and a current is measured. From this information, the rate of energy injection $(\mathcal{P}_{inj})$ can be inferred. Downstream of the heating element a second temperature measurement (T_o) is then taken. Thus, from the temperature difference and the rate at which the energy was injected into the flow, one can infer the mass flow rate $(\dot{m})$ by using the following equation:

$$\mathcal{P}_{inj} = \dot{m}c_p(T_o - T_i). \tag{4.14}$$

As indicated by Eq. 4.14, the specific heat at constant pressure, which depends on the fluid and the temperature, must also be known. As shown in Fig. 4-2, typically the temperature difference is measured directly using Resistance Temperature Detectors (RTDs). The main challenge with this technique is how one obtains the second temperature measurement if the temperature profile at the second location is non-uniform. Thus, one must ideally take the second temperature measurement at a location far enough downstream allowing for the temperature profile to become uniform.

4.1.3 Miscellaneous methods

This section briefly considers other common classes of sensors that do not fall in the previous two categories, but that could be applied in the present context. A more detailed explanation of these techniques that goes beyond the scope of this discussion is given in the text by Tavoularis [30].

4.1.3.1 Ultrasonic anemometry

Ultrasonic flow meters use high-frequency (~10 MHz) pressure (i.e. sound) waves to infer the flow rate of liquids in pipes. There are two methods of achieving this: i) Doppler flow meters and ii) time-of-flight meters.

As shown in Fig. 4-3, Doppler flow metes are made with two piezoelectric crystals: a transmitter (T), which transmits an ultrasonic wave through the geometry of interest, and a receiver (R), which receives the reflected ultrasonic wave by particles or gas bubbles transported by the flowing fluid:
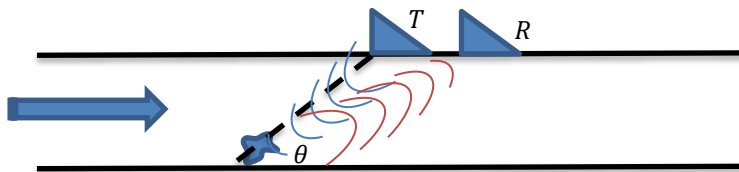
Figure 4-3: Sketch of the basic principle of Doppler flow meters

The frequency (f_r) of the reflected sound is offset from the frequency (f_t) of the transmitted sound by an amount Δf, called the Doppler shift, which is proportional to the velocity (U) of the deflected object, such that:

$$\Delta f = f_t - f_r = \frac{2f_t \cos(\theta)}{C} U, \qquad (4.15)$$

where C is the speed of sound. In practice, the device is calibrated to provide an output equal to the average velocity of the fluid in the pipe, assuming the flow is fully developed.

The time-of-flight flow meter is made with two sets of externally mounted piezoelectric transducers. Each transmitter emits sound waves towards their corresponding receiver; one set is located upstream while the other is located downstream, as shown in Fig.4-4:
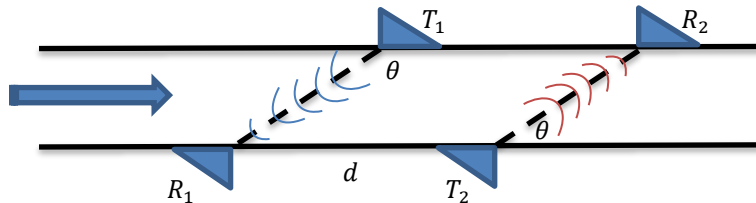
Figure 4-4: Sketch of the basic principle of time-of-flight flow meters

Since sound waves are transported by the flowing fluid, the sound waves travel faster downstream than upstream, and the frequency of pulsation of the two signals differs by:

$$\Delta f = \frac{\cos(\theta)}{d} U, \qquad (4.16)$$

where d is the distance between the pair of transducers. This configuration makes the flow measurement independent of the speed of sound (and thus temperature).

4.1.3.2 Vortex flow meters

The main component of the vortex-shedding flow meter is a bluff body immersed in the flowing fluid as shown in Fig. 4-5.

Figure 4-5: Sketch of a vortex flow meter (top view)

This concept is based on the periodic shedding of vortices (von Karman vortex street) from the edges of the object occurring at a frequency, f (in cylces per second). This frequency is related to the frontal width of the object (H) and the flow velocity (U). These parameters can be combined into a dimensionless parameter called the Strouhal number describing the shedding frequency:

$$St = \frac{Hf}{U}.$$

(4.17)

The shedding frequency is usually detected by a piezoelectric transducer. For vortex flow meters in pipes, a very small wand-shaped object typically passes through the pipe and is inserted inside the bluff body, as shown in Fig. 4-6. The section outside the flow is connected to a piezoelectric transducer that will measure the vibrations which can be converted into a frequency.
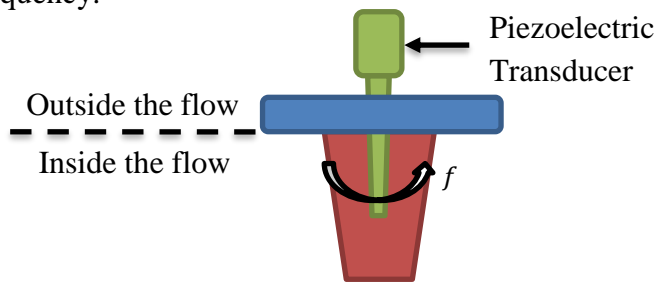
Figure 4-6: Sketch of a vortex flow meter (front view)

For a Reynolds number greater than 5,000, the Strouhal number remains constant (in the range of 0.14-0.21) and thus independent of the velocity (U).

4.1.3.3 Turbine flow meters

There are many types of turbine flow meters. These devices typically use either a gear system or an electrical motor. The gear-type flow meters use mechanical gear systems, which are mechanically driven by a gear mounted on the rotor shaft. This shaft, in turn, drives a mechanical readout which may display the flow rate or speed of the flow (similar to an automotive speedometer or odometer). The electrical motor type is very similar, but has a small motor with a shaft connected to the impeller, as shown in figure 4-7(a).
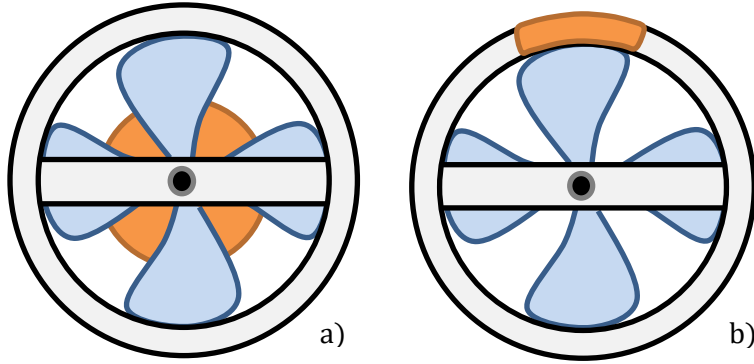
Figure 4-7: Turbine flow meter with an electric motor (a) and a modified turbine flow meter with an electromagnetic pickup (b)

As the impeller spins it rotates the shaft, which changes the electrical resistance of the motor, which can be related to the airflow rate of the moving fluid. An alternative type of turbine flow meter uses electromagnetic pickups so that the airflow rate is proportional to the angular velocity of an immersed rotor. The rotor is connected to a shaft allowing it to freely rotate about it. As the flowing fluid passes through the vanes of the rotor, it causes it to spin. The passage of each blade is then sensed electromagnetically by an externally mounted sensor, as shown in figure 4-7(b). Then the flow rate can be inferred by:

$$Q = C * N_{pls},$$ (4.18)

where N_{pls} is the number of pulses per unit time provided by the sensor and C is a calibration constant, which is dependent on the impeller design and size, the pipe diameter, and the number of blades.

4.1.3.4 Drag flow meter

Drag flow meters are based on the relationship between drag $\left(D_f\right)$ on an immersed bluff body and the free-stream velocity (U):

$$D_f = \frac{1}{2} C_D \rho A U^2,$$ (4.19)

where, A is the frontal area of the object or the area, C_D is the coefficient of drag, and ρ is the fluid density. In practice, the bluff body is a disk inserted in a pipe mounted on a support

instrumented with strain gauges or linear variable-differential transforms (LVDTs), which measure the drag force through deflection.

4.1.3.5 Electromagnetic flow meters

Electromagnetic flow meters provide the flow rate of electrically conducting liquids in pipes. Their underlying theory of operation is from Faraday's law of electromagnetic induction, which states: *When a conductor with length l moves with speed U in a direction normal to the direction of the magnetic field with magnetic flux density B, an electric potential E is generated across it such that:*

$$E = BlU. \tag{4.20}$$

In practice, these flow meters are insulated pipe sections of the same diameter as the pipe, but they are surrounded by an alternating, or pulsed magnetic field having two surface electrodes embedded in the wall across the pipe section normal to the magnetic field direction. The electrical potential between these electrodes is related to the volume flow rate (Q) as follows:

$$E = \frac{4CB}{\pi D}Q, \tag{4.25}$$

where C is a constant coefficient and D is the pipe diameter.

4.2   Advantages and disadvantages of the reviewed techniques

All techniques in the three categories have their respective advantages and disadvantages when considering their application to characterize the flow in the rotor rim ducts of a hydroelectric generator. For example, pressure based techniques were robust enough to survive the harsh environments found in the rotor but, both the Pitot-static tube and the Venturi meter would need major adjustments to fit inside the confined space of a rotor rim duct. When considering the thermal methods, both hot-films and thermal mass flow meters are robust enough to survive the harsh environments whereas hot-wires are more fragile. Furthermore, hot-wires and hot-films give local (rather than average) quantities, as opposed to the thermal mass flow meter. The remaining techniques had similar advantages and disadvantages when considering their application to hydroelectric

generators. Some commonalities between these sensors where: i) the requirement for external sensors around the duct, and ii) their fragility. However, it is impossible to place sensors around the outside of a rotor rim duct, due to the geometry of the rotor. These techniques also had small moving parts or fragile sensors that would not survive the large centrifugal forces found on the rotor. To facilitate the filtering process, the advantages and disadvantages of each technique were collected in tables and are presented in the following sections.

4.2.1   Pressure methods in a hydroelectric generator

Table 4-1: Advantages and disadvantages of the pressure methods for the application

Pressure methods	Pitot-static tubes	Venturi meters
Advantages	Robust	Robust
	Small nozzles	Minimizes head losses
	Cost-effective	Average measurement
	Easy to operate	-
Disadvantages	Local measurement	Expensive
	Requires flow alignment	Large device
	Large tubing	Requires external sensors
	-	Velocity profile dependent

4.2.2   Thermal methods in a hydroelectric generator

Table 4-2: Advantages and disadvantages of the thermal methods for the application

Thermal methods	Hot-wire anemometry	Hot-film anemometry	Thermal mass flow meters
Advantages	Small	Small	Robust
	Cost-effective	Robust	Simple
	One can infer both temp. and velocity	-	Captures wide speed ranges
	Continuous signal	-	Average measurement
Disadvantages	Fragile sensor	-	Only immersion-type is applicable
	Contaminants alter its performance	Complex frequency response	Uniform exit temp. requires long duct
	Local measurement	Local measurement	Difficult to measure exit temperature
	-	Expensive	Flow Intrusive

4.2.3　Miscellaneous methods in a hydroelectric generator

Table 4-3: Advantages and disadvantages of the misc. methods for the application

Miscellaneous methods	Ultrasonic anemom.	Vortex flow meters	Turbine flow meters	Drag flow meters	Electromag. flow meters
Advantages	Non-invasive	Good adaptability	Cost-effective	Small	High accuracies (>0.5%)
	Cost-effective	Robust bluff body	Captures wide speed ranges	Sensitive and multi-directional	Non-invasive
Disadvantages	Fragile sensors	Fragile sensors	Fragile sensor	Fragile sensor	Requires conductive fluid
	Requires developed flow	Re $>5{\cdot}10^3$, St is constant	Small moving parts	Re $>10^3$, C_D is constant	Bulky and heavy system
	Requires external sensors	Requires external sensors	Flow intrusive	Local measurement	Requires external sensors
	-	Flow intrusive	-	-	Expensive

4.3　Technique filtering

Following a design meeting at the IREQ, a design specification list was made. This list contained all the design specifications that the ideal anemometer would possess. The list if given below:

1. Be able to resist a centrifugal force of 300 *g*
2. Be able to fit inside a 51 by 12.7 mm duct
3. Be able to withstand temperatures of 45℃
4. Have an operational life greater than one week
5. Be resistant to contaminants (oil and dust specifically)
6. Give an average measurement (i.e. velocity, flow rate, or mass flow rate) of the flow in the rotor rim ducts
7. Be easy to install and operate

8. Have a robust design with low risk of losing small components

9. Have a measurement precision greater than 10%

10. Induce minimum flow blockage

11. Facilitate data transfer

12. Have a low manufacturing cost

After establishing the design constraints, they were subsequently ranked as critical, important, and preferable. Items 1-5 were deemed critical, items 6-9 were deemed important, and items 10-12 were deemed preferable. Critical specifications are essential in the development of the anemometer, while important specifications should be sought, but the method should still be considered if they are not met.

To narrow down the options, it was decided to rank all the measuring techniques on a scale from 0-5 for each of their design specifications. A value of zero implies that the method did not seem capable of meeting the design specification, whereas a value of 5 implied that it would be highly probable to do so. The results of this exercise are presented in Table 4-1.

Table 4-4: Qualitative analysis of the reviewed techniques

Design specs. \ Technique	Pitot-static tubes	Venturi meters	Hot-wire anemometry	Hot-film anemometry	Thermal mass flow meters	Ultrasonic anemometry	Vortex flow meters	Turbine flow meters	Drag flow meters	Electromagnetic flow meters
Resist centrifugal force	5	5	5	5	5	2	1	1	1	2
Fit in 51 by 12.7 mm duct	3	1	5	5	4	0	0	4	4	0
Temp. resistant (45℃)	5	5	5	5	5	5	5	5	5	5
Life span ($> 1\ week$)	5	5	4	4	5	4	4	3	3	4
Resistant to contaminants	3	4	1	5	5	5	4	4	5	5
Average measurement	1	5	3	1	5	4	3	3	3	5
Easy to install and operate	2	4	4	3	4	0	0	5	3	0
Robustness	4	4	3	4	4	2	2	2	3	4
Measurement precision	2	4	4	4	4	4	3	3	3	5
Minimum flow blockage	3	1	4	4	2	5	2	2	3	5
Easy data transfer	4	4	4	3	3	3	4	4	3	3
Low cost	5	1	4	2	4	1	1	4	1	0
SUM	42	43	**46**	**45**	**50**	35	29	40	37	38

It is important to note that the ranking considered here is a subjective judgment based upon the operating conditions under which the type of sensor would be exposed. Based on the evaluation criteria the best two options were as follows:

1. Thermal Mass Flow Meter
2. Hot-Wire Anemometry

Therefore, only these two techniques will be considered in the subsequent chapters.

4.3   Technique justification

The chosen techniques were both thermal based methods. Their ability to withstand the harsh environments, fit within the confined region of the rotor rim, and their measurement precision made these techniques more viable than the others. Ultimately, only one design is needed, but having two options would increase the chances of obtaining a working anemometer at the end of the validation phase, as unforeseen issues could arise in the design process.

Consequently, both the thermal mass flow meter and hot-wire anemometry techniques were kept for the design phase. The main advantages of hot-wire anemometry are its design adaptability and low cost. Some of its disadvantages were its sensitivity to flow contamination and its inability to obtain an average measurement. However, if a hot-wire is extended over the length of the rotor rim duct, its spatial resolution would increase. The main advantages of a thermal mass flow meter are its adaptability and capability of obtaining an average measurement. Some disadvantages of this technique are its induced flow blockage and the difficulty in obtaining the correct outlet temperature. However, it seemed feasible to undertake the latter aspects and for this reason an analytical validation of both thermal methods was performed.

Chapter 5
Analytical Validation

The first step of the validation phase was analytical in nature. The scale model CFD simulation results provided a broad overview of the physics of the flow in the rotor rim ducts, and rough estimates for important quantities. Based on this information, a feasibility analysis of both hot-wire anemometry and thermal mass flow meters was conducted. The goal of this analysis was to answer questions posed at the end of the preliminary phase regarding the potential performance of these techniques. To this end, the performance of each technique, subject to different geometrical, mechanical, or thermal parameters such as wire diameters, material type, and energy dissipation rates was evaluated. This analysis provided the basis for the subsequent preliminary experimental validation.

5.1   Preliminary feasibility analysis of hot-wire anemometry

Hot-wire measurements are typically made in flows where the velocity profile is non-uniform. But since the hot-wire is small compared to the variation in the velocity profile, the hot-wire is effectively exposed to a uniform profile. However, if the length of the hot-wire is of the order of the variations in the velocity profile (as shown in Fig. 5-1), then one must investigate whether the average measurements are dependent on the velocity profile.
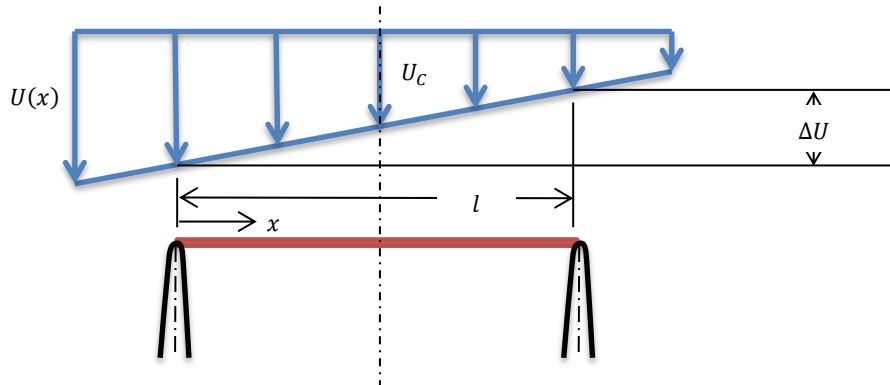
Figure 5-1: A hot-wire exposed to a non-uniform velocity profile

A Constant Temperature Anemometer (CTA) measures the windspeed by equating the convective heat transfer to the electrical power inputted into a flow by applying a voltage (E) such that the wire temperature, and thus its resistance (R_w), remain constant. Thus, to investigate how dependent the output voltage is on the velocity

profile, a numerical analysis was conducted. In this analysis, three parameters were varied, as follows:

     i.   Velocity profile: uniform, linear, parabolic, and blockage

    ii.   Average velocity: 7 and 10 m/s

   iii.   Wire diameter: 50 – 500 µm

For all scenarios, the length of the wire was kept equal to 40 mm as it was estimated that for a 51 mm wide duct, a minimum of 5.5 mm of support material on either side of the wires was required to hold them in place. Each of the velocity profiles were imposed along the length of the wire at the specified average velocity such that: i) the uniform velocity profile had a zero gradient, ii) the linear velocity profile varied between 0 m/s to twice the average velocity, iii) the parabolic velocity profile varied from 0 m/s at both ends of the wire to twice the average velocity at the center, and iii) the blockage velocity profile was a step profile where the percentage blockage is set at 5% of the mean flow velocity over 20% of the length of the wire. The latter was investigated to mimic a recirculation zone that could be present in a rotor rim duct. The uniform profile was chosen as the reference case to investigate the evolution of the output voltage with an increasing velocity gradient (provided by the remaining profiles). This study was performed by numerically discretizing the governing unsteady convective-diffusion equation with a source term (S) corresponding to the power injected into the wire, and by determining the source value required to obtain a wire temperature of 200°C, with a far-field temperature (T_∞) of 20°C. For practical reasons, the velocity profile's effect on the wire resistance was quantified instead of its effect on the output voltage. Furthermore, in this analysis, both the wire diameter and average velocity were varied. The diameter was varied as it was expected that larger wire diameters could potentially dampen out the effects of large velocity gradients. The average velocity was also varied to observe its effect on the wire resistance. This naturally led to two different numerical experiments at two different speeds (4 in all), as detailed here below:

     i.   Keep the wire diameter constant and change the velocity profile

    ii.   Keep the velocity profile constant and change the wire diameter

These two sets of experiments were conducted numerically on a simplified problem.

5.1.1 Numerical hot-wire anemometry analysis
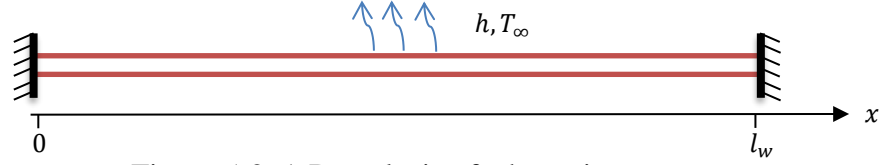
Figure 5-2: 1-D analysis of a hot-wire

The simplified problem for the numerical analysis consisted of a very long ($l_w \gg r_w$) hot-wire with thermally insulated ends and a uniform current is shown in Fig. 5-2. Thus, it was assumed that:

i.   the heat transfer is 1-D,

ii. there is a uniform source, and

iii. the properties are constant

with the following Neumann boundary conditions:

i. $\partial T(0,t)/\partial x = 0$

ii. $\partial T(l_w,t)/\partial x = 0$

The resulting governing differential equation for a hot-wire is given by Bruun [29]:

$$k_w A_w \frac{\partial^2 T_w}{\partial x^2} + \frac{I^2 \chi_w}{A_w} - \pi D_w * h(T_w - T_\infty) - \rho_w c_w A_w \frac{\partial T_w}{\partial t} = 0, \qquad (5.1)$$

where the subscript w stands for wire, k is the thermal conductivity, A is the cross-sectional area, x is axial distance along the wire, D is the diameter, χ is the electrical resistivity, h is the convective heat transfer coefficient, ρ is the density, c is the specific heat, and t is time. To better determine the parameters that affect the relation between the wire resistance and the velocity profile along the wire, some manipulations of Eq. 5.1 are required. One can re-express the second term of the equation, as follows:

$$\frac{I^2 \chi_w}{A_w} = \frac{I^2 \left(R_w A_w / l \right)}{A_w} = \frac{I^2 R_w}{l_w} = \frac{\mathcal{P}}{l_w} = S \qquad [W/m]. \qquad (5.2)$$

This term is the source term arising from the electrical current or the power ($\mathcal{P}$) per unit length of the wire, which will be denoted as S. Thus, for a wire of fixed length, the source

term can be expressed as the power injected into the wire. Applying this change, and dividing by $k_w A_w$, one obtains:

$$\frac{\partial^2 T_w}{\partial x^2} + \frac{S}{k_w A_w} - \frac{\pi D_w * h}{k_w A_w}(T_w - T_\infty) - \frac{1}{\alpha_w}\frac{\partial T_w}{\partial t} = 0, \quad (5.3)$$

where α is the thermal diffusivity. This specified mathematical problem can be solved numerically by: i) separating the wire into three distinct sections, ii) discretizing each section into nodes, and iii) applying the finite difference technique.
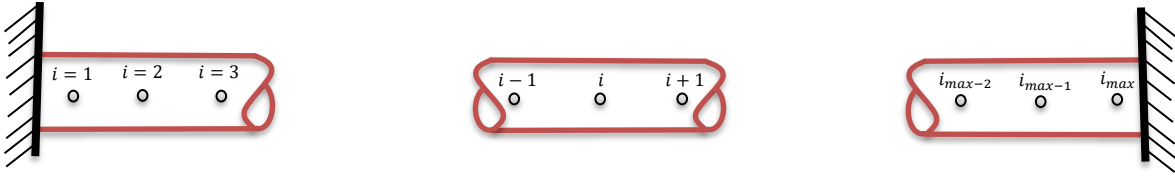
Figure 5-3: Discretization scheme for left, middle and right ends of the 1D hot-wire

Starting with the center section, the second-order derivative in Eq. 5.3 can be discretized using a second-order central differencing scheme as follows:

$$\frac{\partial^2 T_w}{\partial x^2} = \frac{T_{i+1}^n - 2T_i^n + T_{i-1}^n}{(\Delta x)^2}. \quad (5.4)$$

One can also discretize the unsteady term in Eq. 5.3 using a first-order explicit scheme:

$$\frac{\partial T_w}{\partial t} = \frac{T_i^{k+1} - T_i^k}{\Delta t}. \quad (5.5)$$

Substituting Eqs. 5.4 and 5.5into Eq. 5.3, one obtains:

$$\left[\frac{T_{i+1}^k + T_i^k + T_{i-1}^k}{(\Delta x)^2}\right] + \frac{S}{kA} - \frac{\pi D * h}{kA}(T_i^j - T_\infty) - \frac{1}{\alpha}\left[\frac{T_i^{k+1} - T_i^k}{\Delta t}\right] = 0. \quad (5.6)$$

Multiplying Eq. 5.6 by $\alpha\Delta t$ and rearranging results in:

$$T_i^{k+1} = \left[T_{i+1}^k + T_i^k + T_{i-1}^k\right]\left[\frac{\alpha\Delta t}{(\Delta x)^2}\right] + \frac{S}{KA}[\alpha\Delta t] - \frac{\pi D * h\alpha\Delta t}{kA}(T_i^k - T_\infty) + T_i^k, \quad (5.7)$$

where two important dimensionless parameters arise:

$$Fo = \frac{\alpha \Delta t}{(\Delta x)^2} \qquad (5.8)$$

and

$$Bi = \frac{h\Delta x}{k}. \qquad (5.9)$$

They are the Fourier number (Eq. 5.8) and the Biot number (Eq. 5.9). One can rearrange Eq 5.7 such that:

$$T_i^{k+1} = Fo\left[T_{i+1}^k + T_{i-1}^k + T_S\right] + [1 - 2Fo]T_i^k - (\mathcal{N}BiFo) * \left[T_i^k - T_\infty\right], \qquad (5.10)$$

where the following parameters are defined:

$$T_S \equiv \left(\frac{S}{KA}\right)(\Delta x)^2 \qquad (5.11)$$

and

$$\mathcal{N} \equiv \frac{\pi D \Delta x}{A}. \qquad (5.12)$$

T_S represents the increase in temperature due to the source term, and $\mathcal{N}$ is a dimensionless term based on the geometry of the wire. Discretizing the equation at its left boundary is very similar, except the boundary condition must be applied. The imposed boundary conditions are those corresponding to an adiabatic tip such that:

    i.   There are no end losses

    ii. $T_0 = T_2$ ensures the zero-gradient boundary condition

Therefore, applying a second-order central differencing to the left end ($i = 1$) gives:

$$\frac{\partial^2 T_w}{\partial x^2} = \frac{T_2^k - 2T_1^k + T_0^k}{(\Delta x)^2} = \frac{2T_2^k - 2T_1^k}{(\Delta x)^2}. \qquad (5.13)$$

Applying the boundary conditions and Eq. 5.14 results in the equation for the left end of the wire:

$$T_1^{k+1} = Fo[2T_2^k + T_S] + [1 - 2Fo]T_1^k. \qquad (5.14)$$

The same principle is applied to the right end ($i = i_{max}$) of the wire:

$$T_{i_{max}}^{k+1} = Fo\left[2T_{i_{max}-1}^k + T_S\right] + [1 - 2Fo]T_{i_{max}}^k. \qquad (5.15)$$

This set of Eqs. (5.10, 5.14, 5.15) were solved by discretizing the domain into 1,200 nodes (i) and using a simple for-loop in MATLAB to iterate over time (k). (No matrix inversion was required as it was explicit in time.) The source term was specified such that the reference case using a uniform velocity profile achieved an average wire temperature of 200°C. Then the problem was initialized by setting the wire at the ambient temperature and then exposing it to one of the other three velocity profiles. Convergence was obtained when the average wire temperature achieved a steady state temperature. Steady state was defined as the time when the time rate of change of the average wire temperature between two iterations is less than 10^{-3}:

$$\left| \frac{\sum_{i=1}^{N} T_i^k / N - \sum_{i=1}^{N} T_i^{k-1} / N}{\Delta t} \right| \leq 10^{-3}.$$

The relationship between the convective heat transfer coefficient and the velocity was established using the Nusslet number correlation of a cylinder in cross flow proposed by Zukauskas [31]:

$$Nu_D = (h l_w / k_w) = C Re_D^m Pr^n (Pr/Pr_s)^{1/4} \qquad (5.16)$$

$$0.7 \leq Pr \leq 500$$

$$1 \leq Re_D \leq 10^6,$$

where n is 0.37 if the Prandtl number is less than or equal to ten otherwise if the Prandtl number is greater than 10, n is 0.36. The values of C and m are dependent on the Reynolds number, as shown in Table 5-1:

Table 5-1: Constants for Eq. 5.16 for a cylinder in cross flow [31]

Re_D	C	m
$1 - 40$	0.75	0.4
$40 - 10^3$	0.51	0.5
$10^3 - 2 \cdot 10^5$	0.26	0.6
$2 \cdot 10^5 - 10^6$	0.076	0.7

All tested velocity profiles had the same average velocity of either 7 or 10 m/s. Fig. 5-4 shows the convective heat transfer coefficient profile corresponding to each velocity profile.
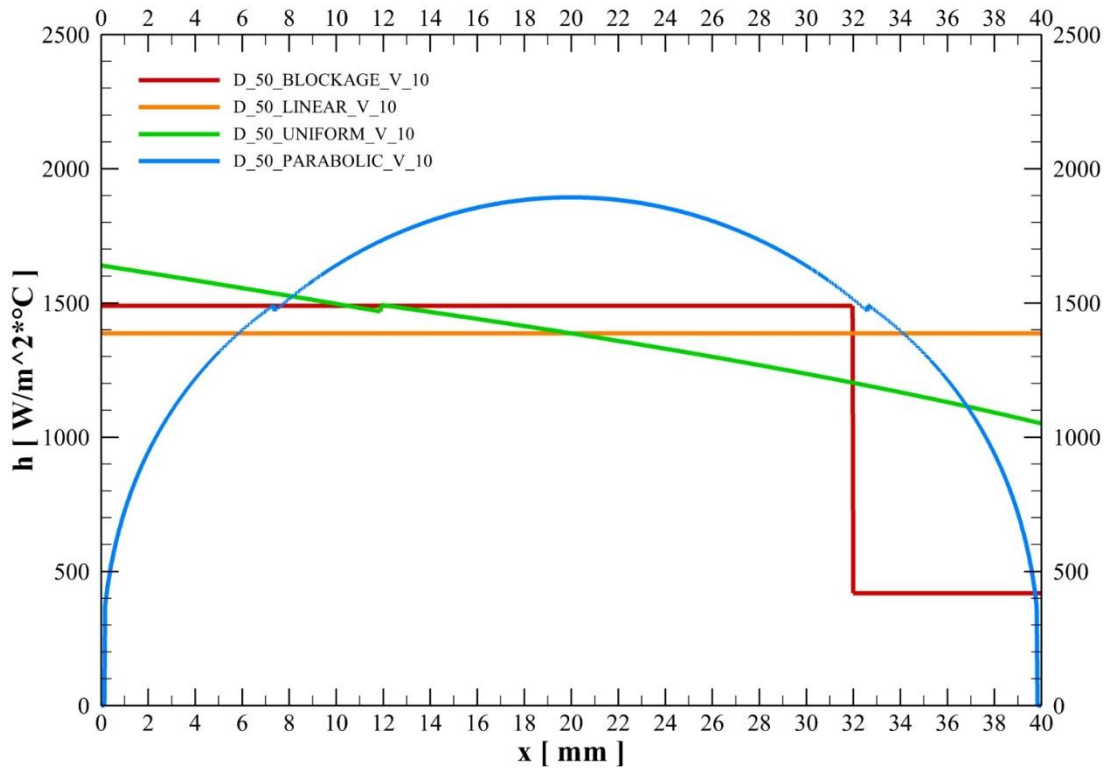
Figure 5-4: Convective heat transfer coefficients over a 40 mm wire exposed to velocity profile with an average velocity of 10 m/s

The small discontinuities visible in Fig. 5-4 result from the discontinuities in the correlation of Eq. 5.17. The numerical analysis ultimately concluded that the resistance change was not a strong function of the velocity change thus, only the results of the 10 m/s case will be presented here. Therefore, only two of the four scenarios will be presented: how the resistance varies with: i) velocity profile for a given wire diameter, and ii) with wire diameter for a given velocity profile.

The baseline resistance values and required power to obtain an average wire temperature of 200°C at 10 m/s for this analysis are presented in Table 5-2.

Table 5-2: Baseline resistance values at an average velocity of 10 m/s

Velocity profile	D_w [μm]	$\mathcal{P}$ [W]	$\bar{h}$ [W/m²K]	$\bar{T}_w$ [°C]	$\bar{R}_w$ [Ω]
Uniform	50	1.57	1387	200.36	1.85
	100	2.14	947	200.06	0.46
	200	3.03	669	200.28	0.12
	500	4.80	423	200.62	0.019

44

5.1.2 Wire resistance dependence on the velocity profile for a given diameter
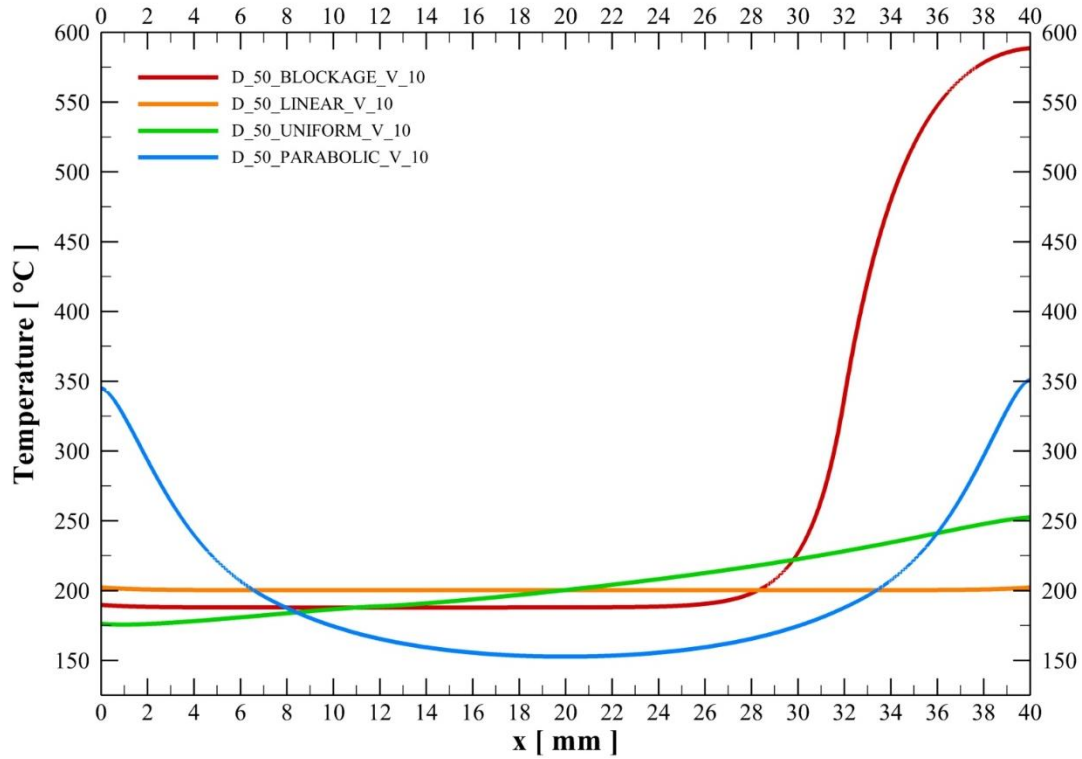
Figure 5-5: Temperature distribution in a 50 µm diameter hot-wire exposed to various velocity profiles with an average velocity of 10 m/s

Table 5-3: Change in wire resistance as a function of velocity profile

D_w [µm]	Velocity profile	$\mathcal{P}$ [W]	$\bar{h}\left[W/m^2K\right]$	$\bar{T}_w$ [°C]	$\bar{R}_w$ [Ω]	ΔR [%]
50	Uniform	1.57	1387	200.36	1.85	N/A
	Linear	1.57	1370	205.28	1.87	1.08
	Parabolic	1.57	1514	198.83	1.84	0.34
	Blockage	1.57	1274	260.27	1.09	13.08
100	Uniform	2.14	947	200.06	0.46	N/A
	Linear	2.14	938	205.58	0.47	1.19
	Parabolic	2.14	1057	193.41	0.46	1.45
	Blockage	2.14	897	247.59	0.51	10.37
200	Uniform	3.03	669	200.28	0.12	N/A
	Linear	3.03	662	206.04	0.12	1.21
	Parabolic	3.03	744	191.25	0.11	1.99
	Blockage	3.03	632	239.12	0.13	8.48
500	Uniform	4.80	423	200.62	0.019	N/A
	Linear	4.80	419	205.40	0.019	1.08
	Parabolic	4.80	470	186.86	0.018	3.24
	Blockage	4.80	397	227.03	0.020	5.95

For this analysis, each wire diameter (50, 100, 200, and 500 µm) was exposed to a different velocity profile. The graphical results of the first case are shown in Fig. 5-5. One observes that the average temperature of a wire having a small diameter (50 µm) will vary greatly with the velocity profile. The numerical results for the different wire diameters are summarized in Table 5-3.

From the results given in Table 5-3, one observes that a velocity profile with a larger velocity gradient will result in larger variations in the wire resistance, which will ultimately provide an inaccurate prediction of the average velocity.

5.1.3 Wire resistance dependence on diameter for a given velocity profile
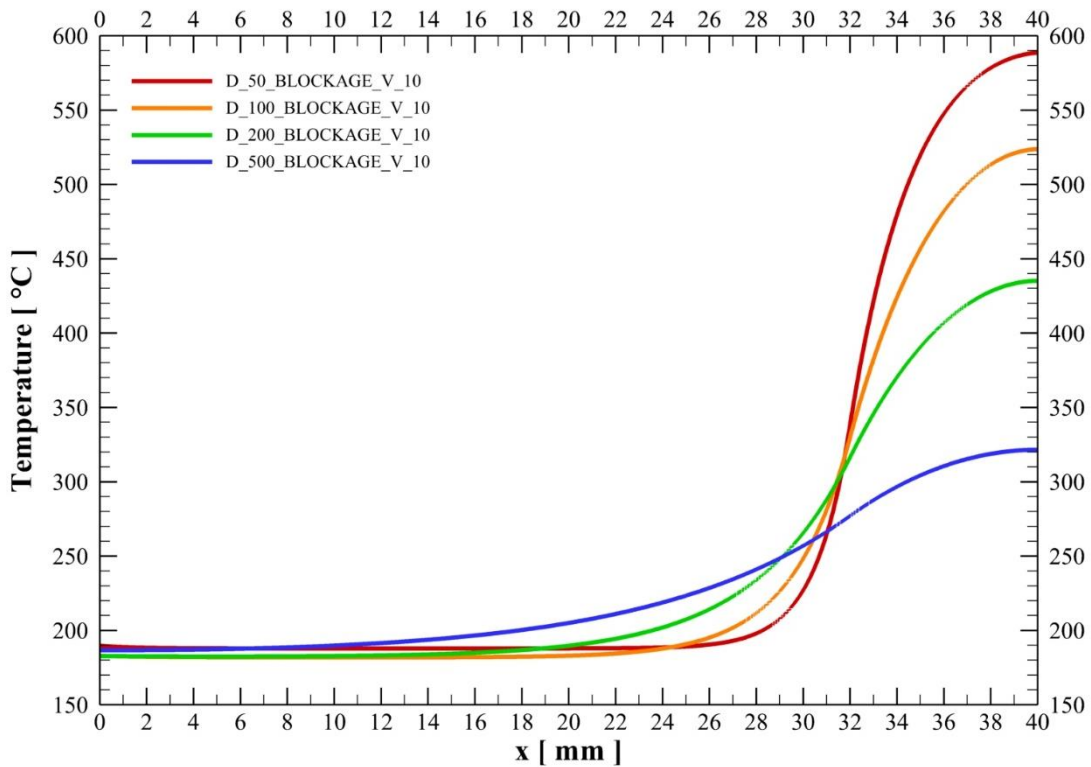
Figure 5-6: Temperature distribution in a hot-wire exposed to a 20% blockage velocity profile with an average velocity of 10 m/s for various wire diameters

For this analysis, the velocity profile was varied for each wire diameter. The graphical results for the 20% blockage velocity profile are shown in Fig. 5-6. One observes that the temperature of a wire exposed to a large velocity gradient will be more uniform as the

wire diameter increases due to an increase in the heat conduction along the wire. The numerical results for the different velocity profiles are summarized in Table 5-4.

Table 5-4: Change in wire resistance as a function of hot-wire diameter

Velocity profile	D_w [μm]	$\mathcal{P}$ [W]	$\bar{h}$ [W/m^2K]	$\bar{T}_w$ [°C]	$\bar{R}_w$ [Ω]	ΔR [%]
Linear	50	1.57	1370	205.28	1.87	1.08
	100	2.14	938	205.58	0.47	1.19
	200	3.03	662	206.04	0.12	1.21
	500	4.80	419	205.40	0.019	1.08
Parabolic	50	1.57	1514	198.83	1.84	0.34
	100	2.14	1057	193.41	0.46	1.45
	200	3.03	744	191.25	0.11	1.99
	500	4.80	470	186.86	0.018	3.24
Blockage	50	1.57	1274	260.27	1.09	13.08
	100	2.14	897	247.59	0.51	10.37
	200	3.03	632	239.12	0.13	8.48
	500	4.80	397	227.03	0.020	5.95

In general, one observes that increasing the wire diameter for flows with smaller temperature gradients did not significantly change the results. However, for the case of the blockage profile, increasing the wire diameter tends to smooth out the large temperature gradients, making the mean wire resistance value approach the value of the uniform case.

In summary, the results show that hot-wire anemometry is not a viable technique to characterize the flow in the rotor rim ducts, since it would yield difference resistance values for ducts having the same average velocity, but different velocity profile. Therefore, the error induced by attempting to make average measurements with this technique renders the approach unsuitable to characterize the flow in the rotor rim ducts.

5.2   Preliminary feasibility analysis of a thermal mass flow meter

One of the main challenges of the thermal mass flow meter technique is adapting the method to the rotor rim ducts. When comparing the case of flow within the rotor rims ducts to that in a pipe, one realizes that it is impossible to place a heating element around the rotor rim ducts, as it is done in heated-tube type thermal mass flow meters. Therefore, one must place a heating element within the rotor rim ducts (as in immersion-type thermal mass flow meters). Several designs were considered but, the concept that showed the most potential was the insertion of an array of wires across the duct. The concept for the heating element came from the fundamental problem in heat transfer of flow across a bank of tubes as presented by Incropera *et al* [31]. Thus, it was decided to place several rows of wires to sufficiently mix the heated flow, as shown in Fig. 5-7.
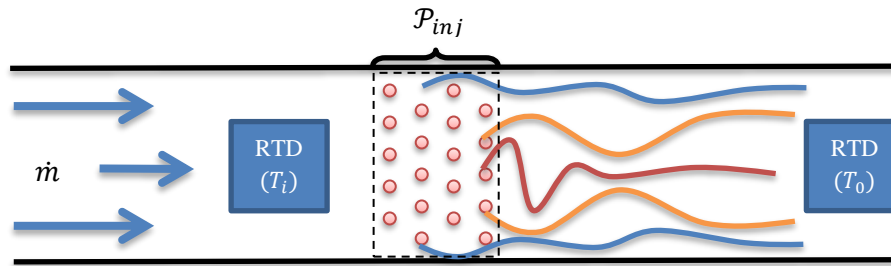
Figure 5-7: Proposed Immersion-type thermal mass flow meter inside a rotor rim duct

The concept features a staggered array of heated wires with Resistance Temperature Detectors (RTDs) measuring the inlet (T_i) and outlet (T_o) temperatures. A staggered arrangement was considered over an aligned one to enhance the mixing. However, many parameters still had to be determined, which are summarized below:

i.   Thermal parameters:
- $\Delta T = T_o - T_i$
- Surface temp. (T_S)
- Energy injected $\left(\mathcal{P}_{inj}\right)$

ii. Electrical parameters:
- Current (I)
- Voltage (E)
- Resistance (R)

iii. Physical parameters
- Wire material

iv. Geometric parameters:
- Wire diameter (D)
- Number of wires (N)

Each one of these parameters is dependent on another and due to practical implications. Thus, many assumptions must be made to close the set of equations that govern these parameters. The goal of this feasibility analysis is to determine if there exists a reasonable set of parameters that will allow for the characterization of the flow within the rotor rim ducts.

5.2.1 Parameter determination for a thermal mass flow meter design

To determine the set of parameters for the proposed design, the analysis of flow across tube banks was considered. To determine the mass flow rate using Eq. 4.14, one must measure the temperature difference between the inlet and outlet of the duct. Obtaining this quantity is the most challenging aspect. Thus, it was important to limit its error. The temperature difference between the inlet and the exit of the duct was fixed to 20°C, such that a measurement error of 1°C will result in a 5% error. By setting this value for the temperature difference, one can obtain the required power to sufficiently heat the flow for a given mass flow rate, as shown in Fig. 5-8.
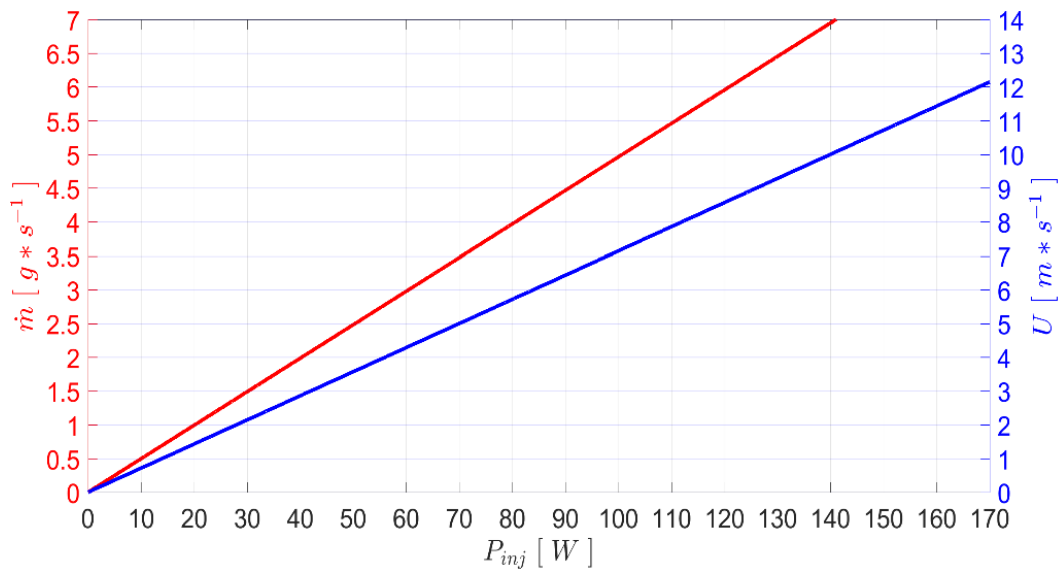
Figure 5-8: Mass flow rate or average velocity in a rectangular duct (12.2 mm by 49.6 mm) with a given injected energy required to obtain a 20°C temperature differential (using Eq. 4.14)

From the scale model CFD analysis, it was determined that the velocity in the rotor rim ducts varied between 1.4 and 12 m/s. Thus, the required corresponding power range is from 20 – 170 W. Knowing the power injected in the flow, one can estimate the wire surface temperature and the electrical parameters. The surface temperature will aid in the determination of the wire diameter and the number of wires, while the electrical parameters will assist in the determination of the current, voltage, resistance, and material choice, as well as showing the method's feasibility.

The wire surface temperature was set below 250°C, which was a subjective choice as there exists, for both the wire and the fixture that would hold it, several materials that can sustain this temperature. To determine the feasibility of obtaining a surface temperature below the specified value, one must obtain its relationship with the wire diameter and the number of wires. To do so, one must calculate the Nusselt number using the expression proposed by Zukauskas [31]:

$$\overline{Nu}_D = C_1 Re_{D,max}^m Pr^{0.36} \left(\frac{Pr}{Pr_s}\right)^{1/4}.$$ (5.17)

This equation is valid if:

$$N_L \geq 20$$
$$0.7 \leq Pr \leq 500$$
$$10 \leq Re_{D,max} \leq 2 * 10^6,$$

where N_L is the number of rows of wires. If the number is less than twenty, the following correlation was proposed by Incropera *et al* [31]:

$$\overline{Nu}_D|_{(N_L<20)} = C_2 \overline{Nu}_D|_{(N_L\geq20)},$$ (5.18)

where the following constants: C_1, m, C_2 are determined using the information provided in Tables 5-5 and 5-6.

Table 5-5: Coefficients C_1 and m for the Nusselt number expression [31]

Configuration	$Re_{D,max}$	C_1	m
Aligned	$10 - 10^2$	0.80	0.40
Staggered	$10 - 10^2$	0.90	0.40
Aligned	$10^2 - 10^3$	Approximate as a single cylinder	
Staggered	$10^2 - 10^3$		
Aligned ($S_T/S_L > 0.7$)*	$10^3 - 2 \cdot 10^5$	0.27	0.63
Staggered ($S_T/S_L < 2$)	$10^3 - 2 \cdot 10^5$	$0.35(S_T/S_L)^{1/5}$	0.60
Staggered ($S_T/S_L > 2$)	$10^3 - 2 \cdot 10^5$	0.40	0.60
Aligned	$2 \cdot 10^5 - 2 \cdot 10^6$	0.021	0.84
Staggered	$2 \cdot 10^5 - 2 \cdot 10^6$	0.022	0.84

*For $S\_T / S\_L < 0.7$, the heat transfer is inefficient and aligned tubes should not be used

Table 5-6: Coefficient C_2 for the Nusselt number expression bellow 20 rows [31]

N_L	1	2	3	4	5	7	10	13	16
C_2, Aligned ($Re_D > 1,000$)	0.70	0.80	0.86	0.90	0.92	0.95	0.97	0.98	0.99
C_2, Staggered ($Re_D > 1,000$)	0.64	0.76	0.84	0.89	0.92	0.95	0.97	0.98	0.99
C_2, Staggered ($Re_D < 1,000$)	0.83	0.88	0.91	0.94	0.95	0.97	0.98	0.99	1.00

The average convective heat transfer coefficient can be determined from the definition of the average Nusselt number:

$$\bar{h} = (k/D) \cdot \overline{Nu}_D \qquad (5.19)$$

It is important to mention that the convective heat transfer coefficients with the proposed Nusselt number correlation are known to have errors up to $\pm 15\%$, thus using this expression, one can only expect an estimate for the surface temperature. To determine the surface temperature, one must use Newton's cooling law and as explained in Incropera *et al.* [31], using $(T_S - T_i)$ as the temperature difference instead of the log mean temperature difference will over predict the heat transfer rate and thus under predict the wire surface temperature. However, given the approximate analysis herein an estimate of the wire surface temperature (T_s) for preliminary design purposes was found using the following expression:

$$T_S = \left(\frac{\mathcal{P}_{inj}}{\bar{h}(\pi l N D)}\right) + T_i, \qquad (5.20)$$

where l is the length of the wire, N is the number of wires and T_i is the inlet temperature.

For the proposed application, the power injected into the flow $\left(\mathcal{P}_{inj}\right)$ will be controlled by a power supply:

$$\mathcal{P}_{inj} = EI = I^2 R. \tag{5.21}$$

Thus, for a given bank of wires with a fixed resistance (R), one can determine the amount of current (I) needed to obtain the desired power. The resistance is a function of the wire length, diameter, and material properties:

$$R = \frac{\chi l}{A} = 4\frac{\chi l}{\pi D^2}, \tag{5.22}$$

where χ is the electrical resistivity, which is a linear function of temperature:

$$\chi = \chi_0\left[1 + L_{\alpha_0}(T_w - T_0)\right]. \tag{5.23}$$

In Eq. 5.23, the subscript 0 refers to quantities evaluated at a reference temperature of $0°C$, and L_{α_0} is the coefficient of resistivity of the wire material. Any highly conductive metal can be used for resistance heating, but most of them readily oxidize. A common material used for electric heating that does not oxidize is Nichrome: a nickel-chrome alloy. When Nichrome is heated to red hot temperatures it develops an outer layer of chromium oxide, which is thermodynamically stable in air and protects the material from further oxidation. Furthermore, its electrical resistivity does not vary as much with temperature when compared to other metals. Other advantages of Nichrome include its tensile strength and low thermal expansion. Thus, Nichrome was a good choice for the wire material of the heating element.

Once all the equations (Eqs. 5.17-23) are known, one can begin to determine the feasibility of the design by looking at their relationships. First, for a fixed wire length and power, the wire temperature is dependent on the wire diameter and the number of wires in the bank. If one increases the number of wires in the bank, or the wire diameter, the surface temperature will decrease. Second, if one increases the wire diameter, the required current increases, which leads into the design's feasibility, as large currents are dangerous and require expensive power supplies. When heating by the Joule effect, one imposes a voltage across a fixed resistance and then the current is measured to infer the power dissipated. Since the flow temperature difference was fixed in this analysis, the

required power for an average velocity was also fixed. Thus, depending on the resistance of the wire bank, a large voltage may be required. Such a requirement will make it very difficult and expensive to power the heating element. By combining quantitative and practical elements it was determined that the optimal configuration for the application was a bank of 30 wires having a diameter of 400 µm. This configuration required a reasonable amount of current and the wire surface temperature was below the specified value.

To show how the optimal geometrical parameters ($N = 30$, $D = 400\ \mu m$) were calculated, the number of wires is first fixed to 30 demonstrating that all other parameters (i.e. thermal, electrical, and physical) meet the specifications. Afterwards the number of wires is varied, showing that it was indeed correctly determined. For the operating power range, one can vary the wire diameter to obtain the required current for a bank of 30 Nichrome wires, as shown in Fig. 5-9.
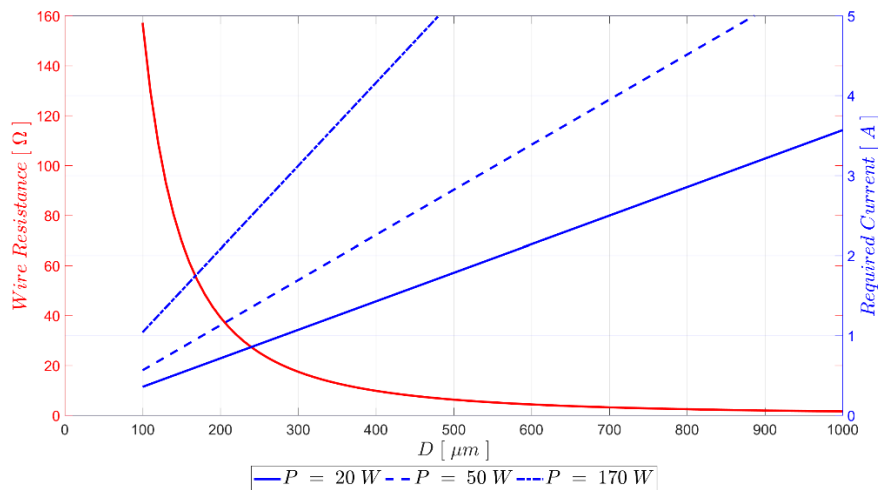
Figure 5-9: The resistance and current required to dissipate a given amount of power from a bank of 30 wires as a function of wire diameter

As shown above, for a bank of 30 wires with a 400 µm diameter dissipating 20, 50, or 170 W, the resistance is about 10 Ω and the required current is about 1.4, 2.3, or 4.2 A, respectively. Therefore, a 0-50 V/0-5 A (250 W) system can power this design, which is capable of measuring velocities from 1.4 to 12 m/s with a 20°C temperature difference between the flow's inlet and outlet. Once a feasible set of electrical parameters has been established, one must determine if they meet the surface temperature requirement. From

the analysis of Incropera *et al* [31], one can vary the wire diameter of the bank to determine its effect on the wire surface temperature, as shown in Fig. 5-10.
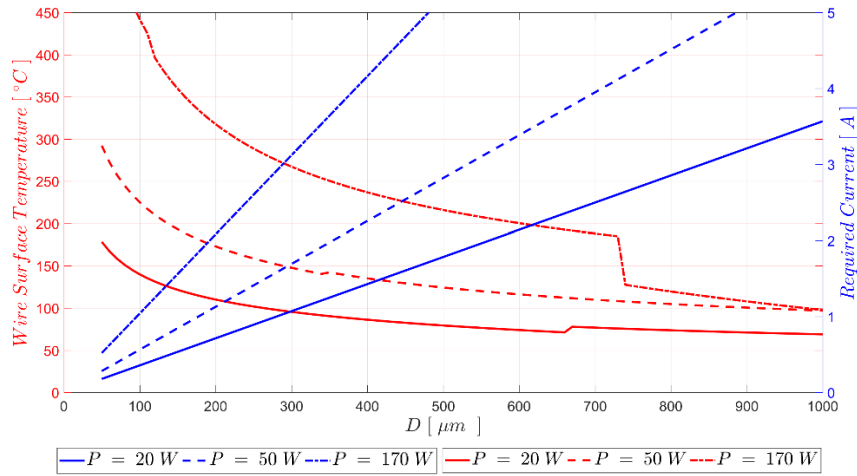
Figure 5-10: Wire surface temperature and required current to power a bank of 30 wires as a function of wire diameter

The discontinuity in the curves in Fig. 5-10 are due to the changes in the constants of Eq. 5.18, as illustrated in Table 5-4. The results show that for a bank of 30 wires with a 400 µm diameter dissipating 20, 50, or 170 W, the surface temperature is 86, 135, or 237°C respectively, which is below the specified 250°C. Now that all conditions have been met, one may vary the number of wires, as shown in Fig. 5-11, to determine whether the assumption was justified.
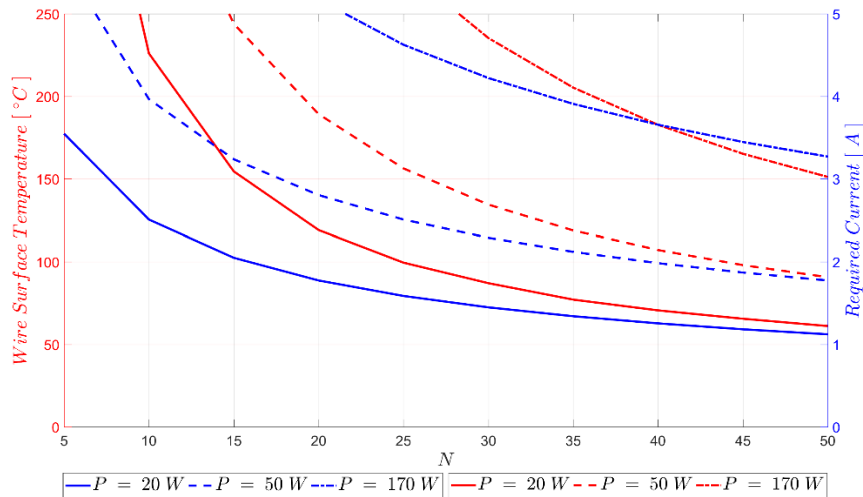
Figure 5-11: The wire surface temperature and required current to power a bank of *N* wires with or 400 µm in diameter

As depicted in figure 5-11, the wire surface temperature is below 250°C for all operating at a minimum of number of 30 wires.

5.2.2   Summary of the chosen parameters for the proposed design

In summary, the list of parameters that met the design specifications for the thermal mass flow meter design are listed in Table 5-7.

Table 5-7: Set of parameters for the proposed design

Thermal			Electrical			Physical	Geometric	
ΔT [°C]	T_S [°C]	$\mathcal{P}_{inj}$ [W]	I [A]	E [V]	R [Ω]	$Material$	D [μm]	N
20	<250	20-170	0-5	0-50	10	Nichrome	400	30

These results show that the thermal mass flow meter is a promising technique for the characterization of the flow in the rotor rim ducts of a hydroelectric generator. The proposed design for the heating element satisfies the geometrical constraints, is robust enough to survive the harsh environment in which it will be used, and the method can provide average quantities. The promising results allowed this method to proceed to the design phase. The only issue related to this method is how to accurately measure the fluid temperature downstream of the heating element. Consequently, an experimental test rig was built to overcome this problem.

Chapter 6
Experimental Validation

The final step of the validation phase is the experimental validation and it is split into four sections: i) experimental methodology, ii) procedures for the experimental validation, iii) description of the experimental setup, and iv) prototype design of a thermal mass flow meter. The first section explains the research approach taken (schematically depicted in Fig. 6-1), as well as, the description of the static model, emphasizing its necessity. The second section presents the procedure used to determine the downstream temperature measurement for a thermal mass flow meter. The third section describes the tools used to perform such measurements. The last section discusses the prototype design of the thermal mass flow meter. This section is brief, as Hydro-Québec holds proprietary right over the developed sensor's design thus, not all the details can be disclosed. The ultimate goal of this step is the development of a working prototype and an experimental method for its validation.

6.1   Experimental methodology

One of the main objectives of the DIAAA project is to make measurements on real hydroelectric generators to characterize the distribution of the flow in the rotor rim ducts. Unfortunately, measurements on real machines require shutdowns that would cause significant financial losses for the company. To resolve this issue while still being able to study the airflow in hydroelectric generators, Hydro-Québec built a scale model, as described in Chapter 3. Although the scale model avoids the shutdown of real hydroelectric generators, it still has some impracticalities. For example, the complexity in making measurements on rotating machinery would slow down the design process. To resolve this, a static model was built.
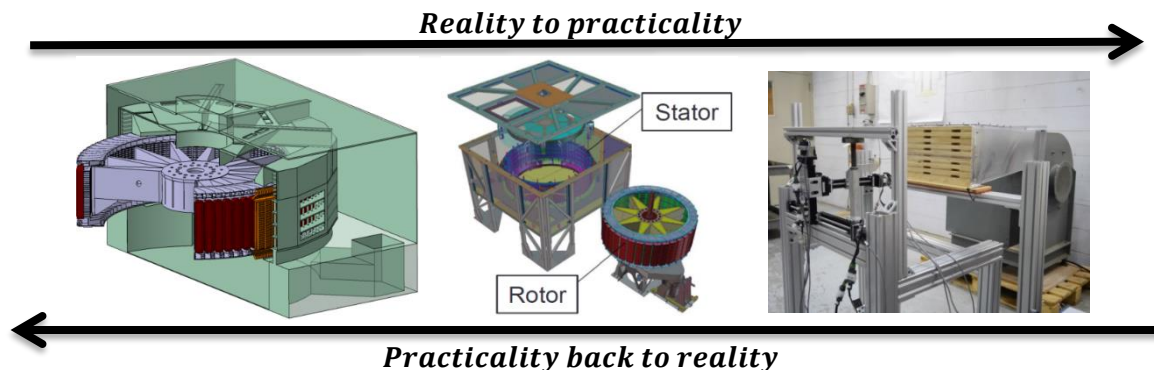
Figure 6-1: Experimental methodology

The static model is comprised of a blower, a diverging HVAC duct, a wood insert, and motorized axes held by an aluminum frame, as shown in Fig. 6-2.

Figure 6-2: (a): Front view of the static model ducts,
(b): View of the static model showing the blower (i), HVAC duct (ii), static model ducts
(iii), and the motorized axes (iv)

The wood insert replicates a section (24 ducts of 12.2 mm by 51 mm) of the scale model's rotor rim. As the name implies, this model is a stationary system so that the complexities associated with rotating machinery (i.e. data collection, large g-forces, high temperatures, and stringent safety measures) are avoided. These factors, although important, can be independently accounted for and excluded from the anemometer's performance testing. Thus, the static model will not validate the anemometer's ability to survive the harsh environments found in rotating machinery, but it will validate the anemometer's performance in obtaining average flow quantities, and its ability to meet the geometric constraints. Once the validation on the static model is complete, the anemometer can be tested in the hydroelectric generator scale model. If the tests are satisfactory, one can then implement the sensor in a real hydroelectric generator during a regularly-scheduled shutdown for maintenance.

6.2 Procedures for the experimental validation

Once an anemometer design is chosen, it must be validated and calibrated. To do so, the flow exiting the static model ducts was characterized by both the anemometer and another reference method. The latter method employed a combination of a hot-wire probe and a small (30 AWG) type-T thermocouple, as shown in Fig. 6-3.

Figure 6-3: Hot-wire/thermocouple combination used for simultaneous multi-point measurements

To effectively characterize the flow in the static model ducts, this technique was employed to collect data at specific locations arranged in a mesh to obtain the velocity and temperature profiles at the same time at the duct outlet. However, for practical implications the array of points was limited by a minimum distance between the thermocouple and hot-wire (5 mm), as shown in Fig. 6-3. The experimental validation included the following procedures:

      i.   Validation procedure

     ii.   Procedure for obtaining the temperature profile

    iii.   Procedure for obtaining the velocity profile

    iv.   Mesh discretization

Each describes how: i) the anemometer was validated, ii) the thermocouples used were calibrated to obtain the temperature profile, iii) the velocity profile was obtained using hot-wire anemometry and iv) the appropriate mesh for the application was chosen.

6.2.1 Validation procedure

The first step in validating the anemometer's performance is to define the appropriate temperature differential in Eq. 4.14. For heated flow in a duct, lacking a fixed free stream temperature, the appropriate temperature characterizing the thermofluid behavior is the bulk temperature (T_b). Since the flow entering the duct is at a uniform

temperature (T_i), one can define the appropriate temperature difference for Eq. 4.14 as the bulk temperature difference:

$$\Delta T_b = (T_b - T_i) = \frac{\int_0^w \int_0^h \rho(x,y)U(x,y)c_p(x,y)\Delta T(x,y)dxdy}{\iint \rho(x,y)U(x,y)c_p(x,y)dxdy},$$

(6.1)

where the velocity $(U(x,y))$, specific heat at constant pressure $(c_p(x,y))$, density $(\rho(x,y))$ and temperature difference $(\Delta T(x,y))$ defined as:

$$\Delta T(x,y) = T_o(x,y) - T_i,$$

(6.2)

are all functions of the vertical (y) and horizontal (x) position at the duct outlet with width w and height h. As specified in Eq. 6.1, obtaining this characteristic temperature difference requires detailed information of the velocity and temperature profile, and designing a thermal mass flow meter that could measure it was the most challenging aspect. Once obtained, one may calculate the mass flow rate as:

$$\dot{m}_{sensor} = \frac{\mathcal{P}_{inj}}{c_p(T_b) * \Delta T_b},$$

(6.3)

where $\mathcal{P}_{inj}$ is the energy injected into the flow by the heating element, and $c_p(T_b)$ the specific heat at constant pressure is evaluated at the bulk temperature. As a measure for comparison, the mass flow rate using hot-wire anemometry can be obtained by:

$$\dot{m}_{hot-wire} = \int_o^w \int_0^h \rho(x,y)U(x,y)dxdy.$$

(6.4)

Thus, the sensor's performance can be quantified by calculating the percent error between the calculated mass flow rate and the value obtained by hot-wire anemometry as:

$$\% Er = \frac{\dot{m}_{sensor} - \dot{m}_{hot-wire}}{\dot{m}_{hot-wire}}.$$

(6.5)

Some aspects that will affect the sensor's performance are energy losses (i.e. conduction and radiation losses) and the accuracy of the air temperature measurement, particularly at the duct outlet. The validation procedure requires that, one specify a method of obtaining both the velocity and temperature profiles at the duct outlet.

6.2.2   Procedure for obtaining the temperature profile

To obtain the temperature profile at the duct outlet ($T_0(x,y)$) and the uniform inlet temperature (T_i), two 30 AWG (~0.25 mm (0.01 in) in diameter) type-T thermocouple were used. These thermocouples where calibrated using a JOFRA Professional Temperature Calibrator V660. The JOFRA uses internal reference sensors with an accuracy of 0.15°C (0.27°F). Using this system, the digital output of the inlet and outlet thermocouples obtained from the National Instruments PXI Thermocouple card was corrected according to the JOFRA reading, as shown in Table 6-1.

Table 6-1: Thermocouple calibration

Ref.	Type T - thermocouples	
T_{JOFRA} [°C]	Inlet [°C]	Outlet [°C]
25	25.6	25.6
30	30.6	30.5
35	35.5	35.4
40	40.5	40.4
45	45.5	45.3
50	50.5	50.3
55	55.5	55.3
60	60.5	60.3
m	1.00	0.99
b	0.65	0.74
R^2	1.00	1.00

In Table 6-1, the inlet and outlet thermocouples are used to measure the inlet and outlet duct temperatures respectively. As illustrated from the data shown, the two thermocouples exhibited a linear behavior and only a small offset was applied and corrected by:

$$T_{Thermocouple} = m \cdot T_{JOFRA} + b,$$ (6.6)

where b represents the offset, m the slope and the R^2 represents the linear regression coefficient.

Once the method for obtaining the temperature profile is established, one can obtain the velocity profile using hot-wire anemometry.

6.2.3 Procedure for obtaining the velocity profile

The hot-wire used was a Dantec Dynamics 55P01 straight general-purpose probe (shown in Figs. 6-3 and 6-4). The signal conditioning system used for this hot-wire was a Dantec MINI CTA 54N80.
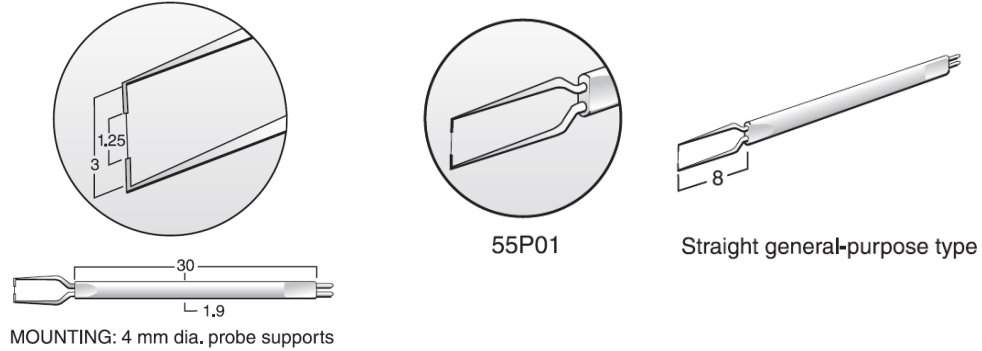
Figure 6-4: Dantec Dynamics hot-wire probe [32]

To relate the anemometer's response to the flow velocity, the modified version of King's law (Eq. 4.12) was used. This calibration equation has a nonlinear relationship between the anemometer response (E) and the flow velocity (U). To determine the calibration constants $(\mathcal{A}, \mathcal{B},$ and $n)$, one must collect the anemometer's response to a well calibrated reference velocity and apply a least-squares fit to the E^2 vs. U data. However, these constants are only valid for the free stream temperature specified in the calibration. This aspect must be considered as the heating element does not uniformly heat the flow, and creates large temperature gradients across the duct. One can compensate for measurements in non-isothermal flows using a correction to King's law proposed by Lienhard in 1988 [33]. This correction involves modifying the calibration constants $(\mathcal{A}, \mathcal{B}$ and $n)$ in Eq. 4.12 based on a combination of first principles and empirical effects between the temperature and the fluid properties and replacing them with:

$$\mathcal{A}_L(T(x,y)) = \mathcal{A}'\left(\frac{T(x,y) + T_w}{2}\right)^{0.84}\left(T_w - T(x,y)\right), \qquad (6.7)$$

$$\mathcal{B}_L(T(x,y)) = \mathcal{B}'\left(T_w - T(x,y)\right), \qquad (6.8)$$

and

$$\bar{n} = \left(\sum_{j=1}^{N} n(T_j) \right) \Big/ N,$$

(6.9)

where T is the free stream temperature at duct outlet which varies with position (x, y), $j = 1,2, \dots N$ is the number of free stream temperatures used in the calibration, and $\mathcal{A}', \mathcal{B}', T_w,$ are the new calibration constants resulting in the following calibration equation:

$$E^2(T(x,y)) = \mathcal{A}_L(T(x,y)) + \mathcal{B}_L(T(x,y))U^{\bar{n}}(T(x,y))$$

(6.10)

For this reason, the hot-wire anemometer was calibrated at six different temperatures, within a range of 20°C, as specified in the analytical validation phase, and within the velocity range observed in the CFD simulations of the rotor rim ducts (as shown in Fig. 6-5).
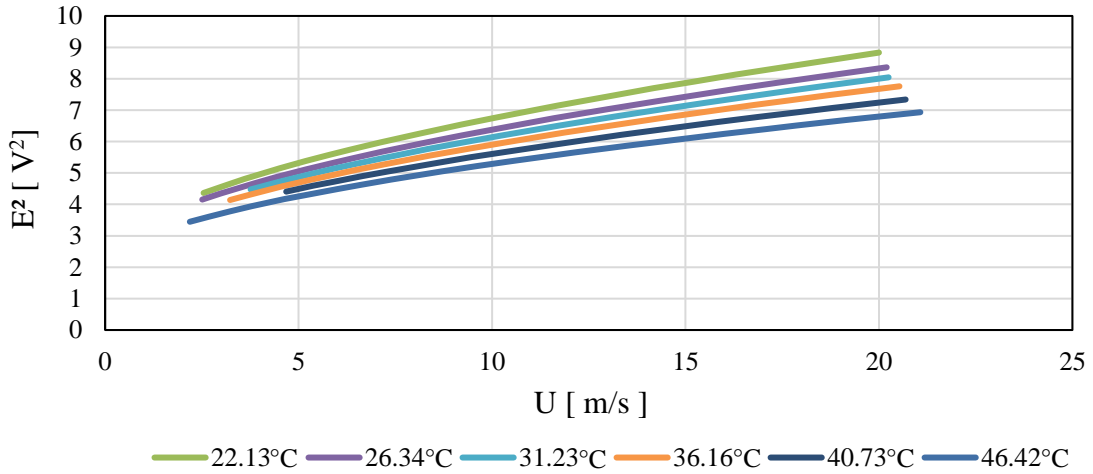
Figure 6-5: Hot-wire calibration curves at six different temperatures

All curves were obtained at a constant free stream temperature, except for the case at 46°C, where a 1.2°C deviation was observed due to limitations in the calibration equipment. Using this data, one can determine the new calibration constants ($\mathcal{A}'$, $\mathcal{B}'$, T_w) by: i) applying a least squares fit of Eq. 4.12 to the E^2 vs. U data at each free stream temperature to obtain $\bar{n}$, ii) applying the same fit, but replacing n with $\bar{n}$ and only varying constants $\mathcal{A}$ and $\mathcal{B}$ with the free stream temperature to obtain $\mathcal{A}_{\bar{n}}$ and $\mathcal{B}_{\bar{n}}$, then iii) applying a least

squares fit of Eq. 6.7 to the $\mathcal{A}_{\bar{n}}$ vs. T data, and Eq. 6.8 to the $\mathcal{B}_{\bar{n}}$ vs. T data, as shown in Figs. 6-7a and 6-7b.
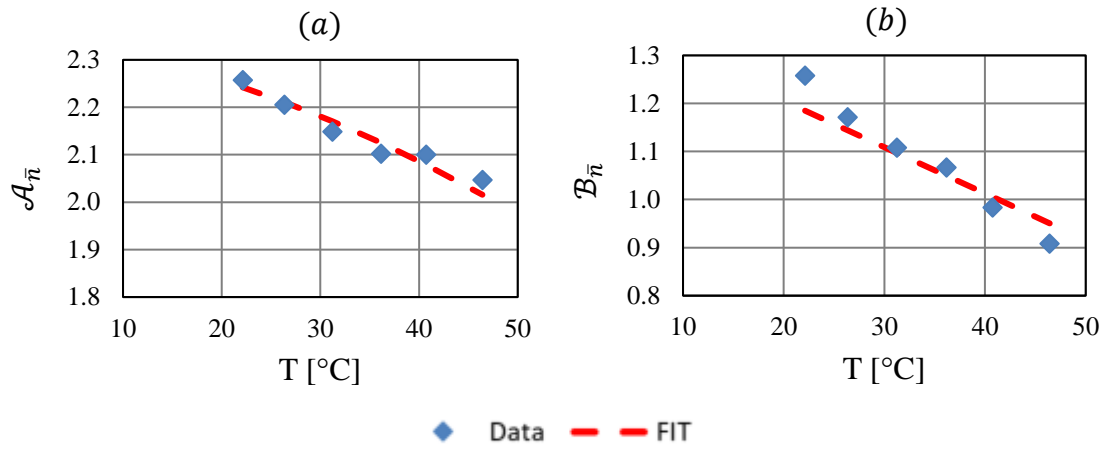
Figure 6-6: (a): Curve fit for the new $\mathcal{A}_{\bar{n}}$ vs. T for Lienhard's method, (b): Curve fit for the new $\mathcal{B}_{\bar{n}}$ vs. T for Lienhard's method

Using these constants, one can estimate the flow velocity at any location (x, y) and temperature at the duct outlet by solving for the velocity in Eq. 6.10 as:

$$U(T(x,y)) = \left(\frac{E^2(T(x,y)) - \mathcal{A}_L(T(x,y))}{\mathcal{B}_L(T(x,y))} \right)^{1/\bar{n}}. \tag{6.11}$$

Once methods for obtaining both the temperature and velocity profiles are established, one may specify the mesh discretization required to obtain the bulk temperature difference and the mass flow rate.

6.2.4 Mesh discretization

To obtain the velocity and temperature profiles at the duct exit, one must determine the required mapping of points. An optimal mesh achieves a reasonable compromise between the time required to perform the measurement for the set of points, and the error generated from the integration process (e.g. computing the mass flow rate).

A first estimate of the mass flow rate was obtained by performing a hot-wire scan at the duct outlet by collecting data at 15 axial positions. At each axial position, the hot-wire moved horizontally across the duct at a constant speed of 1 mm/s and at an acquisition rate of 1kHz. Then through post-processing, the velocity was integrated to obtain the mass

flow rate in the duct. However, it was observed that with this method, the results were not sufficiently repeatable since the hot-wire only collects data at one location during a fraction of a second. Therefore, one must perform a convergence test to determine the data acquisition time that will correctly represent the time averaged values of the flow.

The convergence test showed that an acquisition period of one minute per point was sufficient to limit the variation in the time averaged velocity across the duct within 1%. When the flow in the duct is heated, a 30 second idle period between each point is taken to account for the thermocouple's thermal inertia, making the total acquisition time per point 90 seconds.

Once the data acquisition time per point is determined, one must obtain the mapping of points that will yield a minimum integration error on the mass flow rate. Although, the post-processed value obtained from the hot-wire scan was inaccurate, one can use this data to select an initial mapping of points. Thus, 6, 8, 10, and 14 points uniformly spaced along each of the 15 lines were taken, and their respective integration error on the mass flow rate was determined. Then for each case, one can plot their respective integration error and acquisition time to determine a viable mesh discretization as shown in Fig. 6-7.
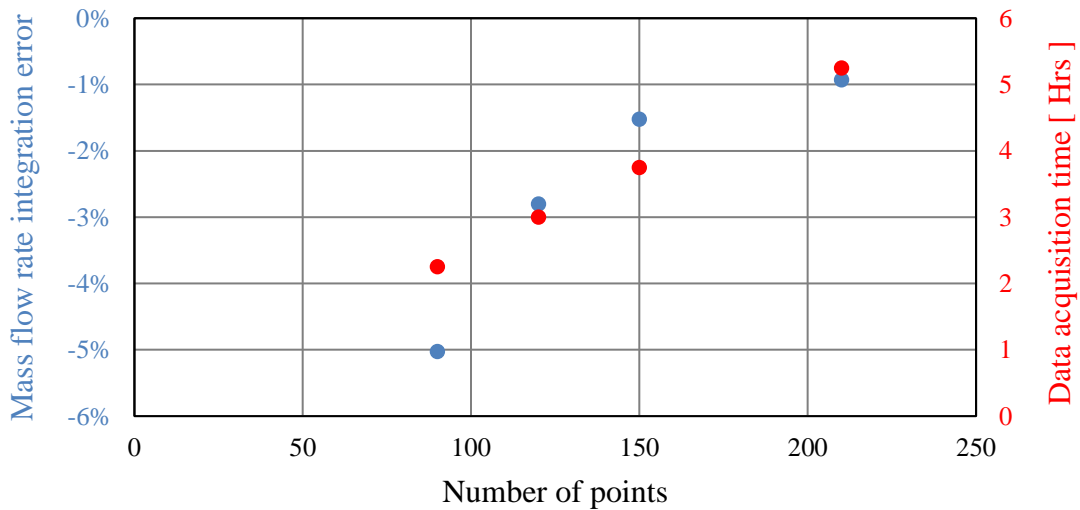
Figure 6-7: Integration error on the mass flow rate and acquisition time per mesh discretization

From these results, it was concluded that 15 lines of 10 points each, uniformly distributed, yielding an integration error of 1.5% and an acquisition time of 3.75 hours was satisfactory.

6.3 Experimental setup

The experimental setup used to validate the sensor is shown in Fig. 6-8.
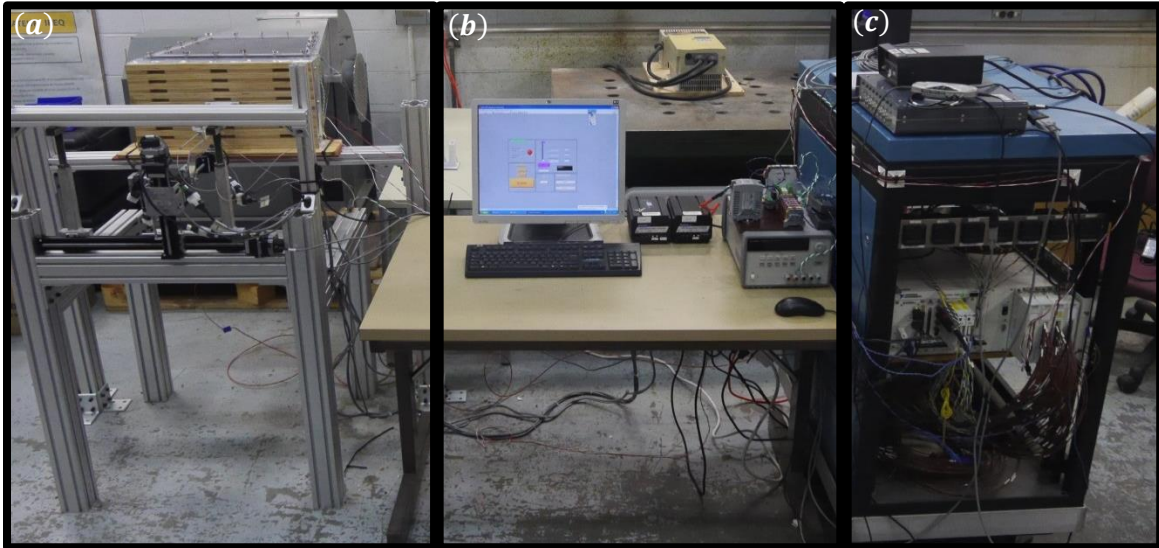
Figure 6-8: Experimental setup comprising of the static model (a), the control system (b), and the acquisition system (c)

The experimental setup is comprised of three main parts: i) the static model, ii) the controlling system, and iii) the acquisition system.

All the components of the static model were described in section 6.1, with exception of the motorized axes that allow the hot-wire/thermocouple to move along three axes to cover the exit of the duct. The motors used are Velmex Motorized Screw Drive XSlides with a three-axis system. These are worm screw motors with an inline accuracy of 0.762 mm (0.03 in). The static model and the motor system are supported by an aluminum frame made from T-Slotted Aluminum Extrusions by Faztek.

The control system is comprised of five components: i) the computer, ii) the stepper motor controllers, iii) the DC power supply, iv) the blower controller, and v) the safety system. The computer communicates with the controllers and acquisition system using LabVIEW 8.6. The stepper motor controllers are Velmex VXM controllers, which operate at a maximum of 400 steps per revolution. The 200 W DC power supply (Agilent E3634A) controls the amount of energy injected into the heating element of the anemometer. The voltage and current from the DC power supply are indicated on an LCD screen having a resolution of 1 mV and 1 mA (<10 A) – 10 mA (≥10 A). The blower controller is a Delta 7.5 hp three phase, 575 V AC drive. The AC drive controls the blower fan frequency from

0-400 Hz with a 0.01 Hz frequency resolution. The safety system is comprised of relays and a FLUKE 80i-110s AC/DC Current Probe, capable of measuring the current passing through wires with a maximum measurement error of 3% (in a 50 mA - 10 A range). The purpose of the safety system is to collect data using the hot-wire/thermocouple method at the outlet of duct equipped with a thermal mass flow meter autonomously. The main danger is if the heating element of the thermal mass flow meter overheats. This can be prevented by monitoring the current injected into the heating element using the current probe and having both software and hardware safety devices (e.g. relays to cut the current should it exceed the specified amount).

The last part of the experimental setup is the acquisition system. The acquisition system is comprised of motor encoders, a thermocouple/RTD output acquisition system, and a hot-wire voltage/output acquisition system. The motor acquisition is done with the combination of an encoder and a data acquisition system (DAQ). The encoder is a Hewlett Packard (HP) HEDS 550 rotary encoder, which translates the rotatory motion of the screw drive into a digital output. This encoder has an accuracy of ±0.25 mm (±0.010 in). This digital output is then read by a National Instruments X Multifunction DAQ. The thermocouple/RTD and hot-wire acquisition is part of an integrated signal conditioning system. This system is a National Instruments PXI Chassis with integrated signal conditioning. A National Instruments PXI-4070 was used to collect the output voltage from the hot-wire signal conditioning system.

6.4   Prototype design of a thermal mass flow meter

The analytical validation showed that the most viable technique to characterize the flow in the rotor rim ducts of a hydroelectric generator was the thermal mass flow meter. Therefore, this technique was selected for the prototype design phase. The main objectives for the prototypes were to: i) meet the geometric constraints of the rotor rim duct and, ii) have a heating element that can heat the flow.

The details of the prototype design phase are the proprietary right of Hydro-Québec. Thus, only general features can be disclosed in this thesis. However, it is important to note that most of the work underlining this thesis was spent on the design details of this anemometer. The main designs are the 4th and 5th iterations. The 4th iteration focused on

determining the method to measure the bulk temperature at the duct outlet, and the 5th iteration implemented the method to perform such a measurement.

6.4.1   4th iteration thermal mass flow meter design

The goal of the 4th iteration was to have a working heating element that would fit inside the specified geometry of the static model duct.
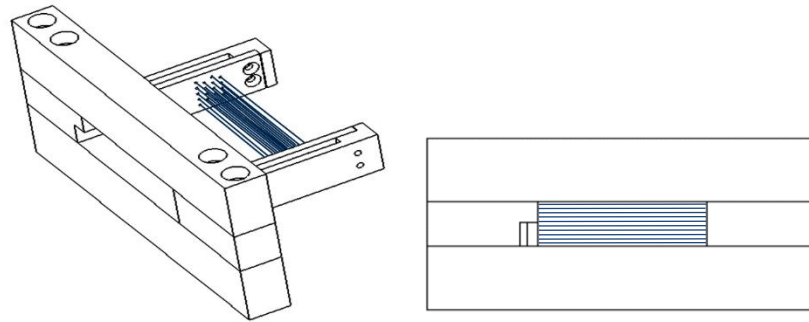
Figure 6-9: 4th iteration of the thermal mass flow meter

This anemometer featured an aluminum frame with nichrome wires as the heating element, shown in dark blue in Fig. 6-9. The nichrome wires are in a staggered arrangement forming a bank of 30 wires that are powered by a 0-5 A, 48 V system. The developed sensor has an operating range capable of emitting 20 to 170 W into the flow, which is rated to measure flows with an average duct velocity between 1.4 and 12 m/s.

6.4.2   5th iteration thermal mass flow meter design

The knowledge gained from the 4th iteration design prompted the design of an RTD to properly capture bulk temperature at the duct outlet. This RTD design considered: i) the resistance-temperature variation, ii) the overall RTD resistance, its fragility, and iii) the effect of self-heating. Once built, the RTD wires were calibrated.

Typically, RTDs are made from metal wires that exhibit an increase in electrical resistance with temperature. Thus, a more practical relation between the resistance of the RTD and temperature is a polynomial expression of the following form:

$$R(T) = R_0[1 + a(T - T_0) + b(T - T_0)^2 + \cdots],$$
(6.12)

where the calibration constants a and b are dependent on the material used, and the subscripts refer to the temperature at which these variables were obtained. For example, R_0 is the resistance of the RTD at T_0 (0°C). Eq. 6.11 is a higher order nonlinear equation typically used over large temperature ranges. In practice, one obtains a higher accuracy in the temperature measurement when a material exhibits a linear change in resistance with temperature, and most metals exhibit this behavior over a short temperature range. Thus, for materials that exhibit a linear change in resistance with temperature or for a short temperature range, the following first-order approximation is adopted:

$$R(T) = R_0[1 + C_\alpha(T - T_0)], \qquad (6.13)$$

where C_α is the temperature coefficient of resistance, which is defined by the following equation:

$$C_\alpha = \frac{R_{100} - R_0}{(100°C) \cdot R_0}. \qquad (6.14)$$

Materials that have been considered for use in the RTDs are nickel, copper, platinum, balco (rare), or tungsten (rare), as shown in Fig. 6-10.
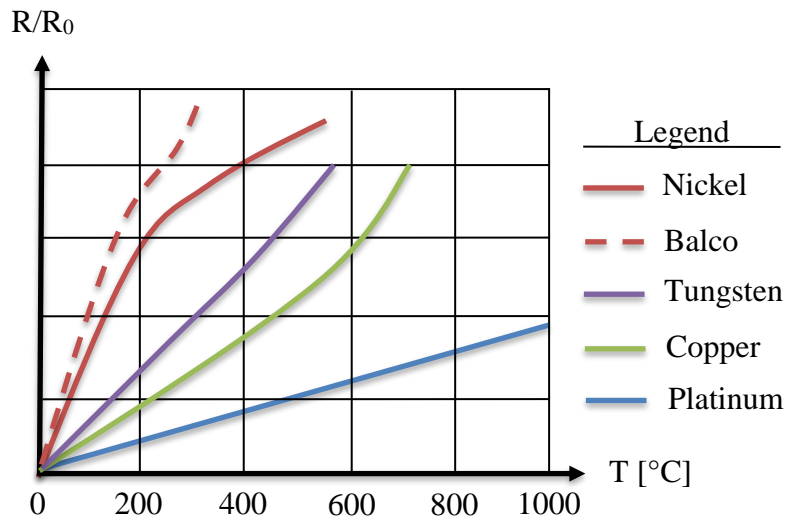
Figure 6-10: Schematic of the normalized resistance-temperature behavior for common RTD materials

Table 6-2 shows the electrical resistivity (χ), the temperature coefficient of resistance (C_α), and the yield stress (σ_y) for the materials given in Fig. 6-10.

Table 6-2: Considered RTD material properties from MatWeb

Material	$\chi\,[\mu\Omega \cdot cm]$	$C_\alpha\,[\,\Omega\,/\,(\Omega \cdot ℃)\,]$	$\sigma_y\,[\,MPa\,]$
Nickel	6.4	0.0068	59
Balco: Nickel Alloy 120 (70% Ni 30% Fe)	19.9	0.045	483
Tungsten	5.65	0.0048	750
Copper	1.69	0.0043	333
Platinum	10.58	0.0039	185

Platinum is the ideal material of choice for an RTD as it varies linearly with temperature for temperatures above 650℃, whereas other materials begin to exhibit a nonlinear behavior at approximately 200℃. However, platinum is not the best choice of material for measuring the temperature at the duct outlet, as the right combination of electrical resistivity, temperature coefficient of resistance, and yield stress is required, and for platinum the latter two are too low.

The first criterion, the temperature coefficient of resistance is the slope of the lines shown in Fig. 6-10, and thus, the larger the slope, the greater the resistance change per unit temperature the RTD wires will experience. Furthermore, if the resistance change per unit temperature is small, it will require a system capable of resolving low voltage readings with high accuracy. The validation phase for the thermal mass flow meter set the operating temperature range between 20-45℃, thus within this range one can observe from Fig. 6-10 that: i) all the materials exhibit a linear behavior, and ii) Balco, a nickel alloy composed of 30% iron and 70% nickel experiences the highest resistance change per unit temperature.

The second criterion, the yield stress directly impacts the manufacturability of the RTDs. For the manufacturing process to be successful, the wire cannot yield under the applied force, thus one can define a maximum force F_{max} as:

$$F_{max} = \frac{\sigma_y}{A_c}. \tag{6.15}$$

where the maximum force the wire can withstand is related to the yield stress of the material (σ_y) and the wires cross-sectional area (A_c). Consequently, both the resistance variation

(Eq. 6.13) and strength (Eq. 6.15) of the material vary with wire diameter, as shown in Fig. 6-11.
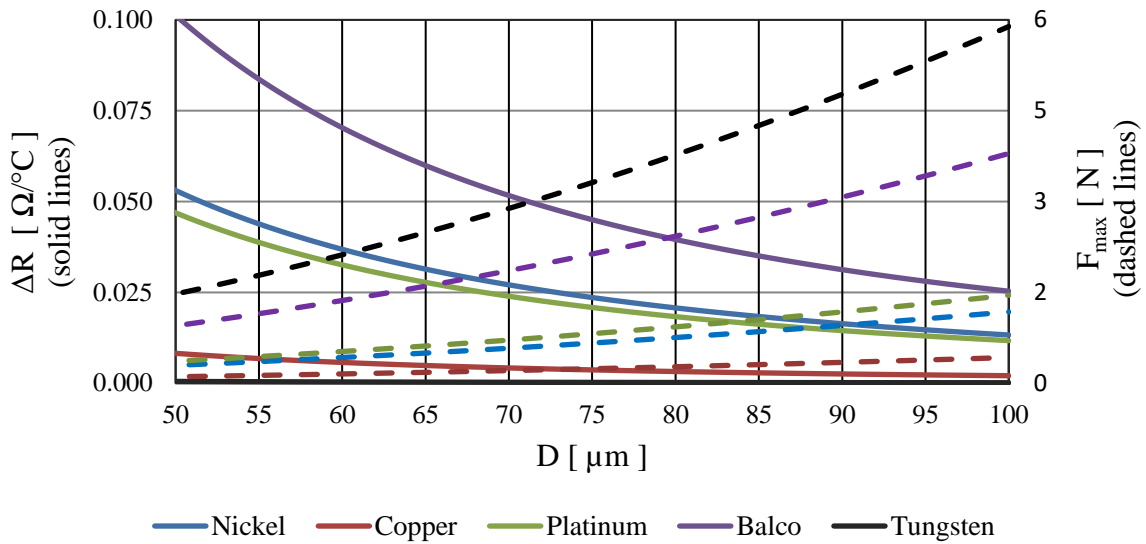
Figure 6-11: The temperature-resistance variation per unit temperature and the maximum force an RTD wire can experience as a function of wire diameter and material

In Fig. 6-11, a linear change of resistance with temperature was assumed and the material properties for the five metals were obtained from Table 6.2. The wire diameter range was specified from 50 to 100 µm, as values outside this range are not practical in a manufacturing sense. Therefore, one can observe that smaller wire diameters have a greater increase in resistance with temperature, whereas larger wire diameters can resist a larger force, and the optimal condition is a Balco wire with a diameter of 80µm. However, prior experimentation with the manufacturing process showed that an applied force of 0.95 N is indeed viable, and that an RTD with a wire diameter of 50 µm and a 100mΩ/°C resistance-temperature variation is more important.

The last criterion, the electrical resistivity controls the overall resistance of the RTD. It is important to choose a material that will have the highest overall resistance as it improves the signal-to-noise ratio. Furthermore, the higher the resistance, the more stable the voltage will be across the wire when attempting to make a resistance measurement by injecting a small (1 mA) current. Fig. 6-12 shows the effect of the wire diameter and material on the overall resistance.
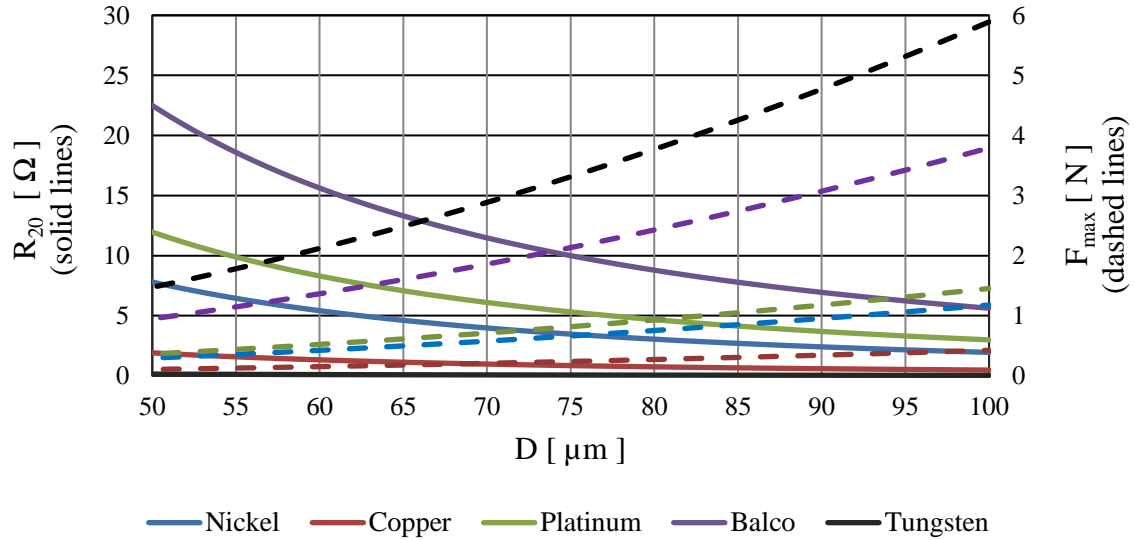
Figure 6-12: The net resistance and the maximum force an RTD wire can experience as a function of wire diameter and material

From the Fig. 6-12, one can observe that the smallest wire diameter gives the highest resistance. Thus, the most practical set of parameters for the RTD wire are: i) a 50 µm diameter, ii) made of Balco, iii) with a 100 mΩ/°C resistance-temperature variation, and iv) an overall resistance of 22.50 Ω.

The last aspect to consider when designing an RTD is the effect of self-heating. The operating principle of an RTD relies on the fact that resistance varies with temperature. However, heat is generated in an RTD by the current that passes through it, which can lead to a systematic error. The heat transfer rate per unit temperature difference from the RTD to the surrounding medium is defined as the dissipation constant ($\mathcal{D}$), which is the product of the convective heat transfer coefficient (h) and the surface area (A_S) of the RTD [34]. Thus, one can define the temperature increase (ΔT) due to self-heating of the RTD as:

$$\Delta T = \frac{I^2 R(T)}{\mathcal{D}} = \frac{I^2 R(T)}{h * A_S}. \qquad (6.15)$$

Obtaining a first estimate for the dissipation requires a relation for the convective heat transfer coefficient. With respect to the current application, one can model the RTD wires as cylinders in cross flow. Therefore, the modified empirical relation of Hilpert [31] can be used to obtain the convective heat transfer coefficient:

$$h = \frac{Nu_D \cdot k}{D} = (k/D)CRe_D^m Pr^{1/3}, \qquad (6.16)$$

where k is the thermal conductivity of air, D is the diameter of the wire and the constants C and m are determined from Table 6-3.

Table 6-3: Coefficients for Hilbert's convective heat transfer correlation (Eq. 6.16) [31]

Re_D	C	m
$0.4 - 4$	0.989	0.330
$4 - 40$	0.911	0.385
$40 - 4 * 10^3$	0.683	0.466
$4 * 10^3 - 4 * 10^4$	0.193	0.618
$4 * 10^4 - 4 * 10^5$	0.027	0.805

Solving for the temperature rise, and assuming a first order approximation for the resistance-temperature relation, one obtains the following relation:

$$\Delta T = \frac{4I^2 \chi_{20}}{k(\pi D)^2 CRe_D^m Pr^{1/3} - 4I^2 \chi_{20} C_\alpha}, \qquad (6.17)$$

Therefore, one must increase the heat transfer rate to the surrounding medium or lower the amount of current used to measure the resistance. Considering the present application, the only parameter left to vary is the current used. Using the typical current value of 1mA, one obtains the temperature rises indicated in Table 6-4 for the specified operating range.

Table 6-4: RTD self-heating values for the specified velocity range

$U\,[m/s]$	1.44	3.57	12.15
$\Delta T\,[°C]$	0.0059	0.0039	0.0022

Based on the results outlined in Table 6-4, it was deemed that in the operating range, no significant self-heating error was induced.

The 5th iteration design of a thermal mass flow meter was required to validate: i) the method for obtaining the bulk temperature at the duct outlet established by the 4th iteration design and ii) the designed RTDs ability to measure the bulk temperature. This new design featured a modified aluminum frame that could accommodate the inlet and outlet RTD wires (shown in blue) while keeping same Nichrome wires as the heating element (shown in red), as shown in Fig. 6-13.
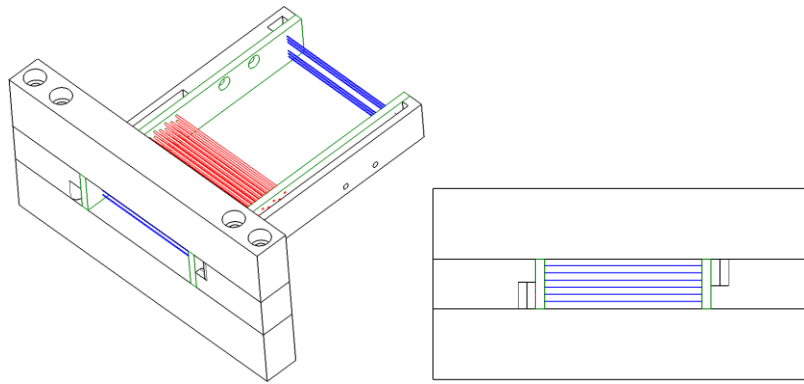
Figure 6-13: 5th iteration design of a thermal mass flow meter

Once manufactured, the RTD wires must be calibrated to obtain an accurate temperature reading.

The RTD calibration procedure involved placing the anemometer in a beaker filled with oil to provide a more uniform temperature medium than air, then the beaker was placed inside an industrial oven to vary the oil temperature, which was verified by a standard OMEGA PT100 reference RTD. The temperature in the beaker was assumed stable if the reference RTD had a variation smaller than 10 mΩ in ten minutes, since the RTD design has a 100 mΩ/°C resistance-temperature variation, this implied a 0.1°C temperature change in the designed RTDs over that time. This calibration was done at five different temperatures over the desired range as shown in Fig. 6-14.
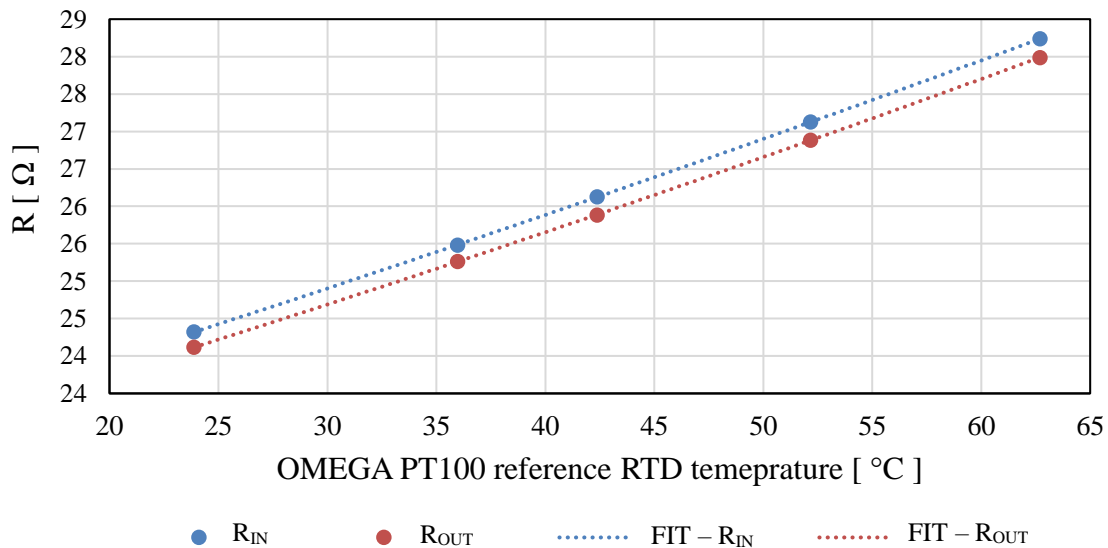
Figure 6-14: Calibration curves for the inlet and outlet RTDs shown in blue in Fig. 6-13

Although the calibration curves are practically linear, a better fit was obtained using a second order polynomial of the following form:

$$R_{RTD} = a \cdot T_{RTD}^2 + b \cdot T_{RTD} + c, \qquad (6.18)$$

where the polynomial coefficients are given in Table 6-5 for the inlet and outlet RTDs.

Table 6-5: RTD calibration coefficients (from Fig. 6-14)

RTD	a	b	c
Inlet	$1.67 \cdot 10^{-4}$	$8.65 \cdot 10^{-2}$	$2.22 \cdot 10^{1}$
Outlet	$1.92 \cdot 10^{-4}$	$8.31 \cdot 10^{-2}$	$2.20 \cdot 10^{1}$

Thus, once a resistance measurement is made, one must use the following equation to solve for T_{RTD}:

$$T_{RTD} = \frac{-b + \sqrt{b^2 - (4a \cdot (c - R_{RTD}))}}{2a}. \qquad (6.19)$$

As designed, the RTD wires have a 100 mΩ/°C resistance-temperature variation but, a more standard wire diameter of 44 AWG (51 µm) with an overall resistance of about 24 Ω at 20°C was obtained. Since the flow entering the rotor rim ducts is at a uniform temperature, the inlet RTD wires are uniformly spaced, whereas the outlet RTDs are in a unique arrangement that was determined from experiments performed on the 4th iteration design. These results and the explanation for the wire arrangement are presented in the next chapter.

Chapter 7
Results/Discussion

The final phase of the project is the proof of concept of the thermal mass flow meter. This was accomplished on the static model so that one could quantify the sensor's capability of measuring the mass flow rate in a small duct under various flow configurations. The results on the static model are divided into two sections: i) results for the 4th iteration design and ii) results for the 5th iteration design. The experiments performed using the former design investigated the feasibility of obtaining the bulk temperature at the duct outlet via i) a single-point thermocouple measurement and ii) the designed RTD method. The experiments performed using the later design quantified the RTD technique's performance, robustness to varying flow conditions, and how the sensor itself alters the mass flow rate.

7.1   Results for the 4th iteration design

As described in the experimental validation (Chapter 6), the thermal mass flow meter's performance was validated by comparing the sensor's mass flow rate to the one obtained by the thermocouple/hot-wire apparatus shown in Fig. 7-1.
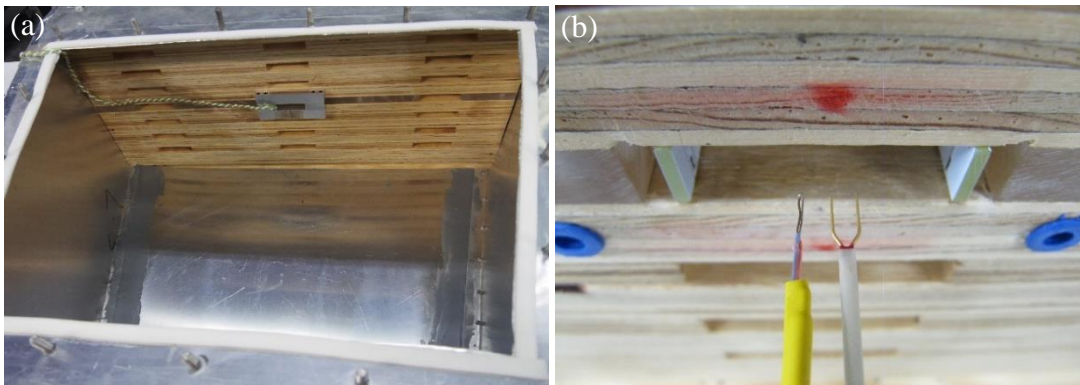
Figure 7-1: (a): 4th iteration thermal mass flow meter installed at the static model inlet

(b): thermocouple/hot-wire apparatus at the outlet of the static model

Fig. 7-1a depicts the 4th iteration thermal mass flow meter installed at the inlet of the static model and Fig. 7-1b shows thermocouple/hot-wire apparatus used to collect data at the duct's outlet. This setup allowed for the investigation of: i) the feasibility of using a single-point temperature measurement to obtain an estimate of the bulk temperature, ii) an alternative method using RTD wires to measure the bulk temperature, and iii) the RTD method's robustness to varying flow conditions that occur in hydroelectric generators.

7.1.1 Single-point temperature measurement

The static model permits several point measurements at the outlet of any duct to be made — a feat that would be impossible in a hydroelectric generator. To be reasonably implementable, a method must provide the bulk temperature in a single measurement and location. However, this type of measurement may introduce a significant error if performed in a flow of non-uniform temperature. A possible solution that will hopefully result in a fully-mixed uniform outlet temperature is to extend the length of the static model to the same aspect ratio as that of a real machine, by using Acrylonitrile butadiene styrene (ABS) extensions (as shown in Fig. 7-2).
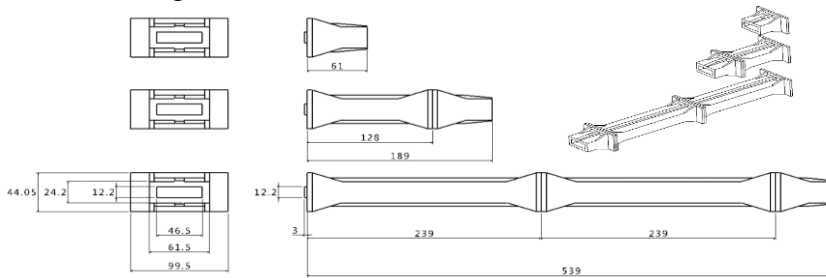
Figure 7-2: ABS extensions used at the outlet of the static model duct (units in mm)

Each configuration used the 61 mm extension at the downstream end to keep the outlet area constant. To ensure a proper insertion of the extension into the static model duct, the width of the extensions are slightly smaller (47 mm) than those of the actual duct (51 mm).

Measurements were made at the duct outlet for the four cases listed in Table 7-1, to quantify the effect duct length has on the temperature/velocity profile uniformity, bulk temperature difference, and midpoint temperature value.

Table 7-1: Configurations used in the feasibility analysis of a single-point measurement

Case	Extension [mm]	Total Duct Length [mm]
A	None	61
B	61	122
C	189	250
D	539	600

Measurements for case A are performed directly at the outlet of the static model duct and thus, no extension was used. The goal of this experiment was to determine if, at the outlet of an actual rotor rim duct, the temperature would be sufficiently uniform such that a single-point temperature measurement would provide the bulk temperature. The results of this experiment are shown Figs. 7-3 and 7-4.
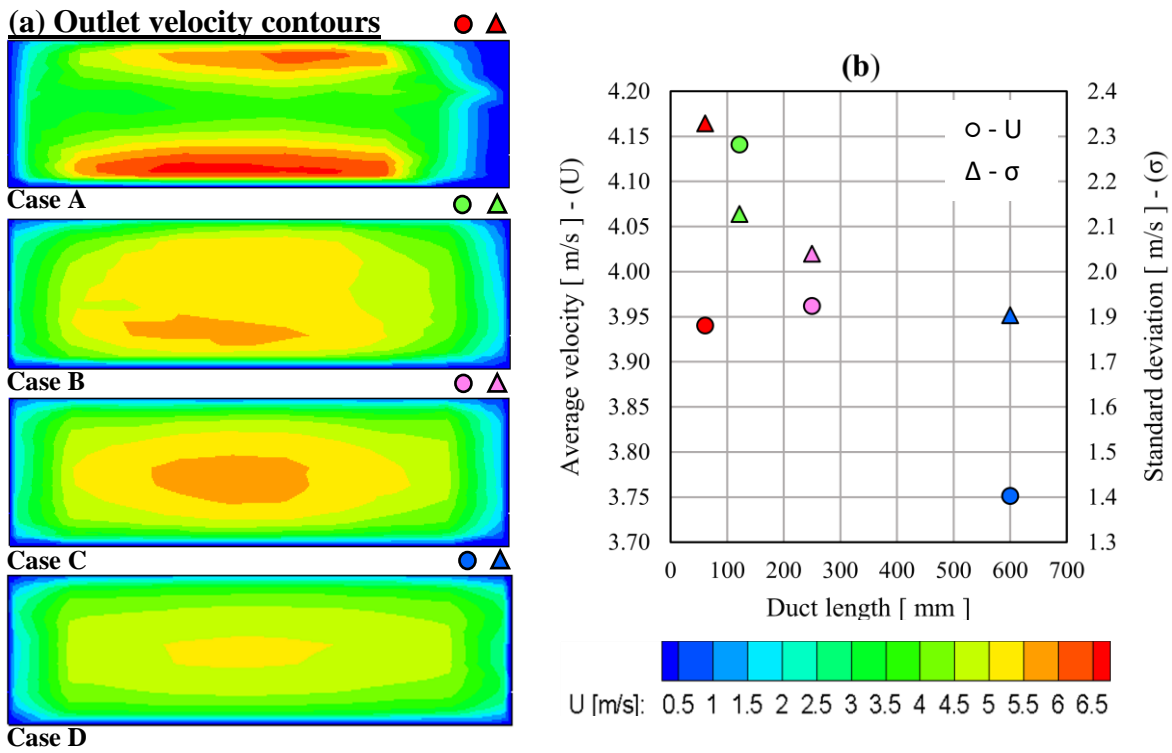
Figure 7-3: (a): Outlet velocity contours, (b): Average velocity at different duct lengths
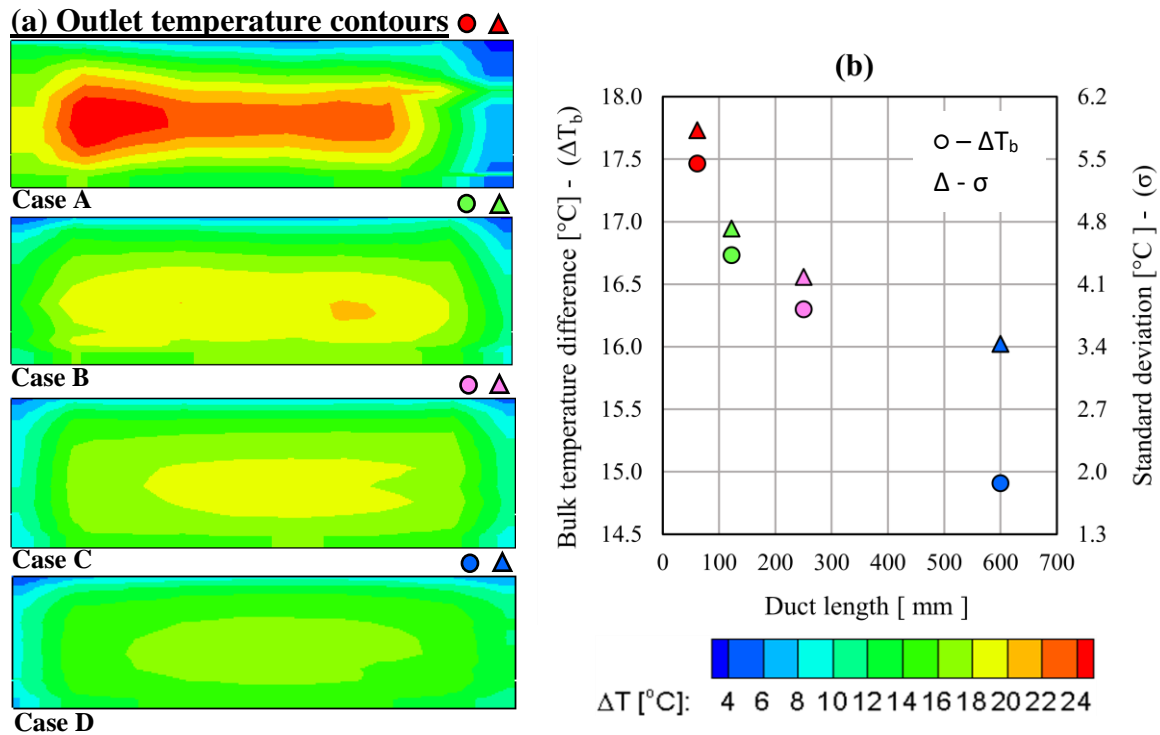
Figure 7-4: (a) Outlet temperature difference contours ($\Delta T(x, y) = T_0(x, y) - T_i$),

(b): Bulk temperature difference ($\Delta T_b = T_b - T_i$) at different duct lengths

Fig. 7-3a shows the velocity contours at each duct exit and Fig. 7-3b shows their corresponding average velocities. The results show that, as the duct length increases, the velocity contour becomes more uniform. This is also confirmed by considering the standard deviation in Fig. 7-3b: as the duct length increases, the standard deviation decreases. Also shown in Fig. 7-3b is the variation of the average velocity with duct length, this variation can be explained by considering the mass flow rate obtain by the hot-wire for each case, as shown in Fig. 7-5.
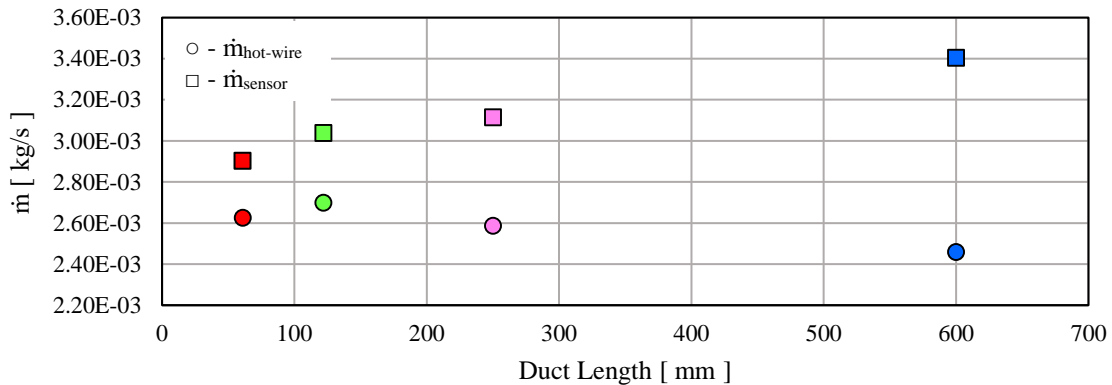
Figure 7-5: Mass flow rate at different duct lengths

Due to the conservation of mass, the mass flow rate for each case should be the same. However, this is not seen in both the values obtained by the hot-wire and the sensor. The former is due to an increase in head losses as one increases the duct length, whereas the latter is due to a conceptual flaw in the calculation of the mass flow rate using the simplified form of the principal of conservation of energy for a flowing fluid assuming no energy losses (Eq. 6.3). Moreover, as one makes a measurement further downstream this assumption becomes less valid because wall conduction losses increase. Thus, the apparent deviation of the conservation of mass for the sensor in Fig 7-4 is due to the deviation from a key assumption made in Eq. 6.3, which is further observed in Fig. 7-4.

Fig. 7-4 shows the temperature difference contours at each duct exit and their corresponding bulk temperature difference. For each case, 52 W was injected into the flow by the heating element. From the temperature contour, one observes that, as the duct length increases, the temperature contour becomes more uniform, as confirmed by the decrease

in standard deviation. Fig. 7-4b also indicates a decrease in bulk temperature as duct length increases, which due to the previously mentioned conduction losses through the walls.

As previously noted, the decrease in bulk temperature difference as the duct length increases is due to energy losses. These losses can be obtained by comparing the energy injected in the flow ($\mathcal{P}_{inj}$) to the one measured at the duct outlet using measurements made by the thermocouple/hot-wire combination ($\mathcal{P}_m$) as:

$$\% \ Energy \ Loss = \left(\frac{\mathcal{P}_{inj} - \mathcal{P}_m}{\mathcal{P}_{Inj}}\right) \cdot 100. \qquad (7.1)$$

Fig. 7-6 plots this quantity as a function of duct length to quantify the deviation from the assumption made in Eq. 6.3.
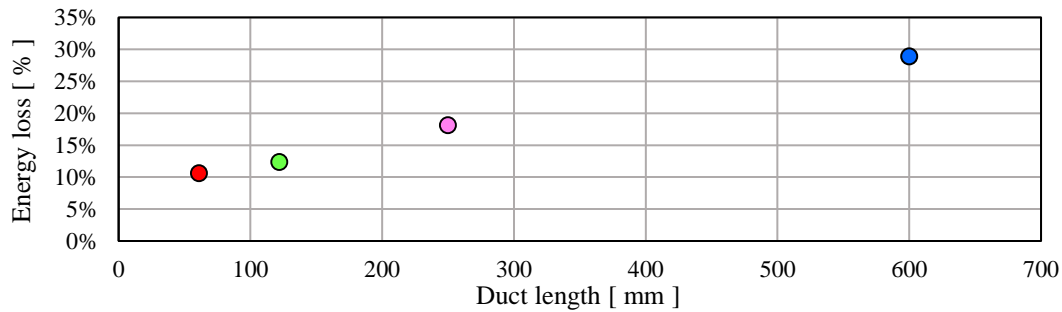
Figure 7-6: Energy losses in the duct

As shown in Fig. 7-6, as one increases the duct length (or measures the temperature farther downstream of the heating element) there is an increase in energy losses, due to heat conduction across the duct walls. In fact, even for materials with low thermal conductivity, such as wood and ABS, one can still observe losses of approximately 10% for a duct length of 61 mm and up to 30% for a duct length of 600 mm. The former distance represents the length of the rotating scale model rotor rim ducts. Therefore, one cannot expect to achieve accuracies greater than 10% with this technique. In summary, if the temperature probe is placed too close to the heating element, a single-point temperature measurement is not representative of the bulk temperature due to large temperature variations, and if the probe is too far from the heating element, the energy losses in the duct are too large to make accurate measurements. Therefore, a single-point temperature measurement is not an acceptable method to measure the bulk temperature and thus, an alternative approach must be used.

7.1.2 RTD measurement technique

The results shown in the previous section demonstrate the need to obtain the bulk temperature difference in a non-isothermal flow, such as the one at the outlet of a 61 mm static model duct, as shown in Fig. 7-7:
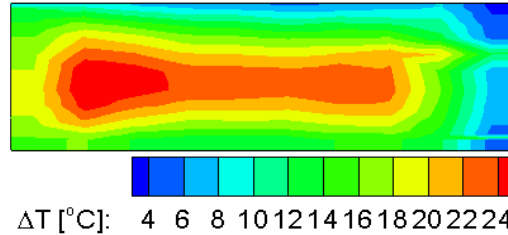
Figure 7-7: Temperature difference contour $(\Delta T(x, y) = T_0(x, y) - T_i)$ at outlet of the static model duct (61 mm)

For this flow the bulk temperature difference was 17.5°C with local temperature differences varying between 4°C and 24°C. Ultimately one must be able to make a temperature measurement that approaches the bulk temperature difference. Given the approximate symmetry of the flow, there may exist a location in which the local temperature is equal to the bulk temperature difference. This region can be identified by calculating the percentage difference between the inlet and outlet temperature difference and the bulk temperature difference:

$$\% \, Diff_{\Delta T_b} = \left(\frac{\Delta T - \Delta T_b}{\Delta T_b}\right) \cdot 100. \tag{7.2}$$

To see the region more clearly one can plot the contour of the percent difference in bulk temperature difference as shown in Fig 7-8:
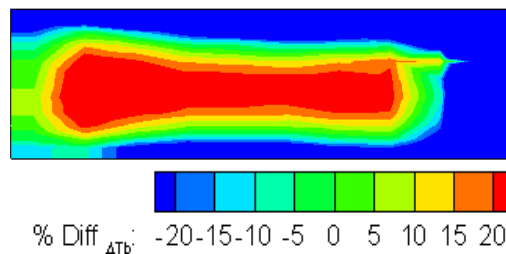
Figure 7-8: $\%Diff_{\Delta T_b}$ contour at the outlet of the static model duct (61 mm)

In Fig. 7-8, the green annulus is the region where the temperature difference is approximately equal to the bulk temperature difference. Ideally, one would only measure the temperature in this region. As described in Section 6.4.2, it was determined that the best way to capture this region was to use the RTDs specifically designed for this application. As shown in Fig. 7-9, the RTD featured 6 wires located 2, 3, and 4 mm above and below the center line of the duct.
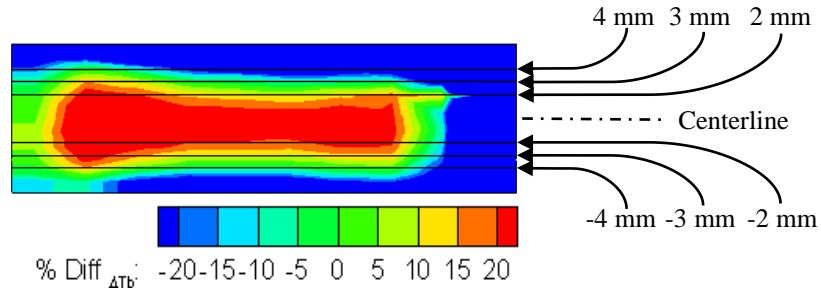
Figure 7-9: 6-wire RTD design

Through post-processing one can obtain the (theoretical) RTD temperature difference, ΔT_{RTD} by taking the arithmetic mean of the temperature across the lines shown in Fig 7-9:

$$\Delta T_{RTD} = 17.23°C. \hspace{3cm} (7.3)$$

This value can then be compared to the bulk temperature difference to evaluate the measurement error:

$$\%Er_{\Delta T} = \left(\frac{\Delta T_b - \Delta T_{RTD}}{\Delta T_b}\right) \cdot 100 \approx 1\%. \hspace{2cm} (7.4)$$

Thus, the post-processing results indicate that the 6-wire RTD could be an accurate method to estimate the flow bulk temperature.

Although the post-processing results of the 6-wire RTD technique provided the bulk temperature within a 1% error, the dependency of the average temperature measurement on the varying flow conditions that occur in hydroelectric generators (e.g. variations in velocity profile and inlet incidence angles) must be validated.

7.1.3 Robustness of the RTD technique

The 6-wire RTD technique's robustness to varying flow conditions that occur in hydroelectric generators was validated by varying inlet flow conditions (i.e. the incidence angle and speed). As described in Section 3.4, CFD simulations of the rotating scale model have shown that the flow entering the rotor rim ducts with large incidence angles (~45°) causes recirculation zones within the duct. However, initial tests on the static model were performed with purely radial flow. For this reason, an attempt was made to recreate the same flow conditions in the static model. To create an inlet flow incidence angle, a flow deflector was made to deflect the flow as shown in Fig. 7-10.
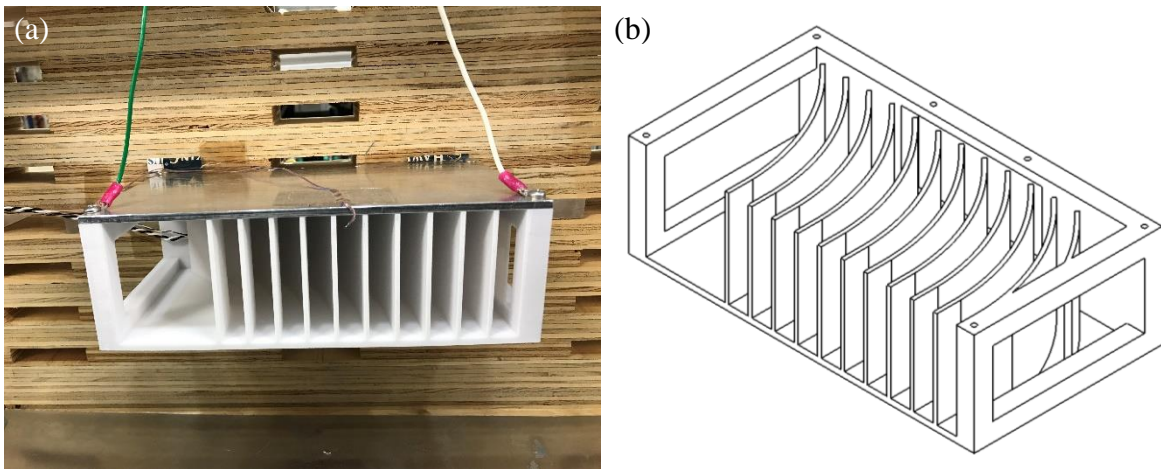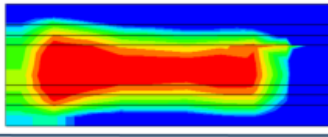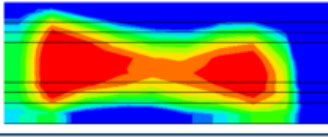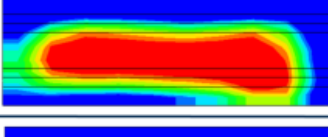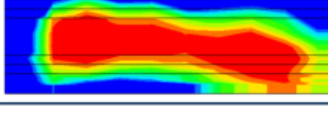
Figure 7-10: (a): 45° flow deflector installed at the static model inlet,
(b): Isometric view of the flow deflector showing the inner components

As illustrated in Fig. 7-10, the flow deflector was installed upstream of the inlet of the static model duct to create a flow incidence angle of about 45°. Furthermore, two different flow speeds were specified to determine the impact of the Reynolds number on the post-processed RTD temperature value. The results of this experiment using the 4th iteration thermal mass flow meter are shown in Table 7-2.

Table 7-2: Robustness of the 6-wire RTD technique

θ	Re	% Diff $_{\Delta Tb}$ -20-15-10 -5 0 5 10 15 20	$\dot{m}$ $[g/s]$	$\%Diff_{\dot{m}}$	ΔT_b	$\%Diff_{\Delta T}$	ΔT_{RTD}	$\%Er_{\Delta T}$
0°	4,857		2.74	—	17.07	—	17.17	1%
45°	4,960		2.68	2%	17.68	1%	17.67	1%
0°	10,749		5.91	120%	8.40	51%	8.50	1%
45°	10,604		5.82	115%	8.41	51%	8.43	1%

In this table, the first case represents the scenario of purely radial flow, and just below, is the flow deflected at 45°. Thus, by comparing the first two rows, one can observe that both cases have a similar mass flow rate (2% difference) and bulk temperature difference (1% difference), which implies that the deflected flow does not sufficiently distort the flow nor cause large errors in the bulk temperature difference reading (in both cases, the temperature difference obtained from the 6-wire RTD (ΔT_{RTD}) is within 1% of the bulk temperature difference (ΔT_b)). Thus, the proposed RTD technique appears to be independent of the incidence angle. To analyze the effect of flow velocity, the Reynolds number was also varied by a factor of two. As shown in Table 7-1, the mass flow rate also increased by a factor of two, while the bulk temperature decreased by the same factor. Once again, the temperature difference obtained from the 6-wire RTD (ΔT_{RTD}) was within 1% of the bulk temperature difference (ΔT_b). Thus, the method is also robust with respect to variations in flow velocity. To further demonstrate its robustness, one can consider the case of a deflected inlet flow at a higher Reynolds number. Again, this result shows a discrepancy between the bulk temperature difference and the RTD value within 1%. This behavior is partially due to the fact that the flow is almost symmetric about both axes.

7.2　Results of the 5th iteration design

The result from the 4th iteration design prompted the design and manufacturing of the 5th iteration prototype featuring the proposed 6-wire RTD technique. Thus, experiments were carried out to test the 5th design's performance, as well as, to compensate the measurements for the flow blockage it causes.

7.2.1　Performance of the 5th iteration design

The accuracy of the 5th iteration thermal mass flow meter was evaluated using the previously developed validation method. Shown in Fig. 7-11 is the new design of the anemometer installed in the static model shown, as well as, the velocity and temperature contours at the duct outlet.
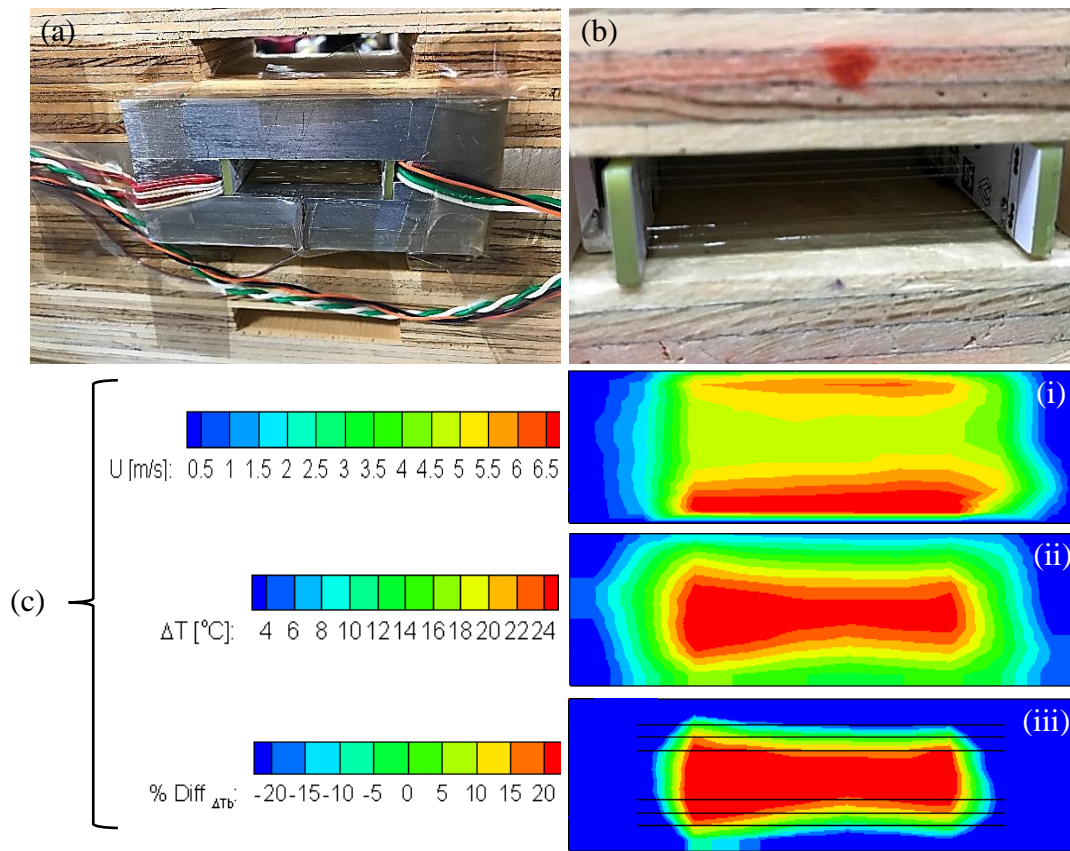
Figure 7-11: (a): 5th iteration thermal mass flow meter at the inlet of the static model,

(b): Static model outlet showing the RTD wires,

(c) Duct exit velocity (i), temperature (ii), and $\%Diff_{\Delta T_b}$ (iii) contours

Fig. 7-11a shows the inlet RTD wires, which are uniformly distributed as the temperature entering the duct is uniform. Also shown are the wires needed to power the anemometer, and to make the voltage measurement. In all, 12 wires are required for this sensor to heat the flow and to measure the inlet and outlet temperatures. Fig. 7-11b depicts the unique distribution of the RTD wires required to capture the bulk temperature difference. As shown by the contours in Fig. 7-11c, both the velocity and temperature contours at the duct outlet are narrower compared to the one of the previous design (Fig. 7-3), as the arms that hold the RTD wires extend up to the duct outlet, and thus, further restrict the flow. The contour of the percent difference in bulk temperature illustrates the location of the RTD wires. From this image, one can observe that the RTD wires are within the region where the temperature rise corresponds to the bulk temperature.

Using the data from the 5th iteration design, one can determine the following: i) if the designed RTDs correctly measure the temperature at their location, and ii) if the position of the wires is at the best location to capture the region where the temperature corresponds to the bulk value. The first point can be determined by comparing the post-processed temperature value to the measured one, whereas the second point can be determined by comparing the post-processed values of the RTD and the bulk temperature difference, as shown in Table 7-3.

Table 7-3: Performance of the designed RTDs

Wire placement	Symmetric 2-3-4 mm				Symmetric 2.3-3.3-4.3 mm	
Quantity	ΔT_{RTD}[°C]	$\%Diff_{\Delta T}$ [°C]	ΔT_b [°C]	$Er_{\Delta T}$ [%]	ΔT_{RTD}[°C]	$Er_{\Delta T}$ [%]
Post-processed value	18.94	-	18.16	4.1	18.24	1
Measured value	17.46	-7.8	-	-	-	-

By comparing the measured temperature using the RTD wires to that obtained by prost-processing, one observes that the measured value is approximately 8% lower and thus, the accuracy of the designed RTDs is lower than the theoretical value. This error is due to the following: i) in the experiment, the wire placement is not necessarily guaranteed and, ii) the temperature value obtained from the RTDs is not an arithmetic mean of the temperature

along the wire due to conduction effects. The effect the first point is illustrated in Table 7-3, where through post-processing the optimal 6-wires placement was found to be at 2.3-3.3-4.3 mm symmetrically about the centerline, thus a 0.3 mm deviation in the wire placement can impose a 3% error in value obtained for the bulk temperature.

From this data, one can also validate the overall performance of the designed thermal mass flow meters. For the 4th iteration design, the mass flow rate is calculated by obtaining the post-processed value of the bulk temperature difference from the thermocouple/hot-wire data, whereas for the 5th iteration design, the mass flow rate is obtained from the measured bulk temperature difference using the RTD wires. For comparison, the post-processed value of the bulk temperature difference was also computed for the 5th iteration design. By comparing the values obtained for the mass flow rate through post-processing and from the RTD measurements, to the ones obtained by hot-wire anemometry, one can determine the respective method's performance. The results of this comparison are presented in Table 7-3:

Table 7-4: Performance of the designed thermal mass flow meters

Method used to obtain ΔT_b	Design	$\dot{m}_{hot-wire}$ $[kg/s] \cdot 10^{-3}$	$\dot{m}_{sensor}$ $[kg/s] \cdot 10^{-3}$	$Error$ $[\%]$
Post-processing	4th Iteration	2.59	2.90	12.2
Post-processing	5th Iteration	2.57	2.76	7.2
Measurement	5th Iteration	2.57	2.87	11.5

By comparing the post-processed values of the 4th and 5th iteration design's, one observes that the latter outperformed the former, which is a result of key design changes. Moreover, the measured value obtained by the 5th iteration design was less accurate than the post-processed value, which is due to inaccuracies in the RTD technique. However, using the measured and post-processed values for bulk temperature difference in the calculation of the mass flow rate yielded similar results for 5th and 4th iteration designs. This demonstrates the ability of the 6-wire RTD to obtain the mass flow rate with acceptable accuracy. It is also important to note that the values obtained for the mass flow rate on the scale model duct need to be corrected since the presence of the anemometer causes a flow restriction. For this reason, a compensation curve is required to determine the sensor's blockage coefficient.

7.2.2 Anemometer blockage factor

An immersion-type thermal mass flow meter such as the one designed herein is an intrusive device that restricts the flow, and thus will lead to an under prediction of the mass flow rate in the duct. A coefficient that accounts for this effect is called the blockage factor, which is defined as the ratio between mass flow rate in an empty duct and the mass flow rate in the same duct equipped with the sensor. This coefficient was determined by obtaining the mass flow rate at three different speeds using hot-wire anemometry at the outlet of an empty duct and of a duct equipped with a sensor, as shown in Fig. 7-12.
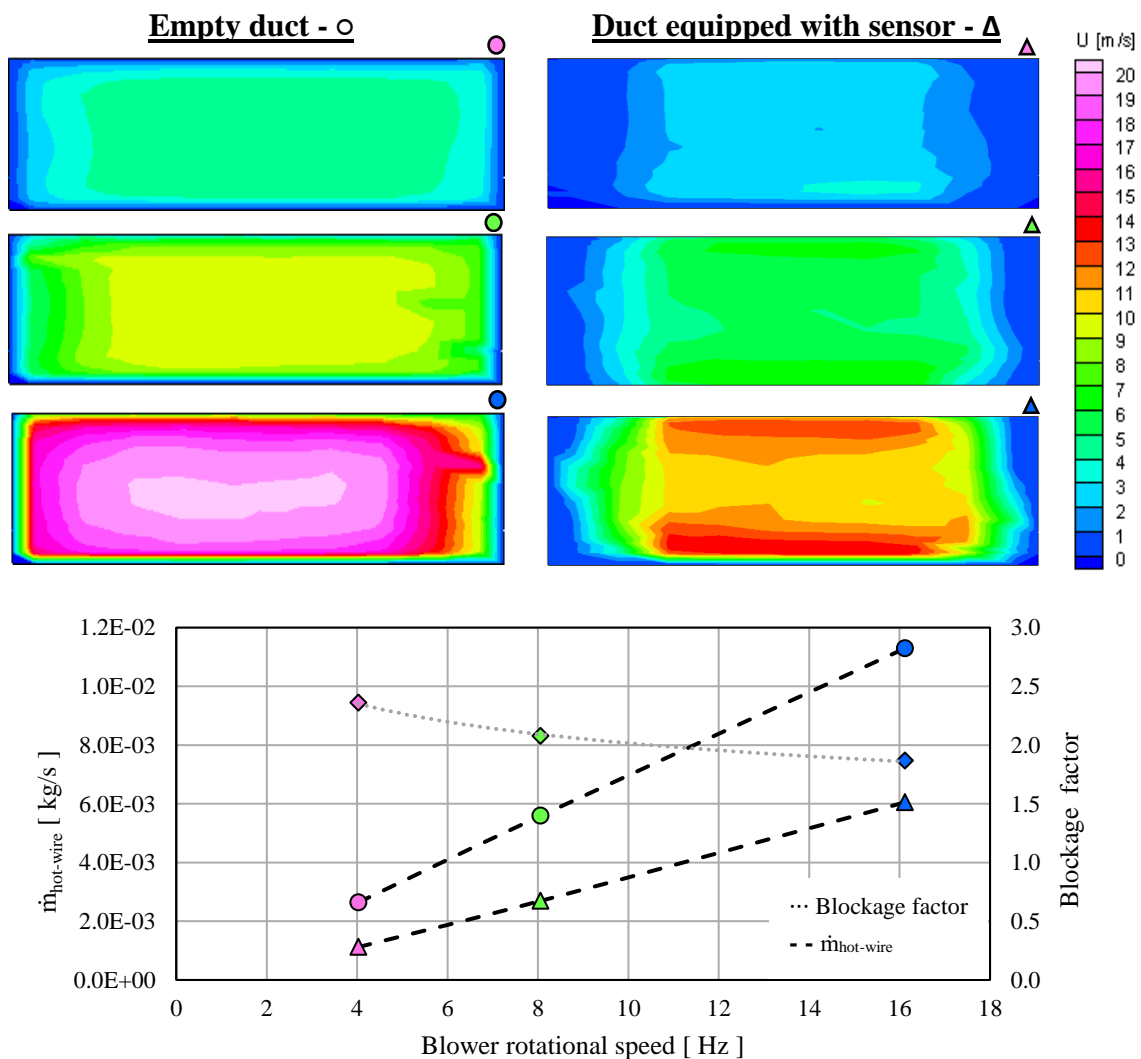
Figure 7-12: Evolution of the blockage factor as a function of flow velocity

In Fig. 7-12, circles represent data taken in an empty duct, triangles represent data taken with the anemometer placed within the duct, and diamonds represent the blockage factor. The colors correspond to three blower rotational speeds of 4.06 Hz (pink), 8.06 Hz (green), and 16.12 Hz (blue). The velocity contours show that, when the anemometer is present in the duct, a larger region of low-velocity is observed at both ends. This phenomenon is due to the anemometer's arms that hold it in place within the duct. The effect of the wires that comprise the heating element is also visible for the high flow case, where the array of wires blocks the flow in the middle of the duct. Considering the variation in blockage with the mass flow rate obtained with the duct equipped with the anemometer, one can obtain a correlation between the two, as shown in Fig 7-13.
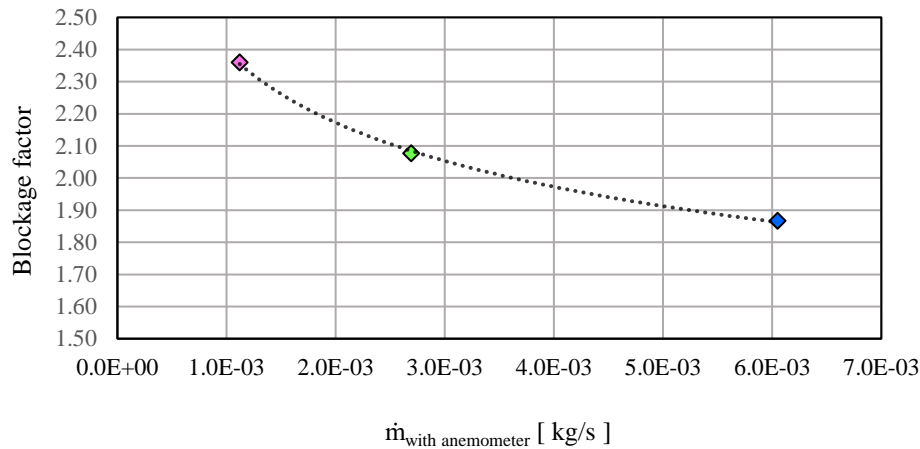
Figure 7-13: The variation of the flow blockage factor with mass flow rate

The blockage factor is nonlinear and follows a power law as:

$$C_{\dot{m}} = \frac{\dot{m}_{empty\ duct}}{\dot{m}_{with\ anemometer}} = a \cdot \dot{m}_{with\ anemometer}{}^{b},$$ (7.6)

where the coefficients of Eq. 7.6 are shown in Table 7-5.

Table 7-5: Blockage factor power law coefficients (from Fig. 7-13)

Coefficient	a	b
Value	0.915	-0.139

The experimental validation phase of the thermal mass flow meter led to a viable method to characterize the flow in the rotor rim ducts of a hydroelectric generator. The 4th iteration design showed that one cannot capture the bulk temperature at the duct outlet using a single-point temperature measurement. This led to the development of a 6-wire RTD technique, which has shown to be accurate and robust to varying flow conditions that may exist in hydroelectric generators. The RTD technique was then validated in the 5th iteration design and the measurements showed that although the RTD approach is not as accurate as estimated by post-processing, its performance is within the range of desired accuracy. These experiments also determined the compensation curve needed to account for the effect of flow blockage in a duct equipped with the sensor. Of the four-objective presented in Chapter 1, the experiments performed on the static model validated the anemometer's performance and its ability to fit inside a typical rotor rim duct, but it was not possible to validate the anemometer's capability of surviving the harsh environments found in a rotating machine (e.g. ~300 g, 45°C, and magnetic fluxes).

To verify the anemometer's capability to resist the level of g-forces found in hydroelectric generators, an FEA analysis was performed by a mechanical engineer at the IREQ, as per company policy. The results indicated that the anemometer would survive the large g-forces as it is made of lightweight materials and has no moving parts. The anemometer's capability of resisting the high temperatures and magnetic fluxes found in these machines was ensured by selecting materials that could withstand temperatures well above 45°C for all the anemometer's components. Finally, it was also verified that the magnetic fluxes would not effect the temperature measurements since RTD sensors are known to have a good immunity to electromagnetic fields. Thus, to this end, all objectives have been met either, by experimental measurements or numerical studies.

Chapter 8
Conclusions/Future Work

8.1   General summary and conclusions

The approached used in the development of the anemometer was divided into three phases: i) the preliminary phase, ii) the validation phase, and iii) the proof of concept. These three phases ultimately met the following four research objectives: i) provide an accurate measurement (~10%) of the flow in the rotor rim ducts, ii) design an anemometer small enough to fit in the rotor rim ducts, iii) design and anemometer capable of operating in a harsh environment, and iv) the accuracy of the measurements made by the anemometer must be independent of magnetic fluxes.

The preliminary phase showed the following: i) no measurements have ever been made in the rotor rim ducts of a hydroelectric generator, ii) the IREQ's scale model will facilitate the transfer of developed sensors to real hydroelectric generators, and iii) among the reviewed flow measuring techniques only thermal mass flow meters or hot-wire anemometers have the potential of meeting the research objectives.

The validation phase demonstrated the following: i) when comparing a thermal mass flow meter to a hot-wire anemometer, the former is better suited to meet the research objectives, as the accuracy in the measurements performed by the latter are dependent upon the flow variations seen in hydroelectric generators, ii) the performance of a thermal mass flow meter can be validated by using a static model and a thermocouple/hot-wire approach, and iii) the prototype design phase showed that the 4th and 5th iteration design of a thermal mass flow meter are capable of fitting inside the rotor rim ducts and heating the flow therein.

The proof of concept phase showed that: i) the anemometer can meet the research objectives, and ii) the measurements made by the RTD technique were independent of flow variations that occur in hydroelectric generators. The following two research objectives were met in the proof of concept phase: i) the 5th iteration design can measure the mass flow rate in the ducts of the static model with accuracies of approximately 10%, and ii) the prototypes are indeed small enough to fit inside the rotor rim ducts. The remaining two objectives were met by i) FEA simulations performed at the IREQ by mechanical engineers, which demonstrated the anemometer ability to survive the large g-forces, and ii) the design of the temperature sensors, which have a good immunity to magnetic fluxes.

8.2 Future Work

Although the developed sensor showed satisfactory performance in the static model, some improvements are required to have a device that can be installed in an operating hydroelectric generator. Shown below are some examples:

    i.   its manufacturability on a larger scale,

    ii.   its ease of installation and operation in an actual machine

    iii.   its durability in harsh environments

To achieve these future objectives, the following steps are required:

    i.   test the sensor's performance in the rotating scale model,

    ii.   implement design improvements,

    iii.   perform tests on a real hydroelectric generator.

As previously mentioned, the tests on the scale model will require a system capable of collecting data on rotating machinery. Much work has been done towards this end by Kirouac, during his internship at the IREQ [35]. More specifically, Kirouac developed a DAQ system capable of powering the thermal mass flow meter and acquiring the data from this sensor. Although this system was designed for the scale model, only minor modifications are required to enable its use on a real hydroelectric generator. Once all the tasks mentioned are accomplished, it will be possible to install several of these sensors in an actual hydroelectric generator to characterize the flow in the rotor rim ducts, so that one may detect any possible anomalies.

Appendix A
Uncertainty Analysis

A.1   First-order uncertainty propagation analysis

A measured value x can be separated into its average component $(\bar{x})$ and its deviation $(\mathcal{U}_x)$ as:

$$x = \bar{x} + \mathcal{U}_x. \qquad (A.1)$$

The deviation is often referred to as the measurement uncertainty or error. There are two main types of error: bias error and precision error. Bias errors remain constant during a given series of measurements and can be estimated by comparisons, or quantified by calibration and experience. Precision errors are the scatter in the measured data and are affected by: i) the measurement system (i.e., repeatability and resolution), ii) the measurand, (i.e., temporal and spatial variations (e.g. turbulence)), iii) the process (i.e., variations in operating and environmental conditions) and iv) the measurement procedure/technique (i.e., repeatability). As a rule of thumb, an error is a precision error if it can be statistically estimated otherwise it is a bias error. It is common that an error is a precision error, but statistical data is unavailable. Thus, one can perform an error propagation analysis to quantify the error. Usually performing a measurement requires several operations and each operation introduces a source of error. Consequently, a measured value x, that has N sources of error e_i, where $i = 1, 2, ..., N$, one can apply the Root-Sum-Squares (RSS) method to obtain the uncertainty in x as shown [36]:

$$\mathcal{U}_x = \pm\sqrt{e_1^2 + e_2^2 + \cdots + e_N^2} = \pm\sqrt{\sum_{i=1}^{N} e_i^2}. \qquad (A.2)$$

This is a very conservative estimate which assumes: i) the quantity behaves in a Gaussian manner and ii) the error will occur on a worst-case basis. The error of interest is often based on a functional relationship in conjunction with the measured value as shown:

$$y = \bar{y} + \Delta y = f(\bar{x} + \Delta x). \qquad (A.3)$$

Therefore, to quantify the error one must perform a Taylor series expansion:

$$\bar{y} + \Delta y = f(\bar{x}) \pm \left\{ \left(\frac{dy}{dx}\right)_{x=\bar{x}} \Delta x + \frac{1}{2}\left(\frac{d^2y}{dx^2}\right)_{x=\bar{x}} (\Delta x)^2 + \cdots \right\}. \qquad (A.4)$$

From Eq. A.4, one can determine that the mean value for y must be $f(\bar{x})$ and the uncertainty must be the value within the brackets. Assuming a linear approximation of Δy, which is valid if Δx is small, one may neglect the higher order terms and obtain a first-order approximation as:

$$\Delta y \approx \left(\frac{dy}{dx}\right)_{x=\bar{x}} \Delta x, \qquad (A.5)$$

where the derivative defines the slope of the line passing through the mean value. Therefore, one may assume that for small deviations from the mean, the slope predicts the approximate relationship between Δx and Δy. Consequently, the uncertainty in x ($\mathcal{U}_x$) is related to the uncertainty in y ($\mathcal{U}_y$) by [36]:

$$\mathcal{U}_y = \left(\frac{dy}{dx}\right)_{x=\bar{x}} \mathcal{U}_x. \qquad (A.5)$$

It is often necessary to extend this to multivariable relationships. Thus, a result $\mathcal{R}$, which is determined through some functional relationship between independent variables $x_1, x_2, \ldots, x_L$ defined as:

$$\mathcal{R} = f_1\{x_1, x_2, \ldots, x_N\}, \qquad (A.6)$$

where N the number of independent variables, and each variable x holds some measurable uncertainty that could affect $\mathcal{R}$. As in Eq. A.1, one could estimate this as:

$$\mathcal{R} = \bar{\mathcal{R}} + \mathcal{U}_{R,} \qquad (A.7)$$

where the sample mean of $\mathcal{R}$ is expressed as:

$$\bar{\mathcal{R}} = f_1\{\bar{x}_1, \bar{x}_2, \ldots, \bar{x}_L\}, \qquad (A.8)$$

and its uncertainty may be expressed by the following relationship:

$$\mathcal{U}_R = f_1\{\mathcal{U}_{\bar{x}_1}, \mathcal{U}_{\bar{x}_1}, \ldots, \mathcal{U}_{\bar{x}_N}\}. \qquad (A.9)$$

In Eq. A.9, each $\mathcal{U}_{\bar{x}_i}$ from $i = 1, 2, \ldots, N$ is the best estimate for the uncertainty of each independent variable of the result, which in turn reflects the propagation of uncertainty

through the result. From a Taylor series expansion of A.5 and with the substitution of Eq. A.6, one obtains the general sensitivity index Q_i [36]:

$$Q_i = \frac{\partial \mathcal{R}}{\partial x_{x=\bar{x}}}, i = 1,2, \dots, N,$$

(A.10)

which relates how changes in each x affect $\mathcal{R}$. The contribution of the uncertainty in the independent variable and the result is estimated by the term $Q_i \mathcal{U}_{\bar{x}_i}$, and the most probable estimate of $\mathcal{U}_{\mathcal{R}}$ is generally accepted as the square root of the sum of the squares of $Q_i \mathcal{U}_{\bar{x}_i}$ as [36]:

$$\mathcal{U}_{\mathcal{R}} = \pm \sqrt{\sum_{i=1}^{N} \left(Q_i \mathcal{U}_{\bar{x}_i} \right)^2}$$

(A.11)

In a more practical sense the value of the variable to be measured is generally affected by the instrument resolution. Therefore, as a rule of thumb, one assigns a numerical value $\mathcal{U}_0$, called the zeroth-order uncertainty, of one half the instrument resolution at a probability of 95%:

$$\mathcal{U}_0 = \pm \left(\frac{1}{2} \right) Smallest\ Incremental\ measurement$$

(A.12)

In most cases, this type of error is provided by the manufacturer.

A.2 Uncertainty in reference measurement

The reference measurement used to validate the thermal mass flow meter was obtained by collecting several points using a hot-wire/thermocouple combination and then by integrating to obtain the mass flow rate, as shown:

$$\dot{m}_{hot-wire} = \iint \rho(T(x,y))U(x,y)dxdy.$$

(A.13)

to quantify the error on the reference one must quantify the error on its independent variables. In Eq. A.13, the density was calculated using a second-order polynomial curve-fit as:

$$\rho(T) = aT^2 + bT + c.$$

(A.14)

The uncertainty for the density $(\mathcal{U}_\rho)$ can be found by applying Eq. A.11 as follows:

$$\mathcal{U}_\rho = \pm \sqrt{\left(\left(\frac{d\rho}{dT}\right) \cdot \mathcal{U}_T\right)^2} = \pm (2aT + b) \cdot \mathcal{U}_T, \qquad (A.15)$$

Where the uncertainty in temperature $(\mathcal{U}_T)$ is a zeroth-order uncertainty specified by the manufacturer of the thermocouple.

The heated flow velocity at the duct outlet of the static model was determined using the modified form of King's law and a least-squares fit to the E^2 vs. U calibration data at different flow temperatures and then by correcting the constants for non-isothermal flows using Lienhard's method:

$$U(E) = \left(\frac{E^2 - \mathcal{A}_L}{\mathcal{B}_L}\right)^{1/\bar{n}}, \qquad (A.16)$$

where

$$\mathcal{A}_L = \bar{\mathcal{A}}\left(\frac{T + T_w}{2}\right)^{0.84} (T_w - T), \qquad (A.17)$$

and

$$\mathcal{B}_L = \bar{\mathcal{B}}(T_w - T). \qquad (A.18)$$

The calibration equipment used to relate the reference flow velocity (U) to the anemometer's output voltage (E) has a relative uncertainty of 1%, which is common for commercial calibrators. Thus, the error due to the anemometer voltage will be neglected. The curve-fit using Lienhard's method was obtained using a least-squares fit with three degrees of freedom. This error is found by subtracting the reference velocities (U_R) from the velocities obtained by the curve-fit $(U(E_i))$ and squaring the sum of this value over the number of data point taken (N). The sum was then divided by $N - 3$, to account for the three degrees of freedom $(\mathcal{A}_L, \mathcal{B}_L, n)$. One must then add the uncertainties of the coefficients $(\mathcal{A}_L, \mathcal{B}_L)$ as:

$$\mathcal{U}_U = \pm \sqrt{\frac{1}{N-3}\sum_{i=1}^{N}(U(E_i) - U_R)^2 + \left(\left(\frac{dU}{d\mathcal{A}_L}\right)\cdot(\mathcal{U}_{\mathcal{A}_L})\right)^2 + \left(\left(\frac{dU}{d\mathcal{B}_L}\right)\cdot(\mathcal{U}_{\mathcal{B}_L})\right)^2}. \quad (A.19)$$

Both coefficients $(\mathcal{A}_L, \mathcal{B}_L)$ and T have uncertainties, that can be computed as follows:

$$\mathcal{U}_{\mathcal{A}_L} = \pm \sqrt{\frac{1}{N-2}\sum_{i=1}^{N}(\mathcal{A}(T_i) - \mathcal{A}_m)^2 + \left(\left(\frac{d\mathcal{A}_L}{dT}\right)\cdot\mathcal{U}_{\Delta T}\right)^2}, \quad (A.20)$$

and

$$\mathcal{U}_{\mathcal{B}_L} = \pm \sqrt{\frac{1}{N-2}\sum_{i=1}^{N}(\mathcal{B}(T_i) - \mathcal{B}_m)^2 + \left(\left(\frac{d\mathcal{B}_L}{dT}\right)\cdot\mathcal{U}_{\Delta T}\right)^2}. \quad (A.21)$$

In Eqs. A.20 and A.21, the first term is the uncertainty of the curve-fit and the second term represents the uncertainty due to the maximum variation in the calibration temperature, which was 1.2°C. Finally, in Eq. A.13 there is also an uncertainty in the area. This variable was obtained using a caliper to measure the width (x) and height (y) of the duct's exit. Knowing this information and applying Eq. A.11 to Eq. A.13 one obtains:

$$\mathcal{U}_{\dot{m}_{hot-wire}} = \pm \sqrt{\left(\left(\frac{d\dot{m}}{d\rho}\right)\cdot(\mathcal{U}_\rho)\right)^2 + \left(\left(\frac{d\dot{m}}{dU}\right)\cdot(\mathcal{U}_U)\right)^2 + \left(\left(\frac{d\dot{m}}{dx}\right)\cdot(\mathcal{U}_x)\right)^2 + \left(\left(\frac{d\dot{m}}{dx}\right)\cdot(\mathcal{U}_x)\right)^2}, \quad (A.22)$$

where the uncertainties for the density and velocity are given by Eqs. A.15 and A.19, and the uncertainties in the width and height are zeroth-order uncertainties specified by the caliper.

A.3 Uncertainty in the developed anemometer

The developed anemometer is governed by the following equation:

$$\mathcal{P}_{inj} = \dot{m}_{calc} cp \Delta T_b \qquad (A.23)$$

where the energy injected into the flow is controlled by a power supply:

$$\mathcal{P}_{inj} = E \cdot I. \qquad (A.24)$$

Therefore solving for the mass flow rate one obtains:

$$\dot{m}_{calc} = \frac{IE}{cp}\left(\frac{1}{\Delta T_b}\right), \qquad (A.25)$$

where the bulk temperature difference (ΔT_b) is obtained using the 6-wire RTD technique. Similar to Eq. A.14, the specific heat at constant pressure was calculated using a second-order polynomial curve-fit:

$$cp(T_{RTD}) = aT_{RTD}^2 + bT_{RTD} + c, \qquad (A.26)$$

which has an uncertainty of:

$$\mathcal{U}_{cp} = \pm \sqrt{\left(\left(\frac{dcp}{dT_{RTD}}\right)\cdot(\mathcal{U}_{T_{RTD}})\right)^2} = \pm(2aT_{RTD} + b)\cdot\mathcal{U}_{T_{RTD}}. \qquad (A.27)$$

The bulk temperature difference is calculated as:

$$\Delta T_b = T_b - T_i, \qquad (A.28)$$

where both temperatures are obtained by the custom RTDs from the following curve-fit:

$$T_{RTD} = \frac{-b + \sqrt{b^2 - (4a \cdot (c - R_{RTD}))}}{2a}. \qquad (A.29)$$

The uncertainty in the curve-fit is due to the uncertainty in the resistance measurement:

$$U_{T_{RTD}} = \pm \sqrt{\left(\left(\frac{dT_{RTD}}{dR_{RTD}}\right) \cdot \left(U_{R_{RTD}}\right)\right)^2} = \frac{\pm U_{R_{RTD}}}{\sqrt{b^2 - 4a(c - R_{RTD})}}, \qquad (A.30)$$

and thus, the uncertainty in the bulk temperature difference is:

$$U_{\Delta T_b} = \pm \sqrt{\left(\left(\frac{d\Delta T_b}{dT_b}\right) \cdot U_{T_{RTD}}\right)^2 + \left(\left(\frac{d\Delta T_b}{dT_i}\right) \cdot U_{T_{RTD}}\right)^2}. \qquad (A.31)$$

Therefore, one can determine the uncertainty in Eq. A.23 as:

$$U_{\dot{m}_{calc}} = \pm \sqrt{\left(\left(\frac{d\dot{m}}{dI}\right) \cdot U_I\right)^2 + \left(\left(\frac{d\dot{m}}{dE}\right) \cdot U_E\right)^2 + \left(\left(\frac{d\dot{m}}{dcp}\right) \cdot U_{cp}\right)^2 + \left(\left(\frac{d\dot{m}}{d\Delta T_b}\right) \cdot U_{\Delta T_b}\right)^2}. \qquad (A.32)$$

Where the uncertainties in current and voltage are zeroth-order uncertainties specified by the variable voltage source, the uncertainty in the specific heat at constant pressure is specified by Eq. A.27 and the uncertainty in bulk mean temperature difference is given by Eq. A.31.

A.4 Zeroth-order uncertainties

The zeroth-order uncertainties were calculated using Eq. A.12 and the measurement precision of the given apparatus. All zeroth-order uncertainties are listed in Table A-1:

Table A-1: Zeroth-order uncertainties

Uncertainty	Specified Value
U_T	$\pm 1.0°C$
$U_{\Delta T}$	$\pm 1.2°C$
U_x	$\pm 0.05\ mm$
U_y	$\pm 0.05\ mm$
$U_{R_{RTD}}$	$\pm 0.0005\ \Omega$
U_I	$\pm 0.0005\ A$
U_E	$\pm 0.0005\ V$

A.5   First-order uncertainties

The first-order uncertainties were calculated using Eq. A.11 and are dependent upon the zeroth-order uncertainties list in table A-1. All calculated fist-order uncertainties are listed in Table A-2:

Table A-2: Calculated first-order uncertainties

Relative Uncertainty	Calculated Value [%]
$\mathcal{U}_\rho / \rho$	$\pm\, 0.32$
$\mathcal{U}_U / U$	$\pm\, 8.84$
$\mathcal{U}_{\mathcal{A}_L} / \mathcal{A}_L$	± 1.50
$\mathcal{U}_{\mathcal{B}_L} / \mathcal{B}_L$	$\pm\, 4.61$
$\mathcal{U}_{cp} / cp$	$\pm\, 0.00$
$\mathcal{U}_{T_{RTD}} / T_{RTD}$	$\pm\, 0.12$
$\mathcal{U}_{\Delta T_b} / \Delta T_b$	$\pm\, 0.33$

A.6   Results of the uncertainty analysis

Using the presented propagation of uncertainty analysis, the uncertainties in both the reference hot-wire and the thermal mass flow meter are listed in Table A-3.

Table A-3: Uncertainty values for the reference hot-wire and developed sensor

Relative Uncertainty	Calculated value [%]
$\mathcal{U}_{\dot{m}_{hot-wire}} / \dot{m}_{hot-wire}$	± 4.26
$\mathcal{U}_{\dot{m}_{sensor}} / \dot{m}_{sensor}$	± 0.30

REFERENCES

[1]   "Cross-section view of a generating unit," in *Turbine-Generator Units*, ed: Hydro-Québec.

[2]   E. Bach, "Characterization of the air flow in a scale model pf a hydrogenerator by means of particle image velocimetry," Master's thesis, McGill University, 2015.

[3]   K. Toussaint, "Caractérisation de l'écoulement d'air dans une maquette d'alternateur hydroélectrique par méthodes numérique et expérimentale," Master's thesis, École Polytechnique de Montréal, 2011.

[4]   C. Hudon, A. Merkhouf, M. Chaaban, S. Belanger, F. Torriano, J. Leduc*, et al.*, "Hydro-generator multi-physic modeling," *European Journal of Electrical Engineering,* vol. 13, pp. 563-589, 2010.

[5]   N. Saleban, P. Germano, C. Hudon, and Y. Perriard, "Développement de capteurs de mesures de la vitesse de l'air dans le rotor des alternateurs," Master's thesis, EPFL, 2013.

[6]   A. Boglietti, A. Cavagnino, D. Staton, M. Shanel, M. Mueller, and C. Mejuto, "Evolution and Modern Approaches for Thermal Analysis of Electrical Machines," *IEEE Transactions on Industrial Electronics,* vol. 56, pp. 871-882, Mar 2009.

[7]   M. Chaaban, J. Leduc, C. Hudon, and D. Nguyen, "Thermal Behaviour of Large Hydro-Generator," in *International symposium on transport phenomena and dynamics of rotating machinery,* Honolulu, Hawaii, United States, 2008.

[8]   G. Dajaku and D. Gerling, "An improved lumped parameter thermal model for electrical machines," in *Proceedings of the 17th International Conference on Electrical Machines,* Chania, Crete Island, Greece 2006.

[9]   G. Traxler-Samek, R. Zickermann, and A. Schwery, "Cooling airflow, losses, and temperatures in large air-cooled synchronous machines," *IEEE transactions on industrial electronics,* vol. 57, pp. 172-180, 2010.

[10]   A. Fasquelle, J. Le Besnerais, S. Harmand, M. Hecquet, S. Brisset, P. Brochet*, et al.*, "Coupled electromagnetic acoustic and thermal-flow modeling of an induction motor of railway traction," *Applied Thermal Engineering,* vol. 30, pp. 2788-2795, 2010.

[11]   S. Pickering, D. Lampard, and M. Shanel, "Modelling ventilation and cooling of the rotors of salient pole machines," in *Electric Machines and Drives Conference, Cambridge, Massachusetts, USA, 2001. IEEE International*, 2001, pp. 806-808.

[12]   M. Shanel, S. J. Pickering, D. Lampard, "Conjugate heat transfer analysis of a salient pole rotor in an air cooled synchronous generator," in *Electrical Machines and Drives Conference,* Madison, Wisconson, USA, 2003.

[13]   N. Gunabushanam and J. Suresh, "Experimental and CFD analysis of hydrogenerator ventilation components," in *CIGRE, International Council of Large Electric Systems,* 2006.

[14]   H. Lang, C. Kral, A. Haumer, M. Haigis, and R. Schulz, "Investigation of the thermal behavior of a salient pole synchronous machine,"in *Proceedings of the 17th International Conference on Electrical Machines,* Chania, Crete Island, Greece, 2006.

[15]   A. A. Pasha, M. Hussain, and N. Gunubushanam, "Experimental and CFD analysis of hydrogenerator stator," in *Proceedings of the 37th National & 4th International Conference on Fluid Mechanics and Fluid Power,* Madras, Chennai, India, 2010.

[16]   G. Kastner, E. Fernleitner, and M. Brunner, "Usage of computational fluid dynamics in the design process for prototype hydro-generators," in *Proceedings of the 16th International Seminar on Hydropower Plants*, Vienna, Austria, 2010.

[17]   K. Toussaint, F. Torriano, J.-F. Morissette, C. Hudon, and M. Reggio, "CFD analysis of ventilation flow for a scale model hydro-generator," in *ASME 2011 Power Conference,* Denver, Colorodo, USA, 2011. pp. 627-637.

[18]   E. Hartono, "Experimental study of air flow in a hydro power generator model," Master's thesis, Chalmers University of Technology, 2011.

[19]   E. Hartono, M. Golubev, P. Moradnia, V. Chernoray, and H. Nilsson, "A PIV Study of The Cooling Air Flow in An Electric Generator Model," Technical report, Department of Applied Mechanics, Chalmers University of Technology, 2012.

[20]   F. Torriano, N. Lancial, M. Lévesque, G. Rolland, C. Hudon, F. Beaubert, *et al.*, "Heat transfer coefficient distribution on the pole face of a hydrogenerator scale model," *Applied Thermal Engineering,* vol. 70, pp. 153-162, 2014.

[21] H. Jamshidi, H. Nilsson, and V. Chernoray, "Experimental and numerical investigation of hydro power generator ventilation," in *27th IAHR Symposium on Hydraulic Machinery and Systems*, Montreal, Quebec, Canada, 2014.

[22] P. Moradnia, V. Chernoray, and H. Nilsson, "Experimental assessment of a fully predictive CFD approach, for flow of cooling air in an electric generator," *Applied Energy,* vol. 124, pp. 223-230, 2014.

[23] P. Moradnia, M. Golubev, V. Chernoray, and H. Nilsson, "Flow of cooling air in an electric generator model–An experimental and numerical study," *Applied Energy,* vol. 114, pp. 644-653, 2014.

[24] E. Bach, L. Mydlarski, F. Torriano, J.-P. Charest-Fournier, H. Sirois, J.-F. Morissette*, et al.*, "PIV Characterization of the Air Flow in a Scale Model of a Hydrogenerator," in *ASME 2015 Power Conference*, San Diego, California, USA, 2015.

[25] V. Filipan, R. Budin, and A. Mihelić-Bogdanić, "Air flow measurement on hydro generators," in *International water power and dam construction,* vol. 45, pp. 44-46, 1993.

[26] E. Bourdreault, E. Lavoie, E. Lavalée, and S. Lavoie, "Maquette tournante alternateur: rapport de conception mécanique." Rapport technique IREQ-2011-0069, Institut de recherche d'Hydro-Québec (IREQ), Varennes, Canada,2011.

[27] C. Tropea, A. L. Yarin, and J. F. Foss, *Handbook of experimental fluid mechanics*, Springer, 2007.

[28] B. R. Munson, T. H. Okiishi, and W. W. Huebsch, *Fundamentals of fluid mechanics*, 6 ed. Hoboken, New Jersey, USA, J. Wiley & Sons, 2009.

[29] H. H. Bruun, *Hot wire anemometry : principles and signal analysis*. Oxford; New York, Oxford University Press, 1995.

[30] S. Tavoularis, *Measurement in fluid mechanics*. Cambridge; New York, Cambridge University Press, 2005.

[31] T. L. Bergman A. S. Lavine, F. P. Incropera, and D. P. Dewitt , *Fundamentals of heat and mass transfer*, 7 ed. Hoboken, New Jersey, USA, J. Wiley & Sons, 2011.

[32] "Probes for Hot-wire Anemometry," Dantec Dynamics, in *Brochure*, pp. 17, 2000.

[33]   J. Lienhard V and K. Helland, "An experimental analysis of fluctuating temperature measurements using hot-wires at different overheats," in *Experiments in fluids,* vol. 7, pp. 265-270, 1989.

[34]   S. P. Venkateshan, *Mechanical measurements*, 2 ed. Chichester, West Sussex, United Kingdom, Wiley, 2015.

[35]   Kirouac, Mathieu, "Système embarqué pour la mesure de débit massique dans les jantes d'un rotor d'alternateur de réseau," Rapport technique, Université de Sherbrooke, Québec, Canada, 2017.

[36]   R. S. Figliola and D. E. Beasley, *Theory and design for mechanical measurements*, 5 ed. Hoboken, New Jersery, USA, J. Wiley & Sons, 2011.